THE PENNSYLVANIA STATE UNIVERSITY
SCHREYER HONORS COLLEGE

DEPARTMENT OF MATERIALS SCIENCE AND ENGINEERING

Quantifying Surface Morphology of Additively Manufactured Plastics

BEVAN HARBINSON
SPRING 2023

A thesis
submitted in partial fulfillment
of the requirements
for a baccalaureate degree
in Materials Science and Engineering
with honors in Materials Science and Engineering

Reviewed and approved* by the following:

Bryan D. Vogt
Professor of Chemical Engineering
Thesis Supervisor

Amy Carol Robinson
Associate Teaching Professor of Materials Science and Engineering
Honors Adviser

* Electronic approvals are on file.

ABSTRACT

The applications for the additive manufacturing of plastics are currently limited by the inferior and anisotropic mechanical properties additively manufactured materials possess compared to materials manufactured by traditional subtractive or formative methods. Improved quality assurance and testing standards are necessary to minimize the impacts of poor material properties. Optical profilometry is a promising nondestructive method to measure the surface morphology and inter- and intra-layer contact of plastics additively manufactured by material extrusion. Acrylonitrile butadiene styrene tensile specimens were printed with 0° and 90° raster angles and 0.2 mm, 0.25 mm, and 0.3 mm layer heights. Surface morphology measurements were made with focus variation microscopy and converted into amplitude spectra using fast Fourier transforms. These spectra were analyzed to identify the wavelengths present in the surface morphology. Parameters describing the height variation, noisiness, and sinusoidal nature of the surface were calculated from the spectra and correlated with tensile testing results, providing the elastic modulus, ultimate tensile strength, and elongation at break of each specimen. The ultimate tensile strength of the specimens printed with a 90° raster angle was found to correlate positively with the amplitude of the two fundamental waves ($R^2 = 0.929$), positively with the mean absolute deviation of one of the fundamental waves across the width of the specimen ($R^2 = 0.785$), and negatively with the total harmonic distortion away from a sinusoidal morphology ($R^2 = 0.604$). No statistically significant correlations were found for the elastic modulus or elongation at break.

TABLE OF CONTENTS

LIST OF FIGURES

LIST OF TABLES

ACKNOWLEDGEMENTS

I would first like to thank Dr. Bryan Vogt for rekindling my interest in additive manufacturing through his class last year “CHE 497: 3D printing of plastics.” Since then, you have served as a great thesis supervisor by always suggesting new ideas and paths forward whenever I felt the least bit lost in my research.

Thank you, Sierra Yost, for training me on the 3D printer and other equipment when I was new to the lab and for all your day-to-day support in and out of the lab. I also want to thank both of my wonderful advisors Meg Abplanalp and Amy Robinson for always thinking of me.

Lastly, thank you to all my friends and family who were there for both the great times and difficult times this year.

Chapter 1

Introduction

1.1 Motivation

Additive manufacturing (AM), also referred to as three-dimensional (3D) printing, is a rapidly developing technology which operates by forming material into a free-form part layer by layer. AM has been increasingly replacing conventional manufacturing methods that rely on the removal of excess material as occurs in machining or the development of a mold to impart a predefined shape as occurs in molding [1]. The growth of AM technologies over the last 50 years has been attributed to the method's benefits over traditional manufacturing including, but not limited to: greater customizability of parts, complex part geometries not possible via machining or molding, lightweight designs utilizing lattice structures, and rapid prototyping [1][2].

Despite these advantages, AM has a few drawbacks including limitations of applicable materials, high relative costs for large scale production, and a lack of engineering design and testing standards [3][4]. AM also tends to produce diminished and anisotropic mechanical properties compared to the bulk material and lacks reliable quality assurance methods, such as monitoring of the process *in situ* and the resulting part [3][4][5]. Improved quality of AM is achievable with close monitoring and control of the printing feedstock, process parameters, and resulting part qualities [4]. The part qualities most relevant to the manufacturing of thermoplastic materials via a common AM technology called material extrusion (MatEx), also known as fused filament fabrication (FFF) or fused deposition modeling (FDM), are the porosity and the inter- and intra-layer bond strength of the resulting part [4][6].

Two of the most promising characterization techniques for the nondestructive measurement of the resulting part's amount of porosity and inter- and intra-layer contact are tomography and profilometry [5]. Tomography, typically X-ray computed tomography (CT), provides information on the internal morphology of the part after printing while profilometry, typically optical profilometry operating with laser scattering, focus variation microscopy (FVM), or structured light imaging (SLI), provides information on the 3D surface morphology during or after the print [2][5].

1.2 Objective

The present study seeks to apply a fast Fourier transform (FFT) based analysis to post-print measurements of the surface morphology of additively manufactured plastic parts to quantify differences in the regularity and uniformity of the surface not easily observable by eye. Acrylonitrile butadiene styrene (ABS) tensile specimens additively manufactured via MatEx will be imaged via FVM optical profilometry. ABS was selected due to its widespread use in MatEx printing which has been owed to its toughness, processability, and low cost [3][7]. This FFT analysis will be applied to specimens printed with varied process parameters including layer height and raster angle, as these are considered two of the most impactful process parameters on mechanical properties [8][9]. This process is expected to result in discernable differences in the relative amplitude and distribution of different spatial frequencies across print conditions, and to a lesser extent, within a given print condition. These spatial frequency differences will be correlated with the mechanical properties, including elastic modulus, ultimate tensile strength, and elongation at break. If successful, this correlation will allow for the future prediction of the

mechanical properties of an individual additively manufactured part based on the distribution of spatial frequencies acquired from surface morphology measurements rather than through destructive mechanical testing.

Chapter 2

Literature Review

2.1 Additive Manufacturing of Polymers

AM of any material typically follows the same general layer-wise process, although some researchers including Dolinski et al. have presented nonlayered AM methods [10]. First, an object is converted to a 3D model with the assistance of computer automated design (CAD) software. This model is then given to a slicer software which prepares the model for printing by slicing the design into many layers and converting it into a set of instructions for the 3D printer to follow [11]. It is at this step that one can make selections including layer height, print path, and build orientation. Finally, the printer forms each layer of the object by selectively depositing or fusing raw material along the programmed path [11]. AM technologies have been classified into seven categories according to ISO/ASTM 52900:2021: binder jetting (BJT), directed energy deposition (DED), material jetting (MJT), sheet lamination (SHL), powder bed fusion (PBF), vat photopolymerization (VPP), and MatEx [2][12]. These last three categories are the most relevant to the AM of polymer materials and will be discussed further.

All PBF technologies operate on the same principle where a thin layer of powder is spread on a platform to form a bed of powder. The powder is then fused into a layer of the desired shape using a laser. This process is then repeated by spreading a new layer of powder on top of the fused layer [3]. Thermoplastic materials can be printed with this technology through selective laser sintering (SLS). With this method, the laser does not fully melt the powder, only the surface of the powder particles, causing them to fuse together without inducing flow [3]. SLS can produce parts with fine details when using powders with small particle sizes and the powder

bed supports the printed structure without the need to design a separate support structure. However, SLS often produces parts with decreased structural integrity due to porosity caused by inefficient packing of powder particles.

VPP technologies typically employ stereolithography (SLA), where ultraviolet (UV) light is scanned across a layer to activate initiator molecules within a polymer resin and begin polymerization of the liquid resin into a solid layer which is then moved, and the process repeated [3]. While SLA can print parts with fine details and low porosity, it is limited to photopolymers and often requires postprocessing to fully cure parts for the necessary mechanical properties [2].

One of the most widespread technologies for the AM of polymer materials and the one relevant to the present study is MatEx [2]. This AM technology consists of a print bed upon which a motor-controlled extrusion nozzle heats a filament or pellets of thermoplastic material to a semi-molten state and deposits it along a programmed path to form a layer [7]. When the material exits the nozzle and meets the print bed of a previously deposited layer of material, it rapidly cools and solidifies, forming partially fused layers and roads, which are individual lines of material extruded on a given layer, often with voids between them [6]. A diagram of this process showing five layers, each five roads across, is given in Figure 2.1, where the extrusion width is the nominal width of a printed road, and the layer height is the amount the nozzle moves vertically between layers. MatEx is advantageous for its low cost and widespread use compared to other AM technologies, but it can only print details as fine as the layer height and extrusion width and produces anisotropic mechanical properties due to poor adhesion between roads and layers [2][6].

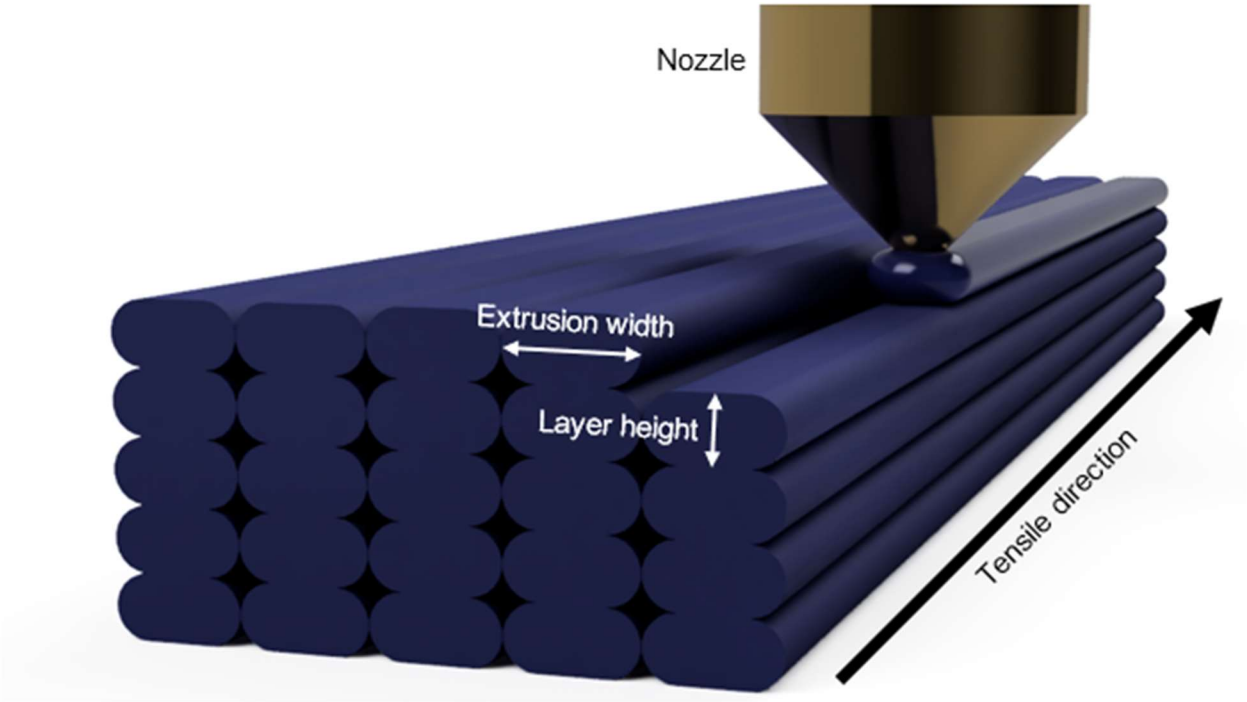

Figure 2.1: Diagram of the additive manufacturing process used in material extrusion. A filament of thermoplastic material (shown in blue) is fed through a heated nozzle (shown in brass) which extrudes the filament in a semi-molten state onto a print bed and successive layers as individual roads with a defined width, known as the extrusion width, and height, known as the layer height.

2.2 Material Extrusion Mechanical Properties

The weaker and more anisotropic mechanical properties of materials manufactured via MatEx compared to traditional methods like injection molding has been a longtime disadvantage of plastics additively manufactured by this method [8]. Ahn et al. measured the tensile strength of ABS specimens that were injection molded and that were printed via MatEx with various raster angles including 0° (roads running parallel to the tensile direction, as in Figure 2.1) and 90° (roads running perpendicular to the tensile direction). Injection molded ABS was found to have a tensile strength of 26 MPa while the 0° raster angle resulted in 73% tensile strength and the 90° raster angle resulted in 10% tensile strength [8]. Shubham et al. conducted a similar

study by varying the layer height from 0.075 mm to 0.5 mm. This study found a monotonic decrease in both tensile strength and elongation at break when increasing layer height with the 0.5 mm layer height resulting in 54% the strength and 66% of the elongation of the injection molded specimens which had a tensile strength of 36 MPa and an elongation at break of 5.8% [9]. This connection between increasing layer height and deteriorating mechanical properties can be explained by contact pressure. Coogan and Kazmer modeled inter-layer contact and contact pressure to find that small layer heights increased the pressure forcing roads into contact with existing material, improving inter-layer contact [6] Despite the inferior mechanical properties, it is often advantageous to use a larger layer height as this reduces the number of layers and manufacturing time [13]. Raster angle and layer height are two of the most influential factors on the mechanical properties of materials printed via MatEx, but other process parameters such as extrusion width, build orientation (flat on the bed vs standing upright), air gap or overlap between roads, and extruder and bed temperatures can all affect the mechanical properties as well [3][7][9].

The poor mechanical properties of parts printed via MatEx even after optimization of process parameters has been attributed to the rapid cooling of the extruded material upon contact with existing material preventing the polymer chains within the material from diffusing and entangling across the interface before cooling below the glass transition temperature (T_g) [14]. This results in weak inter- and intra-layer bond strength, compromising the mechanical properties of the material, especially perpendicular to the road direction [14][15][16]. This phenomenon makes the thermal history of a printed part a vital piece of information when determining its expected mechanical properties since the longer a road remains above its T_g, the more time polymer chains have to diffuse and entangle across interfaces [17]. This dependence

on thermal history makes parameters including printing speed, inter-layer cooling time, part size, and print path highly impactful on the ultimate properties of the resulting part [17][18][19]. Faes et al. found that ultimate tensile strength and elongation a break decreased for ABS tensile specimens printed upright as the inter-layer cooling time was increased due to this effect. A statistical difference was not observed for specimens printed flat presumably because the layer size was large enough that the previous layer had already mostly cooled even with the minimum inter-layer cooling time [18]. Ai and Vogt identified the same relationships between inter-layer cooling time and mechanical properties for polycarbonate (PC) specimens. The size of tensile specimen, which determines intra-layer cooling time, was found to influence the failure mechanism with smaller specimens (lower intra-layer cooling time) resulting in more ductile-like failure [19].

More recent research has focused on material design as opposed to process parameter optimization as a more promising method to improve the mechanical properties of parts produced via MatEx [15]. Levenhagen and Dadmun showed that the addition of low-molecular-weight surface-segregating additives (LMW-SuSAs), which were smaller than the polylactic acid (PLA) polymer chains in the neat material, improved inter-layer adhesion and isotropy due to increased chain diffusion across interfaces. Additionally, modification of the LMW-SuSAs with methacrylate end groups that would crosslink across the interfaces when exposed to UV radiation resulted in up to approximately 200% the transverse tensile strength of the unmodified material [15]. Examples of similar material design approaches included the introduction of hydrogen-bonding additives to polymethyl methacrylate (PMMA) filaments by Street et al. and the use of a core-shell filament structure with a quickly solidifying PC core to provide shape and an olefin ionomer shell to form crystalline domains and ionic bonds across the interfaces by Peng

et al. [16][20]. The implementation of these material design approaches may decrease the printability of the material since the melt flow behavior of the printed materials must be well understood and controlled for to additively manufacture parts successfully and consistently [21].

2.3 Quality Assurance via Optical Profilometry

3D tomography and profilometry methods including X-ray CT, laser scattering, FVM, and SLI have become more widespread in AM quality assessment compared to contact methods like stylus profilometry and atomic force microscopy (AFM) despite the superior spatial resolution of the latter, due to their potential for *in situ* nondestructive monitoring of the printing process [5][22]. Some optical profilometry techniques measure statistical parameters of the surface like roughness as is the case for laser scattering, where the distribution of scattered light around the specularly reflected beam can be compared to a standard to determine the roughness across the specimen surface [5][23].

Other techniques, like FVM and SLI, instead capture the actual surface morphology of the specimen [5]. SLI functions similarly to the stereo vision of humans except one camera/eye is replaced with a projector that illuminates the surface with a fringe pattern that appears as black and white lines on a flat surface but is distorted by the specimen's surface morphology when viewed by the camera at an angle. This distorted fringe can then be analyzed to form a 3D reconstruction of the surface [24].

FVM, the technique used in the present study, gradually adjusts the height of a lens, identifying at what height each pixel of the image has the highest contrast, indicating that it is in focus at that height. The focus depth of each pixel can then be plotted with its lateral position to

form a 3D heightmap of the surface [5][24]. The typical optics configuration for an FVM system includes a white light source shining onto the specimen surface and reflecting back into the objective lens and a camera sensor which measures the contrast of each pixel as a piezoelectric motor varies the working distance. These and other optical profilometry techniques can have a significant drawback for some surfaces due to systematic errors caused by the geometry of the optical system [25]. These instruments work well for flat and stepped structures, but steep slopes can result in errors and noisy data on the scale of surface features due to the specular reflection passing outside the aperture of the objective lens [25].

2.4 Surface Morphology Quantification

On a basic level, the 3D imaging techniques discussed above have been used to detect printing defects that result in incomplete objects by comparing the expected part geometry with that observed in situ to terminate the printing process prematurely if a failure is detected as demonstrated by Straub [26]. More complex analyses rely on similarity evaluation, where 3D surface morphology measurements (SMMs) are compared to determine if they are from the same surface or how similar two different surfaces are. This method can be applied to quality monitoring either *in situ* to measure the uniformity of the surface morphology within and across layers or *ex situ* to measure the uniformity of the similarity of the surface morphology across parts printed under identical or varied conditions [5]. *In situ* quality monitoring allows for the capture of 3D SMMs of the interior layers of a part before they are printed over but requires faster measurements than *ex situ* quality monitoring. Of the research into similarity evaluation in

manufacturing, some works rely on the spatial domain where the 3D SMMs are taken as-is, while others use the frequency domain, where SMMs are converted using Fourier transforms [5].

Works in the spatial domain often cut the 3D surface into line profiles where 1D roughness data can be easily extracted to compare different measurement techniques as in Poon and Bhushan [22]. Launhardt et al. and de Pastre et al. took similar approaches when comparing surface morphology measurement techniques but compared height differences in addition to roughness [27][28]. These feature-based methods can have higher error rates when evaluating the similarity of two surfaces because they do not account for larger scale geometries present in the SMMs [29]. Zheng et al. and Wang et al. each consider the entire surface in the special domain using either the Pearson correlation coefficient (PCC) or image distance, which is simply the height difference between the two 3D SMMs at each point [23][29].

Information in the frequency domain is typically accessed by cutting the 3D surface into line profiles and applying Fourier transforms to them for 1D frequency information [5]. An example of this comes from Thwaite, where a constructed apparatus was able to obtain the 1D Fourier transform of an image optically. The resulting power spectrum revealed the dominant wavenumbers (or wavelengths) present in the profile of the surface which were able to be superimposed to evaluate their similarity [30]. Jiang et al. instead applied 2D Fourier transforms to 3D SMMs to create a similarity evaluation framework using a similarity score derived from the PCC of the 2D Fourier transforms [5]. These similarity scores may be used with measurements at different locations on the same specimen to monitor the uniformity of an individual part or with measurements across specimens to monitor the repeatability of the manufacturing process between prints. Uniformity and repeatability are both essential to produce quality additively manufactured parts [29].

Chapter 3

Methodology

3.1 3D Printing Specimens

Hatchbox 1.75mm True Blue ABS filament (HATCHBOX 3D, Pomona, CA, USA) was used for the printing of all tensile specimens. This filament was reported to have a diameter of 1.75 ± 0.03 mm and a recommended extrusion temperature of 210-240 °C [31]. The filament was dried overnight at 80 °C in a vacuum oven prior to printing and was returned to the oven when not in use.

3D models for the tensile specimens were selected according to ASTM D638-22 Type V with a thickness of 2 mm [32]. The slicer software Simply3D was used to generate print paths for specimens under six unique conditions: three different layer heights (0.2, 0.25, and 0.3 mm) with two different raster angles (0° and 90°), all with a build orientation flat on the print bed. The size and raster angles of the printed specimens are visualized in Figure 3.1.

Tensile specimens were manufactured using a Roboze One+400 Xtreme MatEx 3D printer (Roboze, Bari, Apulia, Italy) with a 0.4 mm diameter nozzle, an extruder temperature of 225 °C, and a print bed temperature of 90 °C. The print bed temperature was selected to minimize the cooling rate during printing while still cooling the material below the T_g of ABS which is about 105 °C [9]. Tensile specimens of each of the six conditions were printed sequentially in batches of five for a total of thirty specimens. The specimens were printed with about 15 mm of space between each other with each specimen #1 through #5 printed in the same location on the print bed to minimize variation between batches. The remaining process parameters were kept at set values and are summarized in Table 3.1.

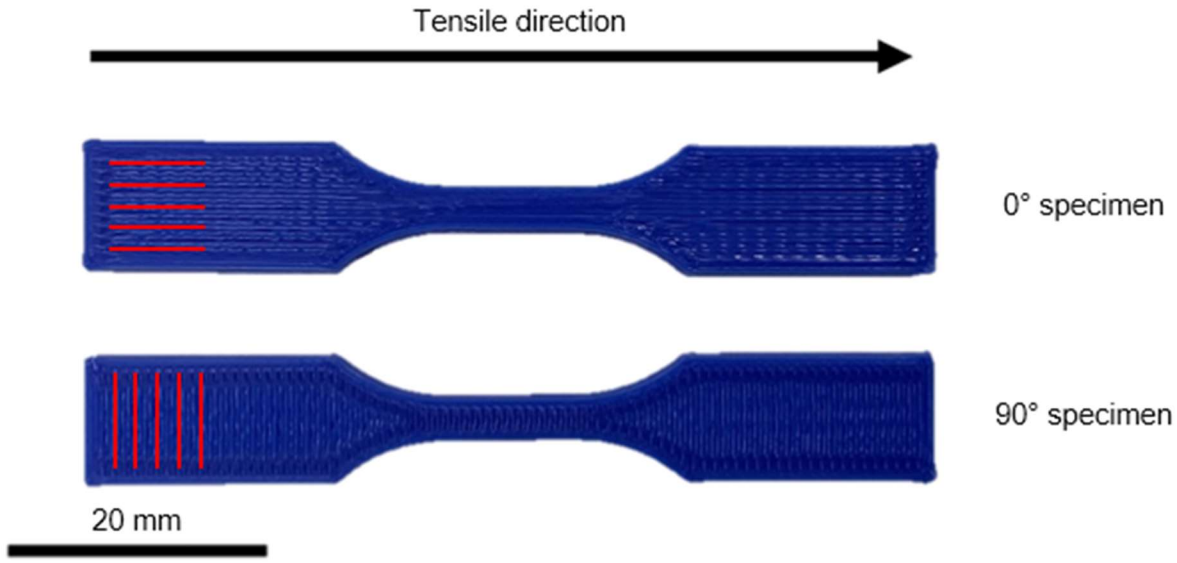

Figure 3.1: Photo of two 2 mm thick ASTM D638-22 Type V tensile specimens 3D printed flat on the print bed with raster angles of 0° and 90° relative to the tensile direction.

Table 3.1: Summary of process parameters for Type V tensile specimens.

Process parameter	**Set value**
Nozzle diameter	0.4 mm
Extrusion width	0.4 mm
Layer height	0.2 mm, 0.25 mm, 0.3 mm
Top solid layers	3
Bottom solid layers	3
Outline shells	2
Infill percentage	100%
Outline overlap	50%
Build orientation	Flat
Raster angle	0°, 90°
Extruder temperature	225 °C
Bed temperature	90 °C
Printing speed	3600 mm/min
Outline speed	50%
Solid infill speed	80%
First layer speed	50%

The width and thickness of the narrow section of each tensile specimen were measured for later use during mechanical testing calculations and were all found to be within the

dimensions and tolerances prescribed by ASTM D638-22 with widths 3.08 ± 0.02 mm and thicknesses 1.99 ± 0.09 mm [32]. The specimens were stored in a sealed bag with a desiccant to keep them dry until mechanical testing could be carried out.

3.2 Optical Profilometry

The top layer of the narrow sections of each of the thirty specimens were imaged via FVM based optical profilometry using a Zeta-20 Optical Profiler (Zeta Instruments, San Jose, CA, USA). A 50x magnification objective lens with a numerical aperture of 0.8 and working distance of 1.0 mm was used for all imaging. This configuration somewhat mitigated the errors caused by surfaces with steep slopes [25]. Combined with a 0.35x coupler and a 2/3" camera sensor, this configuration produced 466x349 μm images with a spatial resolution of 0.364 μm. The focus of the instrument was varied in increments of 0.50 μm. Images were automatically captured in 20x4 grids and manually aligned to form a single 3D SMM that covered about an 8390x1080 μm area centered on the narrow section of each specimen. The axes of the 3D SMM were defined such that the x-axis was parallel to the tensile direction, the y-axis ran along the width of the surface, and the z-axis was vertical. Additional scans were taken in the center of the grip sections on either end of three specimens (90°, 0.2mm, #1; 90°, 0.25mm, #1; and 90°, 0.3mm, #1) to better understand the surface morphology further from the edges of the specimen, but these scans were not used for correlations with the mechanical properties since all failures occurred in the narrow sections.

3.3 Tensile Testing

Uniaxial tensile testing was conducted according to ASTM D638-22 under ambient conditions with an MTS Criterion Model 43 load frame (MTS Systems, Eden Prairie, MN, USA) [32]. The load frame was equipped with a 1000 N load cell, self-tightening scissor action grips, and an MTS Advantage Video Extensometer 204. The narrow section of each specimen was marked to allow the extensometer to accurately track the strain of the material during testing. Tensile testing was conducted at a rate of 5 mm/min, fracturing all specimens within two minutes. Stress-strain curves for each specimen were plotted using the load data, each specimen's cross-sectional area, and strain data from the extensometer, from which the elastic modulus (E), ultimate tensile strength (σ_u), and elongation at break (ε_b) were calculated.

3.4 Fast Fourier Transform Analysis

The 3D SMMs obtained from optical profilometry were converted to the frequency domain via an FFT algorithm to quantify multiple parameters of the wavy surface. Due to software limitations, it was only practical to perform 1D transforms. As elaborated upon by Jiang et al., 2D transforms would be preferable due to the information lost when slicing a 3D surface into 2D line profiles [5]. First, the 3D SMM was sliced into a series of line profiles parallel to the x-axis spaced every 20 μm in the y-dimension. Each line profile was then cropped to only extend 8000 μm of the approximately 8390 μm long image. This was done due to the nature of FFT algorithms to categorize the waves within a signal into frequency bins that correspond to wavelengths that are unit fractions of the length of the input data (1/2, 1/3, 1/4, etc.) [33]. The amplitude of any waves in the signal with frequencies not corresponding to a single bin would be

split between the two closest bins, decreasing the accuracy of the FFT [33][34]. With the expectation that the 0.4 mm extrusion width that all the specimens were printed with would result in a 400 µm wave in the surface, each line profile was shortened to a multiple of 400 µm. The discrete Fourier transform (DFT) of each line profile was then computed with MATLAB using a set of FFT algorithms available in a library known as the Fastest Fourier Transform in the West (FFTW) [35]. Each DFT was converted into a single-sided amplitude spectrum (SSAS) describing the amplitude of each wave present in the surface with respect to frequency and combined to form a 3D representation of how the SSAS changes along the y-dimension. This process of converting the 3D SSM into a set of SSASs is visualized in Figure 3.2.

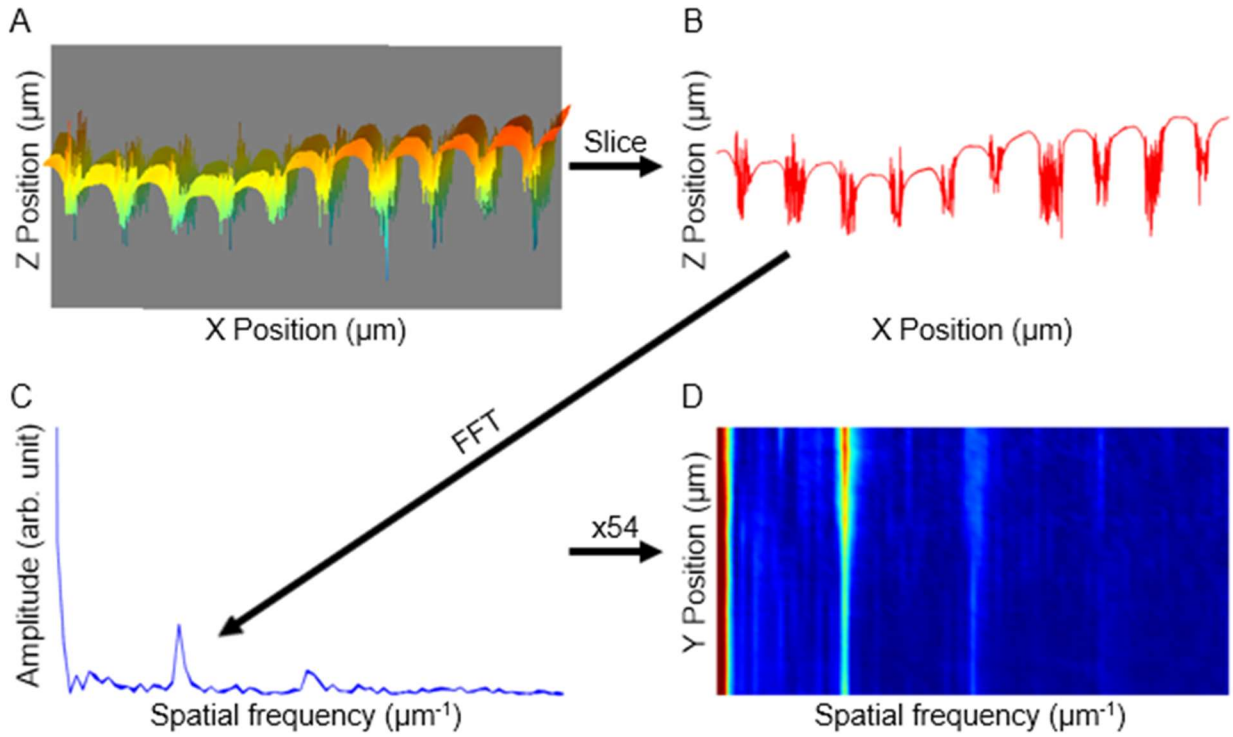

Figure 3.2: Process of converting a 3D surface morphology measurement (SMM) into a set of single-sided amplitude spectra (SSASs). (A) A 3D SMM is sliced with an xz-plane every 20 µm in the y-dimension; (B) producing line profiles which are then converted using a fast Fourier transform; (C) into an SSAS describing the waves contained within the individual line profile which is then combined with other SSASs; (D) forming a 3D representation of the SSASs with respect to the y-dimension.

The same process was attempted with line profiles parallel to the y-axis, but the DFT had too little resolution to be useful, even with interpolation, due to the inverse relationship of signal length with frequency bin size [34]. Consequently, information was only obtained for waves parallel to the x-axis/tensile direction, which are much more common in the specimens with a 90° raster angle as is evident by Figure 3.1.

Five unique parameters were calculated for the surface of each specimen and used for correlations with mechanical properties. The first parameter, $A_{800+400}$, was defined as the average combined amplitude of the two most intense waves present in these surfaces, located at 800 and 400 μm in the set of SSASs. This parameter acts as a measure of the height variation present in each surface related to these waves. Next, the average ratio of the amplitudes of these two waves was calculated for each surface to produce the parameter A_{800}/A_{400}. The parameter A_{Noise} is a measure of the background noise present in the set of SSASs for each surface. It was calculated by averaging the amplitude of each point of the 3D representation of the SSASs between 8000 and 10 μm in wavelength, excluding the wavelengths associated with the two fundamental waves and any harmonic peaks located at unit fractions of the two fundamental waves (266, 200, 133, 100 μm, etc.). The next parameters MAD_{800} and MAD_{400} were defined as the mean absolute deviation (MAD) of the amplitude of the respective wavelength along the y-dimension. This serves as a measure of how much the morphology of the surface changes along the y-dimension. The last parameters were the total harmonic distortion (THD) of each of the two fundamental waves, referred to as THD_{400} and THD_{800}. The THD is a measure of how distorted a wave is from perfectly sinusoidal according to the relative amplitude of the wave's harmonic frequencies but is most frequently used in audio and electrical engineering [35]. The THD is defined as the ratio of the sum of the root mean square (RMS) amplitudes of all the harmonics to the RMS

amplitude of the fundamental wave, but peak amplitudes were used instead since RMS and peak amplitudes are directly proportional for sine waves [35]. The parameters and their corresponding equations are summarized in Table 3.2.

Table 3.2: List of the parameters used for correlations with mechanical properties.

Parameter	**Equation**
Combined Peak Amplitude	$A_{800+400} = mean\big(A_{800}(y) + A_{400}(y)\big)$
Peak Amplitude Ratio	$A_{800}/A_{400} = mean\left(\frac{A_{800}(y)}{A_{400}(y)}\right)$
Background Noise Amplitude	$A_{Noise} = mean(A(\lambda, y) - A_{800}(y) - A_{400}(y) - A_{266}(y) - A_{200}(y) - \cdots)$
Absolute Deviation	$MAD_{\lambda} = mean\big(\big\lvert A_{\lambda}(y) - mean\big(A_{\lambda}(y)\big)\big\rvert\big)$
Harmonic Distortion	$THD_{\lambda} = mean\left(\frac{\sqrt{{A_{\lambda/2}}^2 + {A_{\lambda/3}}^2 + {A_{\lambda/4}}^2 + \cdots}}{A_{\lambda}}\right)$

Chapter 4

Results and Discussion

4.1 Mechanical Properties

Figure 4.1 shows the stress-strain curves obtained during the tensile testing of all the specimens. The stress-strain curves for three specimens were discarded and these specimens will be excluded from all correlations. Specimen 0°, 0.2mm, #4 only partially fractured due to the delamination of a few roads from the outside of the specimen, resulting in the premature termination of testing. The extensometer failed to properly track the strain for specimens 0°, 0.3mm, #5 and 90°, 0.25mm, #5. The stress-strain curves appear to be relatively consistent across and within each of the six print conditions, though most specimens seem to either fracture around 4% strain or elongate significantly further to 8% strain before fracturing. No trend between ε_b and the location of fracture (in the center of the narrow section or closer to where the specimen begins to widen) was observed.

The distribution of each of the studied mechanical properties (E, σ_u, ε_b) for each of the six conditions is shown in Figure 4.2. The average mechanical properties are within expected ranges as compared with Shubham et al., though some specimens surpassed the properties displayed by injection molded ABS with σ_u = 36 MPa and ε_b = 5.8% [9]. The variation present for each property is consistent with the 5.63% for E, 9.97% for σ_u, and 52.9% for ε_b identified by Faes et al. [36]. There may be a positive trend of both σ_u and ε_b with layer height for the specimens printed with a 90° raster angle, but the variation present in these values brings the significance of this trend into question.

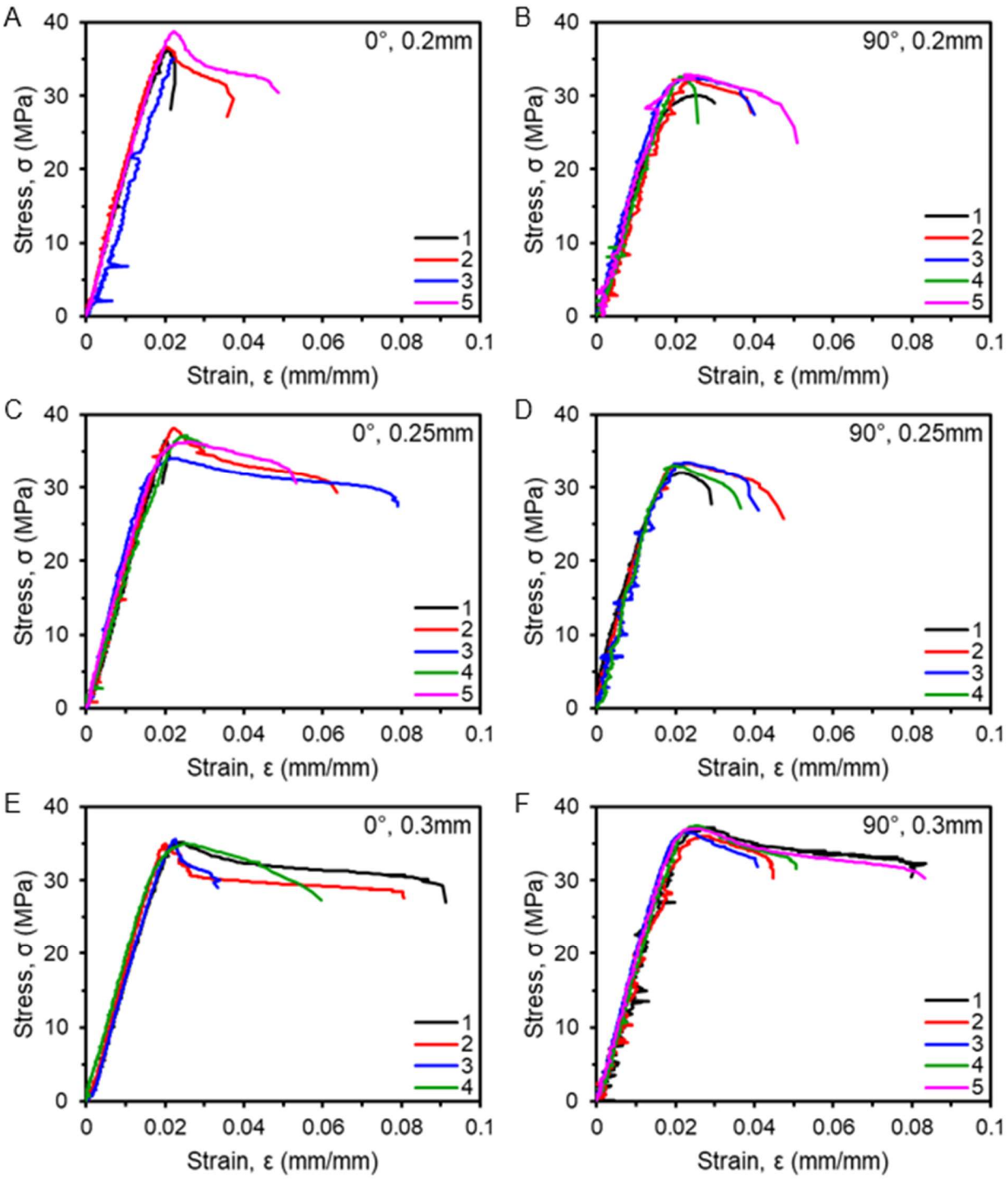

Figure 4.1: (A-F) Stress-strain curves produced from the uniaxial tensile testing of Type V tensile specimens according to ASTM D638-22. Each panel is labeled with the batch's raster angle and layer height.

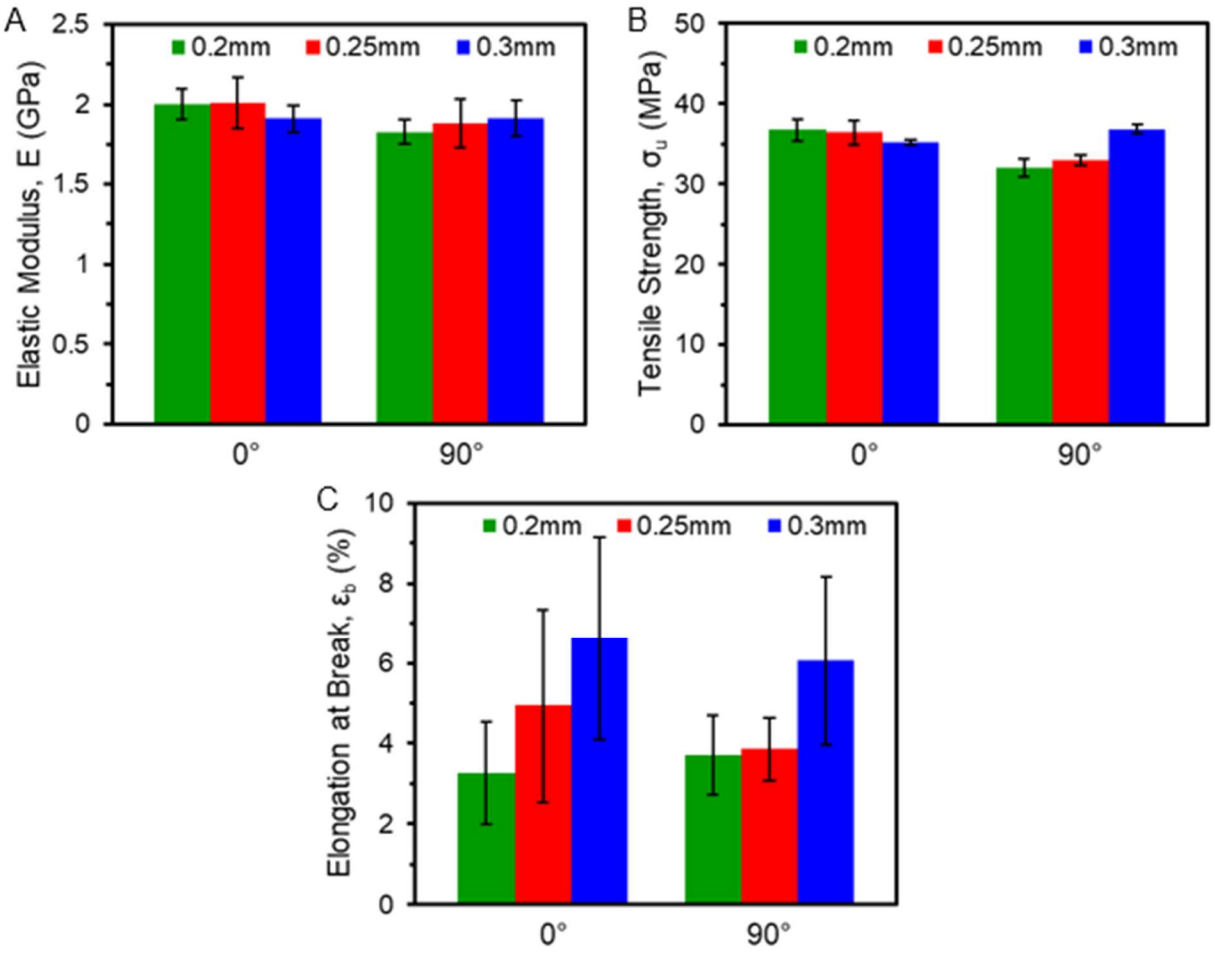

Figure 4.2: Average mechanical properties of specimens printed under each of the six conditions. (A) Elastic modulus; (B) ultimate tensile strength; (C) and elongation at break were calculated for each condition. Error bars represent the standard deviation of the corresponding property in each batch.

Overall, neither layer height nor raster angle had a significant effect on E, σ_u, or ε_b. This is counter to the inferior mechanical properties for increasing raster angle as reported by Ahn et al. and for increasing layer height as found by Shubham et al. [8][9]. A partial explanation for this is offered by Sola et al. where it was found that decreasing specimen size decreased but did not eliminate the difference in mechanical properties between 0° and 90° specimens [37]. The mechanism behind this effect can be explained by the change in intra-layer cooling time explored by Ai and Vogt [19]. The small Type V tensile specimens used in the present study would have a

lower cooling time between roads for the 90° raster angle than for the 0° raster angle, resulting in better intra-layer adhesion and improved mechanical properties.

4.2 Surface Morphology Measurements

The 3D SMMs of the center of the grip sections of specimens printed at each of the three layer heights are presented in Figure 4.3. These scans show the typical surface morphology far from the edges of the specimen where the extrusion nozzle is assumed to be moving at a constant speed and flow is fully developed. The roads shown in the 0.2 mm specimen have flat top surfaces and appear to have made good contact between each other for the most part. This morphology closely resembles that modeled in Figure 2.1 and is well explained by the higher contact pressure present for lower layer heights. This suggests that the grip section of this specimen has superior inter-layer contact compared to those with more rounded road tops [6]. There are a few defects where neighboring roads did not make contact, resulting in a hole down to the underlying layer. The 0.25 mm specimen has roads with more rounded tops and poorer contact between neighboring roads with frequent holes. The roads making up the 0.3 mm specimen's surface have even more rounded tops but appear to have made better contact with neighboring roads than observed for the 0.25 mm specimen. The surface of this specimen is also not completely level with the left half lower than the right.

The narrow sections of the tensile specimens are generally much flatter than the grip sections as seen in Figure 4.4 of representative narrow sections of 0° specimens printed at each layer height (note the change in scale bar). These three specimens follow a similar trend to the imaged grip sections in terms of having flatter road tops at lower layer heights. Unlike the grip

sections, the contact between roads appears to be best at a layer height of 0.3 mm, whereas the 0.2 mm and 0.25 mm specimens each only have intermittent contact along the interface in the center of the image. The stringy defects on parts of the surfaces of the 0.2 mm and 0.3 mm specimens will become relevant when viewing the FFT output.

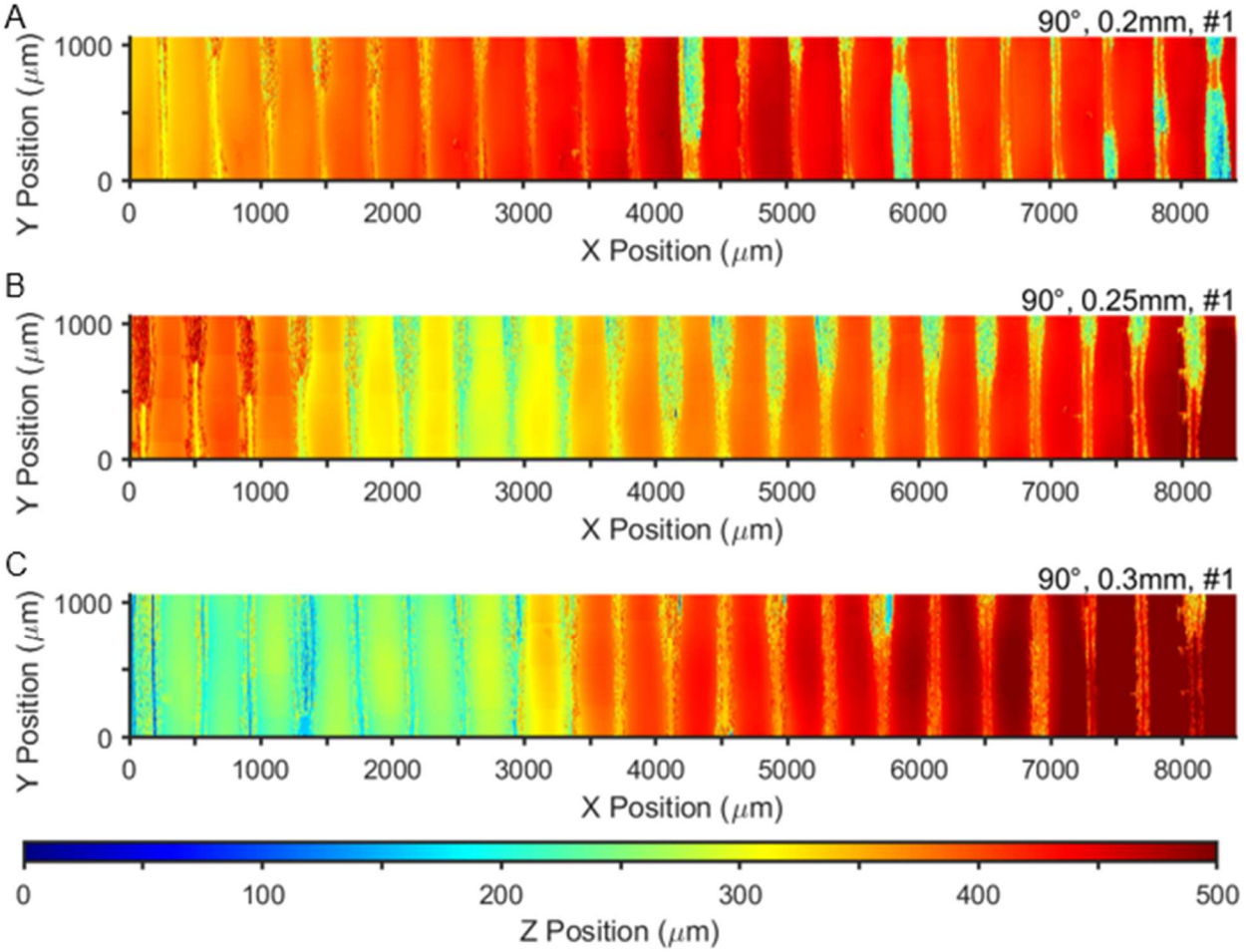

Figure 4.3: 3D surface morphology measurements of the grip sections of 90° raster angle specimens printed with layer heights of (A) 0.2 mm; (B) 0.25 mm; (C) and 0.3 mm.

Figure 4.5 shows representative 3D SMMs for the 90° specimens of each layer height. All three surfaces display starkly different morphologies than in Figures 4.3 and 4.4 due to the path of the extrusion nozzle turning back on itself near the edges of the specimen. The surface of the 0.2 mm specimen is very flat and smooth with excellent intra-layer contact on the left side,

but the morphology shifts slightly around x = 5000 µm such that periodic ovoid holes remain unfilled. The 0.25 mm specimen has a similar morphology that is flat in most areas with small ovoid holes between each road. The increase in layer height up to 0.3 mm yields a drastic change in surface morphology with no holes open to the underlying layers, only what can be described as flat-bottomed valleys. The difference between the two can be seen due to the noise present in and around holes due to the steep slopes of the surface in those regions [25]. The 0.3 mm specimen also has significant stringing of material across the surface, especially near where the nozzle turned around.

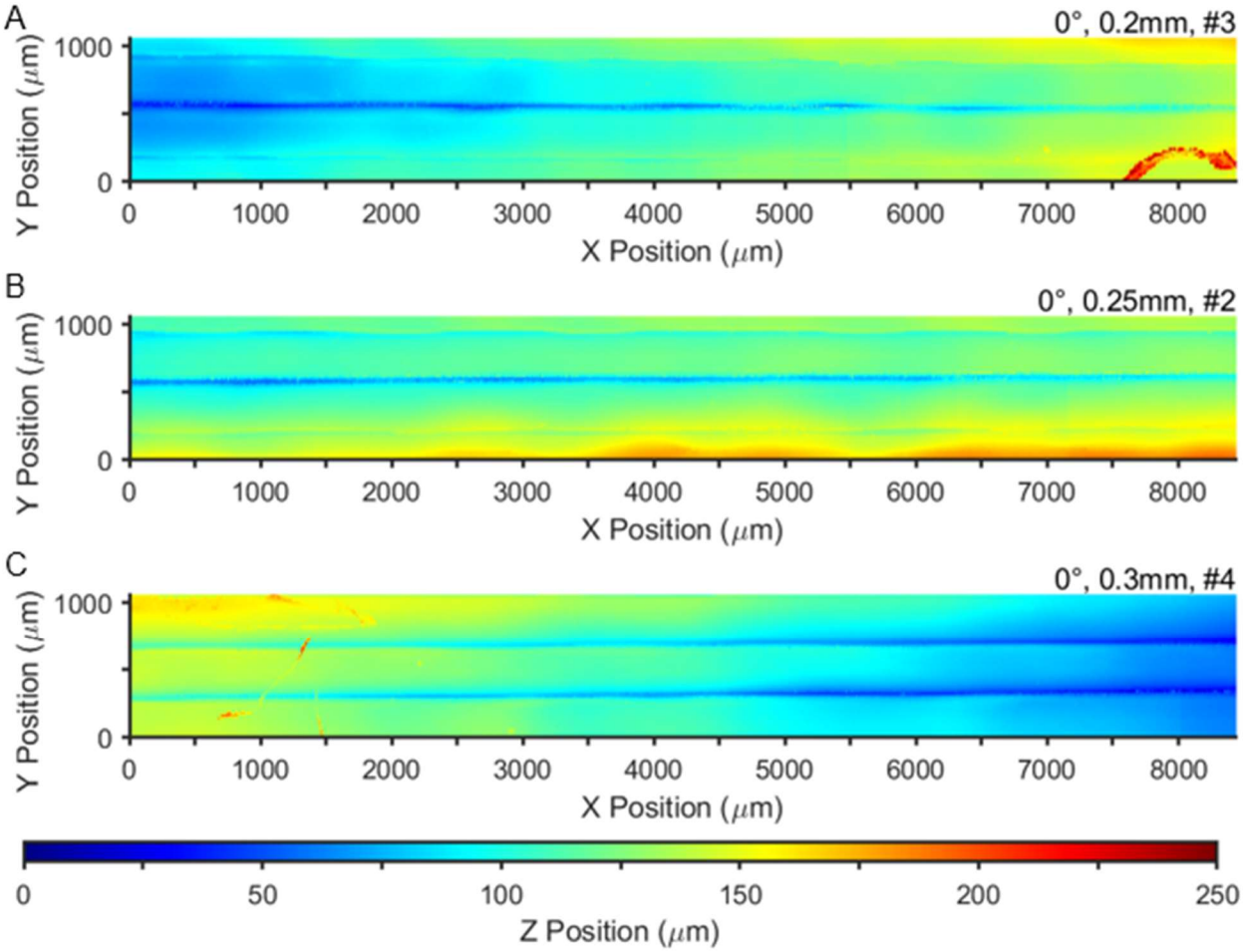

Figure 4.4: Representative 3D surface morphology measurements of the narrow sections of 0° raster angle specimens printed with layer heights of (A) 0.2 mm; (B) 0.25 mm; (C) and 0.3 mm.

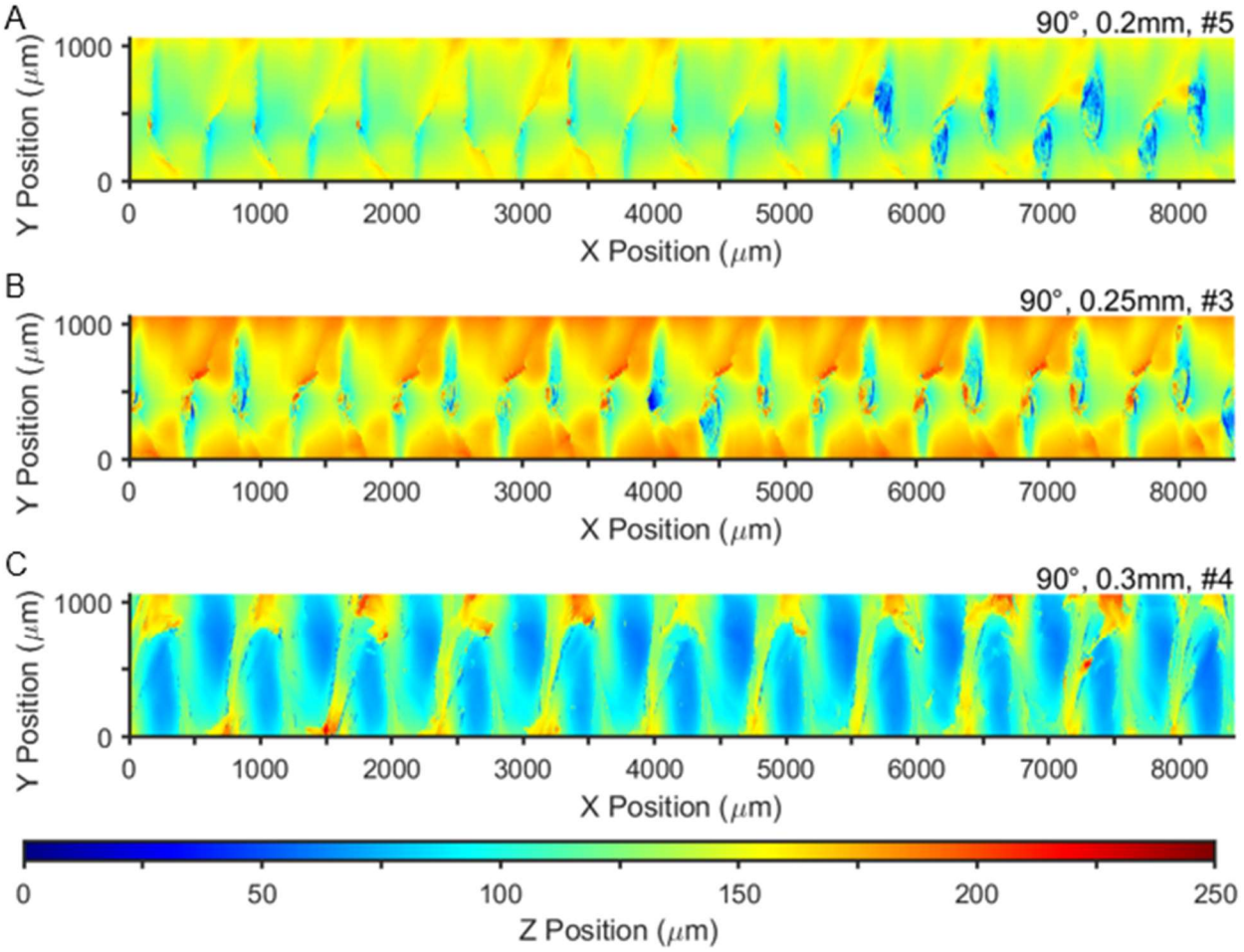

Figure 4.5: Representative 3D surface morphology measurements of the narrow sections of 90° raster angle specimens printed with layer heights of (A) 0.2 mm; (B) 0.25 mm; (C) and 0.3 mm.

Examining all the specimens within a single print condition as is done in Figure 4.6 provides further insights into the surface morphology behind the observed mechanical properties, especially the magnitude of their variation. All remaining 3D SMMs are provided in Figure A.1. Although these five specimens were manufactured sequentially during a single print operation and with identical process parameters, there are a wide variety of surface morphologies. The 0.2 mm and 0.25 mm specimens in Figure 4.5 look more similar to each other than many of those in Figure 4.6. With such dissimilar surfaces, it is unsurprising that the mechanical properties of additively manufactured plastics vary as much as they do.

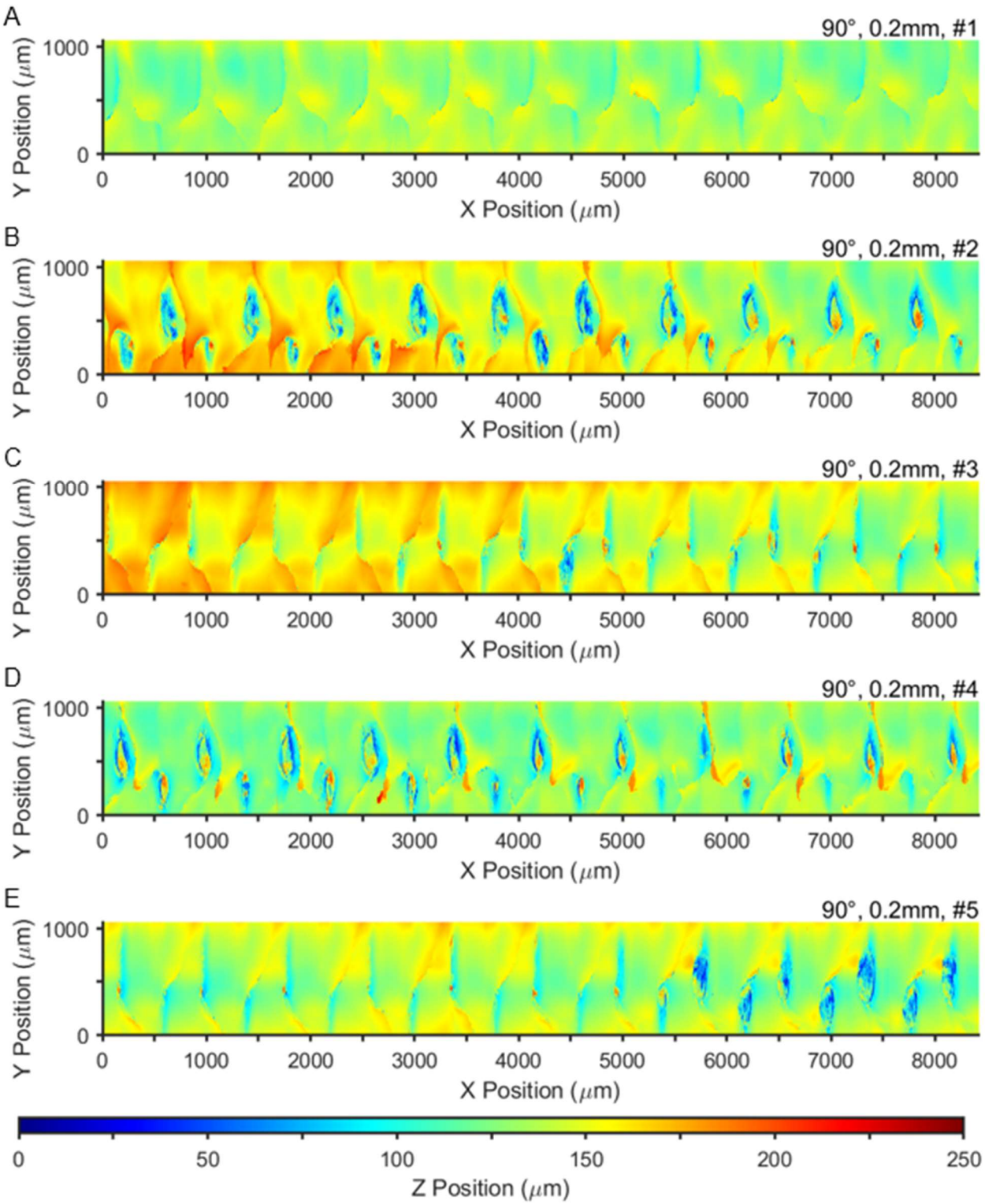

Figure 4.6: (A-E) All five 3D surface morphology measurements of the narrow sections of the 90° raster angle, 0.2 mm layer height specimens.

In order of smoothest surface with the least defects in intra-layer contact like holes to that with the most, the 90°, 0.2 mm specimens go #1, #3, #5, #4, #2. One might expect that the smoother surface with less defects and holes would possess superior mechanical properties, but specimen #1 had an average E, the lowest σ_u, and the second lowest ε_b of the five. #3 was the highest E specimen while #5 has the highest σ_u and ε_b. Evidently, this visual comparison of the surfaces is inadequate for evaluating the mechanical properties. A more quantitative method able to discern characteristics of the surface difficult to perceive by eye is necessary.

4.3 Fast Fourier Transform Spectra

Returning to the 3D SMMs of the grip sections in Figure 4.3 with 3D representations of SSASs obtained from a series of FFTs will help to better visualize and then quantify the concepts of the roundness of the tops of and the intra-layer contact between the printed roads. Figure 4.7 shows the sets of SSASs representing the same three surfaces of the grip sections as in Figure 4.3. Each set of SSASs has four key features: the zero-frequency (infinite wavelength) peak, a fundamental peak at $\lambda = 400$ μm, harmonic peaks, and background noise.

The zero-frequency peak is located on the far-left side of each set of SSASs. The amplitude of this peak corresponds to the average height of the surface above $z = 0$ μm. This height is arbitrary based on the bounds set during optical profilometry, so the zero-frequency peak can be ignored. The zero-frequency peak for the 0.3 mm specimen extends to the right to about $\lambda = 1600$ μm due to the presence of low frequency waves that account for the unlevel nature of that surface.

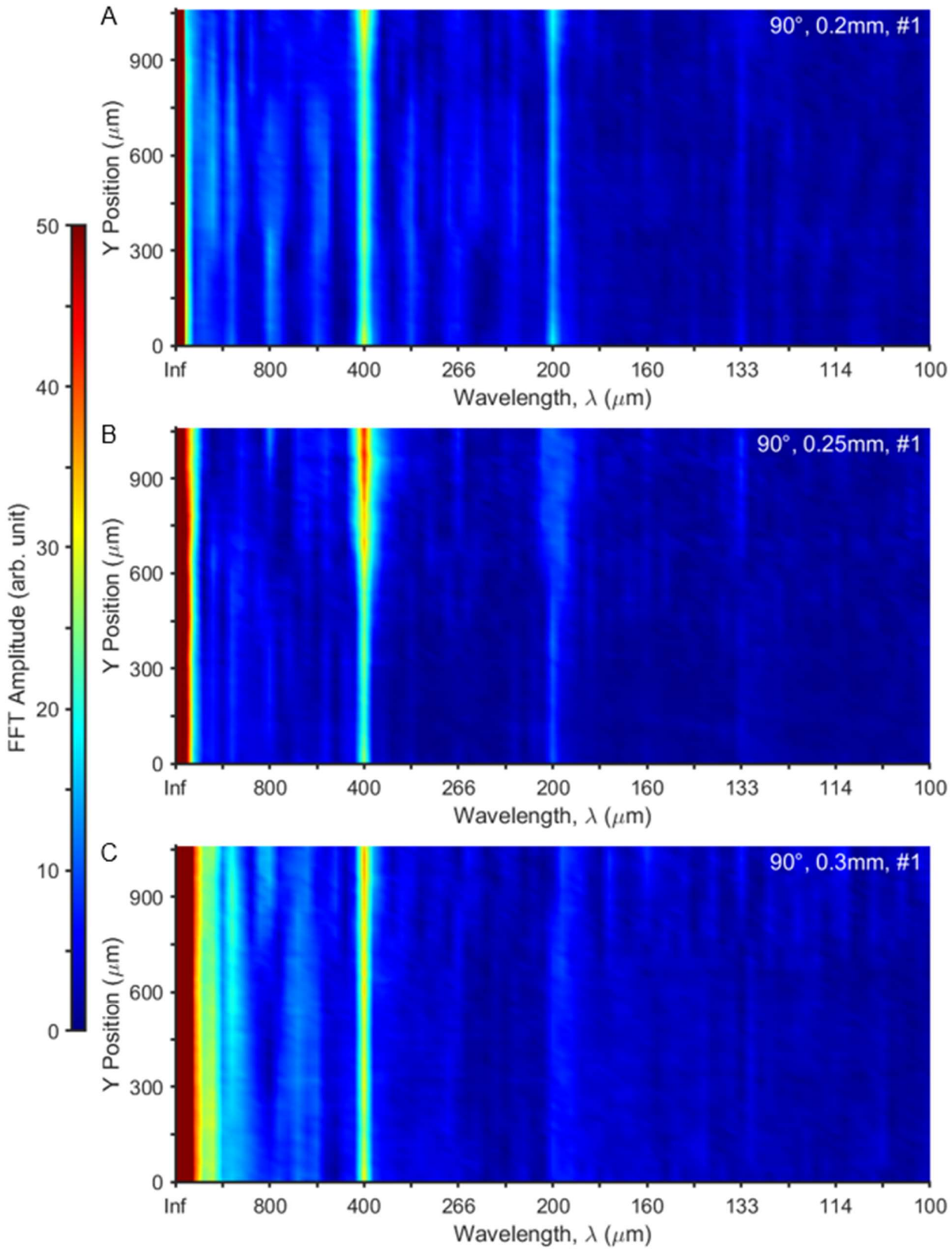

Figure 4.7: (A-C) Single-sided amplitude spectra of the grip sections from Figure 4.3.

The fundamental peak is the first and highest amplitude peak after the zero-frequency peak which is located at $\lambda = 400$ μm for these specimens. This 400 μm wave is a large component of these surfaces due to the 0.4 mm extrusion width that all the specimens were printed with. This peak is weakest for the 0.2 mm grip section and increases in amplitude with the layer height since its amplitude is a measure of the height variation of the surface every 400 μm. This indicates that the surface of the grip section is flatter at lower layer heights. The additional amplitude of the fundamental peak around $y = 900$ μm for the 0.25 mm specimen indicates that the height variation is higher at that location, due to the poor intra-layer contact for that specimen in Figure 4.3.

Harmonic peaks occur at unit fractions of the fundamental peak which is clearest for the 0.2 mm surface where there is a peak at $\lambda = 200$ μm and a weaker one at $\lambda = 133$ μm. These harmonic peaks occur because the wave that forms the surface of the specimen is not perfectly sinusoidal but distorted to be more like a square wave. The amplitude of the harmonic peaks relative to that of the fundamental peak indicates how distorted the wave is from sinusoidal. For these three surfaces, the harmonic peaks are strongest at lower layer heights, meaning that the 0.2 mm surface has flatter road tops while the tops of the 0.3 mm surface's roads are more curved.

Lastly, all the amplitude between the fundamental peak and its harmonics is likely background noise. The randomness of the noise in the steep sloped areas and gaps in these surfaces acts as a set of waves with a distribution of frequencies, like white noise. The amount of noise in all these SSASs makes sense considering the number of holes and defects present in the original three surfaces.

Since the line profiles used to create these sets of SSASs were parallel to the x-axis, they were not expected to produce any large peaks for the specimens with a 0° raster angle. The

SSASs corresponding to the surfaces presented in Figure 4.4 are presented in Figure 4.8 and confirm the lack of significant waves parallel to the road direction. The only visible features in the SSASs of the 0° specimens are noise from the interfaces and gaps between neighboring roads and from the stringy defects on parts of the surfaces of the 0.2 mm and 0.3 mm specimens. These defects effectively smear across the SSASs due to the harmonics corresponding to the width of the defects at a given y-position.

Figure 4.9 shows the sets of SSASs obtained from the surfaces presented in Figure 4.5. Viewing the narrow sections of these 90° raster angle specimens in the frequency domain instead of the spatial domain reveals a few key features. Each of the three representative specimens has higher amplitude harmonics and more of them, suggesting that the morphology of surfaces in the narrow sections are less sinusoidal and more distorted than in the grip sections. The harmonics are spaced closer together because half of them originate from the $\lambda = 400$ μm peak as in the grip section, while the other half are exclusively due to a new $\lambda = 800$ μm peak that was not identifiably present in any of the grip section surfaces. This peak is thought to be caused by the extrusion nozzle turning around when it nears the edge of the specimen, producing a series of U-turns that are double the extrusion width of 0.4 mm. The boundaries between this turnaround region at either edge of the specimen and a more regular region where the $\lambda = 400$ μm wave is dominant are clear in the SSAS for the 0.3 mm, where the $\lambda = 800$ μm peak has a high amplitude at the top and bottom of the image while the $\lambda = 400$ μm peak is highest around the low point of the $\lambda = 800$ μm peak around $y = 500$ μm. This effect is weaker for the 0.2 mm and 0.25 mm specimens. The $\lambda = 400$ μm peak in the 0.25 mm specimen appears to mostly consist of the 2nd harmonic of the $\lambda = 800$ μm peak due to the similarity of the two peaks' profiles along the y-dimension.

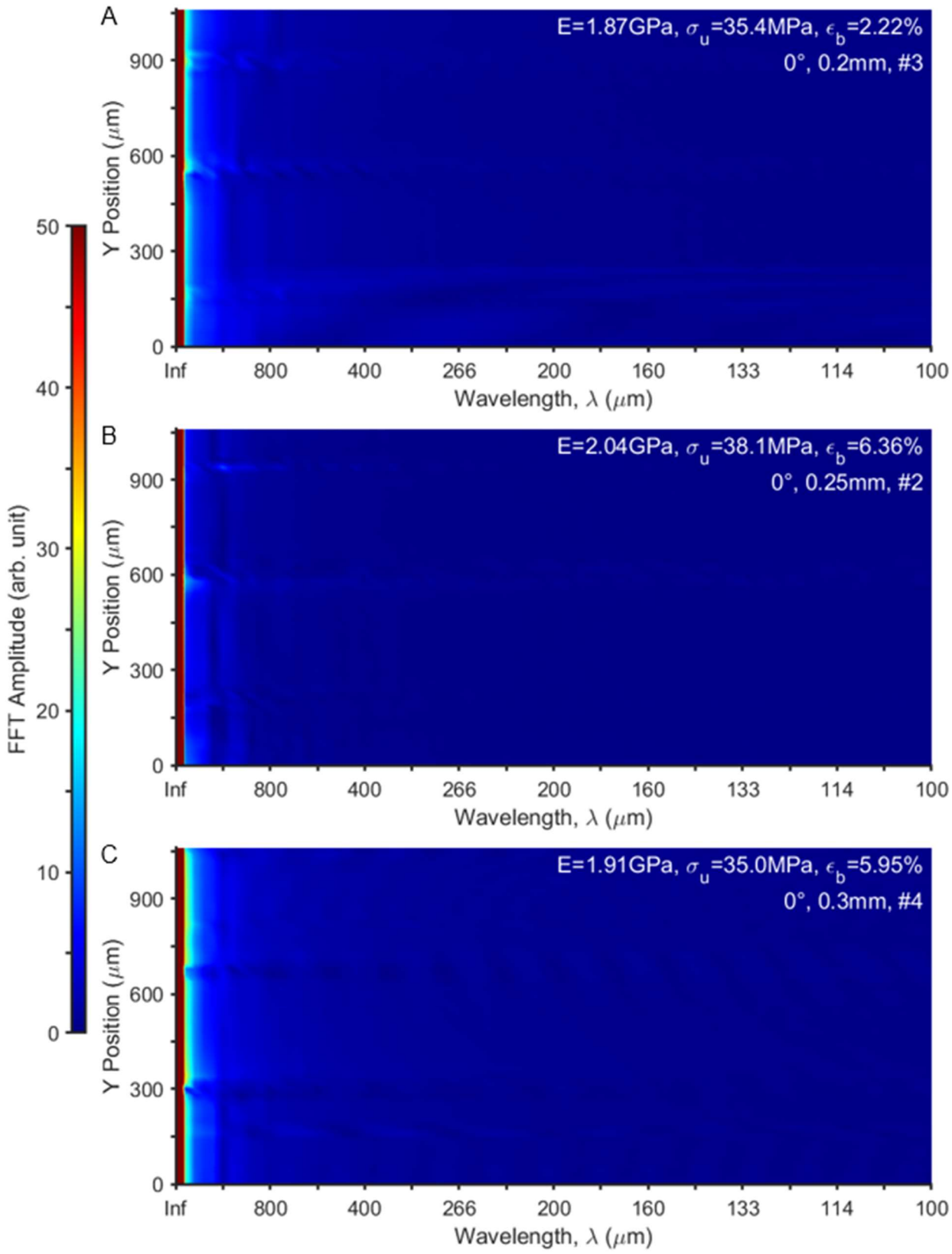

Figure 4.8: (A-C) Single-sided amplitude spectra of the 0° specimens from Figure 4.4.

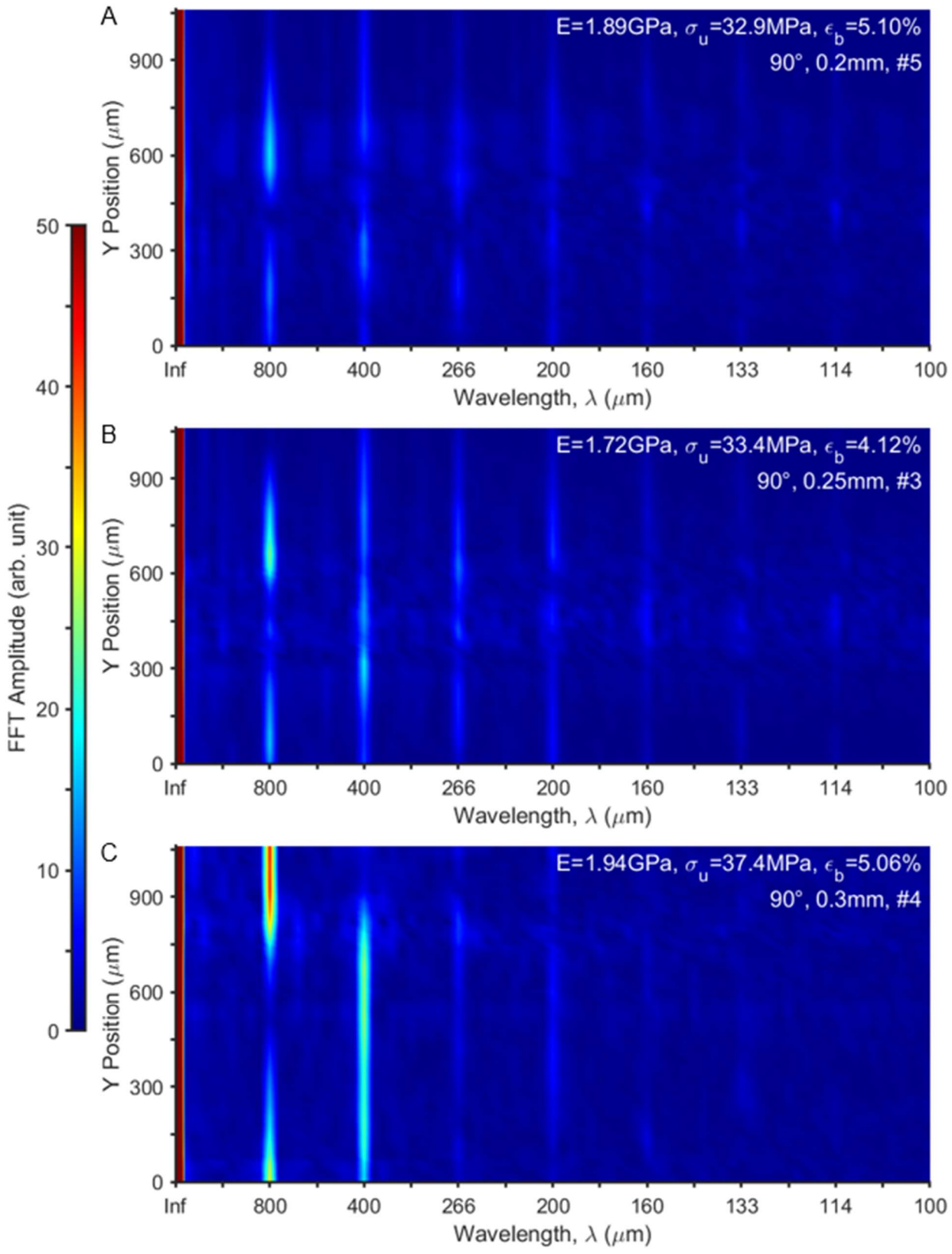

Figure 4.9: (A-C) Single-sided amplitude spectra of the 90° specimens from Figure 4.5.

The same spectral analysis can be applied to the set of five 90° raster angle, 0.2 mm layer height specimens shown in Figure 4.6, resulting in the five sets of SSASs in Figure 4.10. These five specimens all have a similar wave structure consisting of a high amplitude $\lambda = 800$ μm peak followed by a lower amplitude $\lambda = 400$ μm and all the possible harmonics. The profile of each peak and harmonic along the y-dimension consists of the same general pattern with two maxima towards the middle of the width of the surface. Of the five specimens, specimen #1 has uniquely low amplitudes for all of its peaks, corresponding to the flat surface observed in Figure 4.6. This difference could contribute to the lower σ_u of specimen #1 compared to the other four specimens.

Figure 4.11 and Figure 4.12 present the three 90° specimens with the highest and lowest E respectively, allowing for a qualitative correlation of the surface morphology with the mechanical properties. There is no clear feature that separates the high modulus surfaces from the low modulus ones. The two lowest modulus surfaces have spectra with moderately strong $\lambda =$ 800 μm and 400 μm peaks along with clear harmonics for both fundamental peaks but so do the spectra of the highest modulus surface. All specimens also appear to have similar amounts of background noise.

Performing the same comparison with the three 90° specimens with the highest and lowest σ_u, as shown in Figure 4.13 and Figure 4.14 respectively, yields more interesting results. All three of the highest strength specimens have a very similar wave structure consisting of two high amplitude peaks at $\lambda = 800$ μm and 400 μm followed by only weak harmonics below $\lambda =$ 200 μm. The low strength specimens have lower amplitude fundamental peaks and a variety of harmonic amplitudes. The visible connections between strong fundamental peaks and weak harmonics with increased strength are promising for the application of the two parameters that measure those aspects of the SSAS that correspond to those properties, $A_{800+400}$ and THD_{λ}.

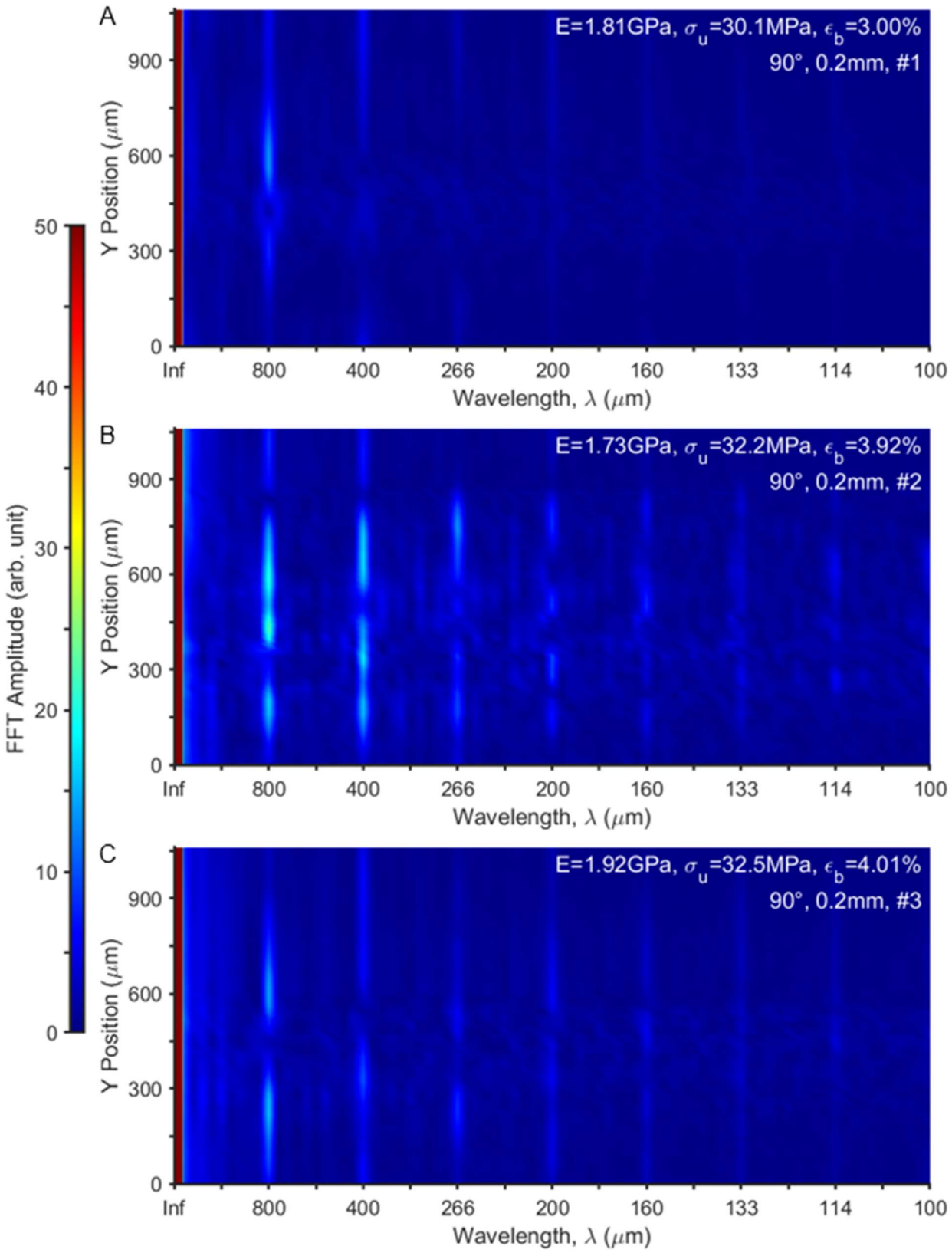
A
E=1.81GPa, σ_u=30.1MPa, ϵ_b=3.00%
90°, 0.2mm, #1
B
E=1.73GPa, σ_u=32.2MPa, ϵ_b=3.92%
90°, 0.2mm, #2
C
E=1.92GPa, σ_u=32.5MPa, ϵ_b=4.01%
90°, 0.2mm, #3
Y Position (μm)
0
300
600
900
Inf
800
400
266
200
160
133
114
100
Wavelength, λ (μm)
FFT Amplitude (arb. unit)
0
10
20
30
40
50

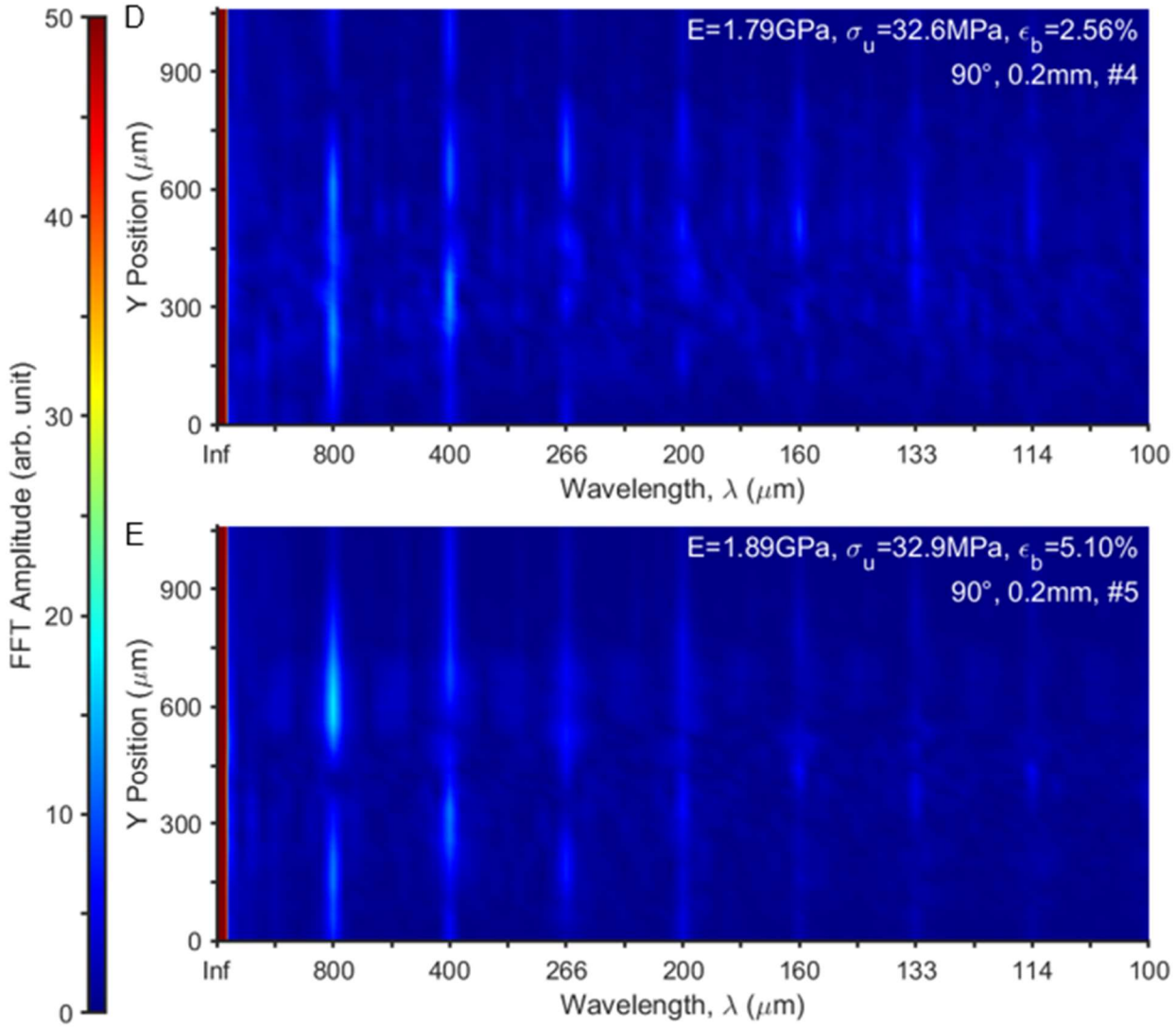

Figure 4.10: (A-E) Single-sided amplitude spectra of all five 90°, 2 mm specimens from Figure 4.6.

Figure 4.15 and Figure 4.16 compare the SSASs of the specimens with the highest and lowest ε_b, respectively. This yields a similar relationship as observed for σ_u, where higher amplitude fundamental peaks and lower amplitude harmonics are more likely to result in longer elongations before fracture. All remaining SSASs are given in Figure A.2.

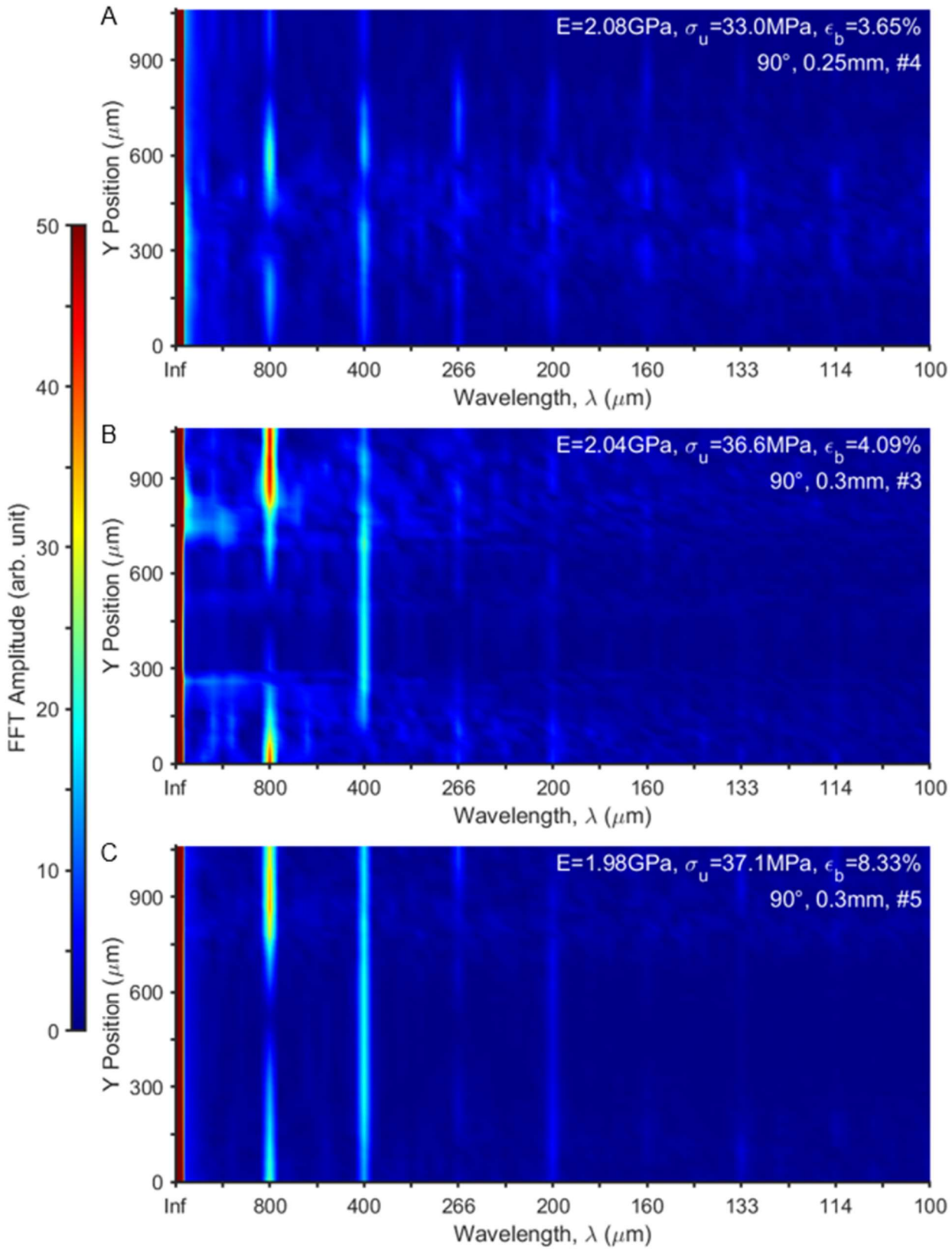

Figure 4.11: (A-C) Single-sided amplitude spectra of the highest modulus 90° specimens.

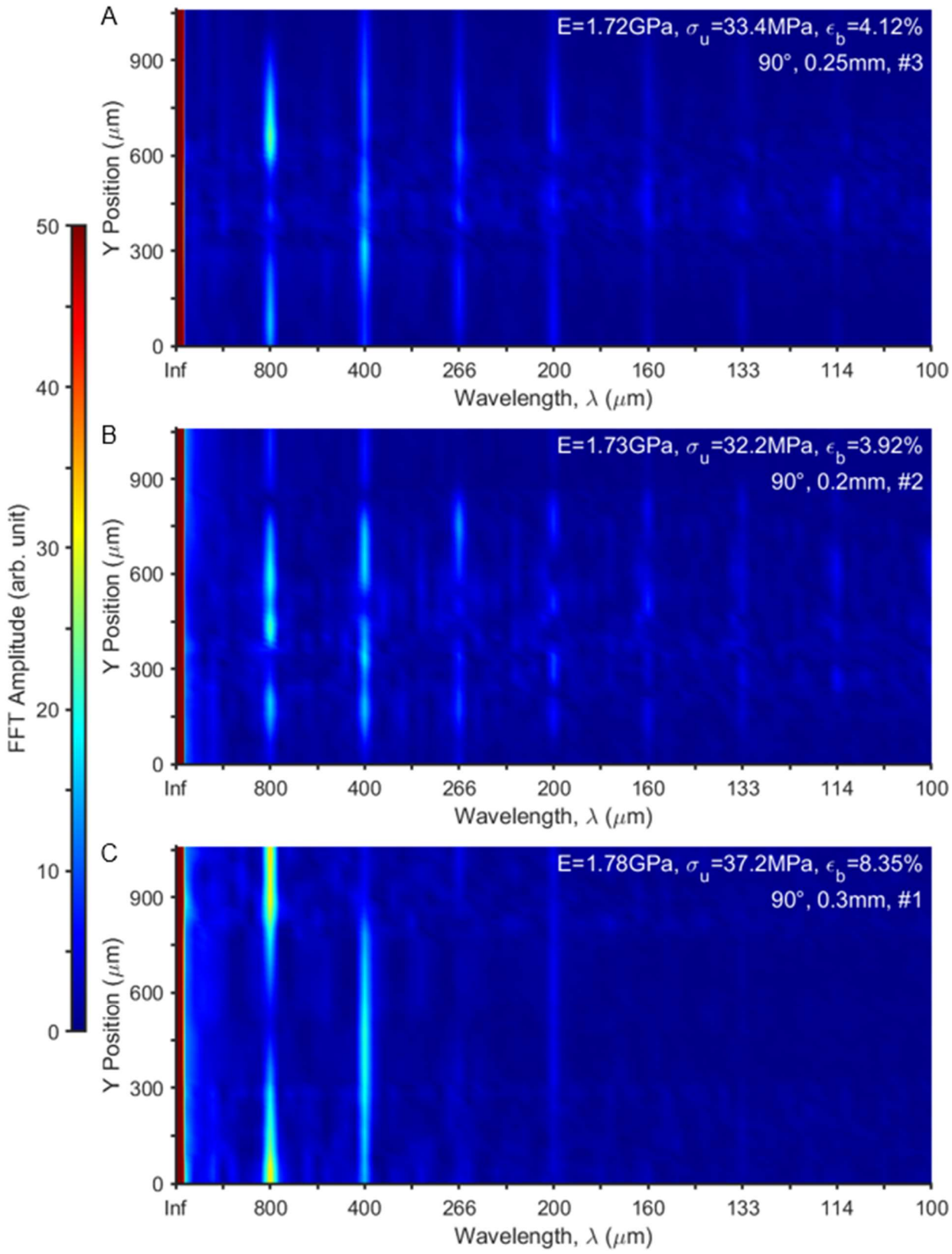

Figure 4.12: (A-C) Single-sided amplitude spectra of the lowest modulus 90° specimens.

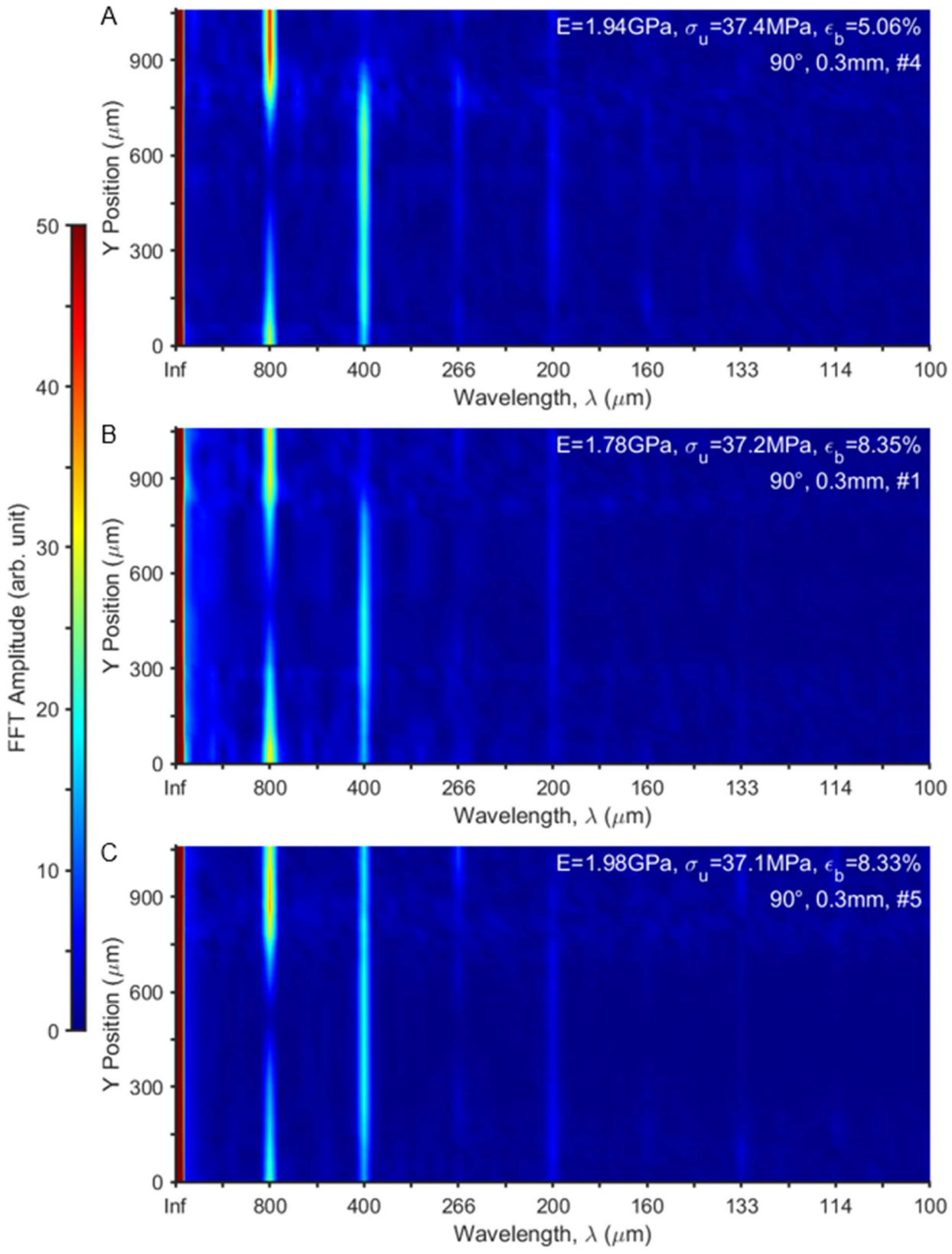

Figure 4.13: (A-C) Single-sided amplitude spectra of the highest strength 90° specimens.

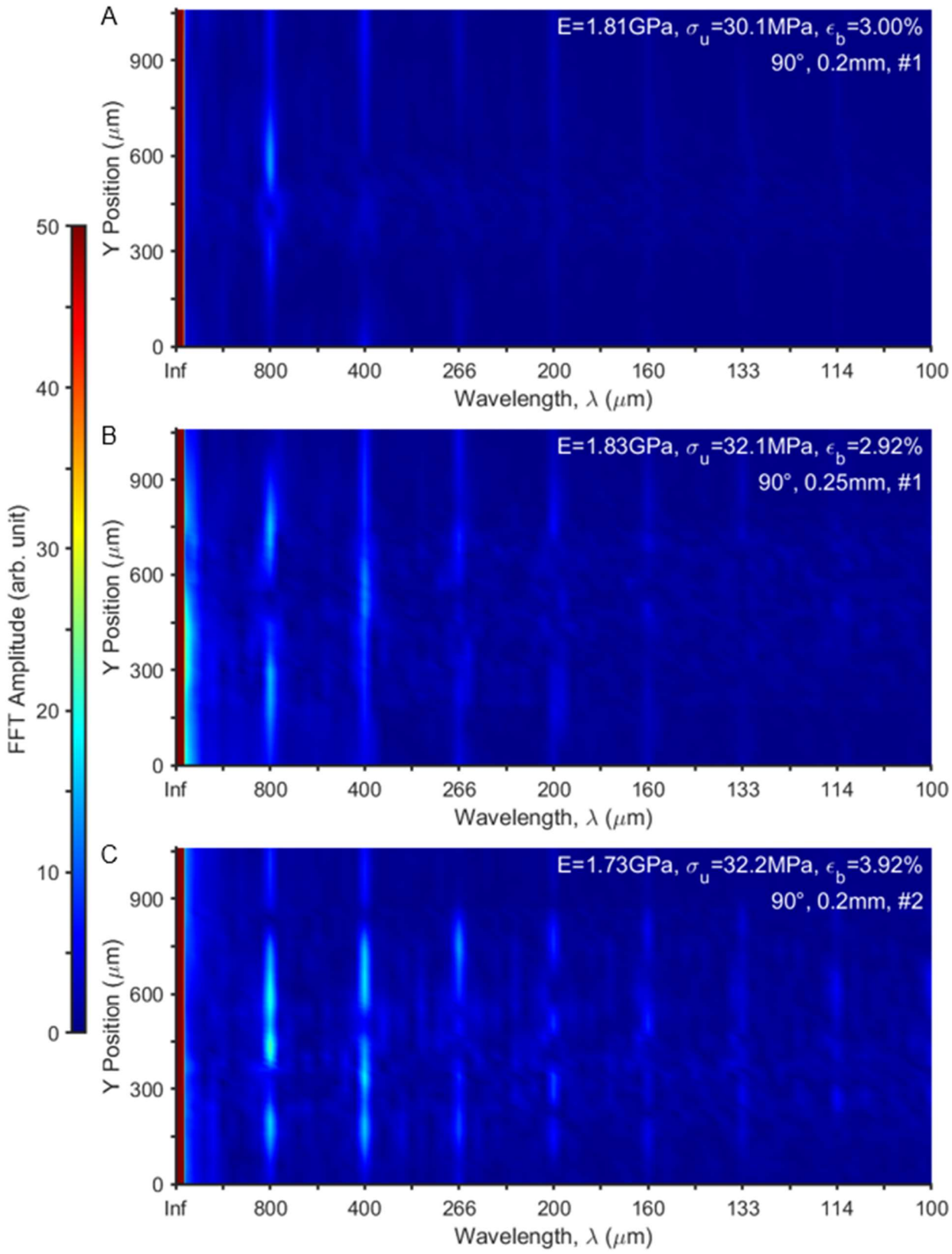

Figure 4.14: (A-C) Single-sided amplitude spectra of the lowest strength 90° specimens.

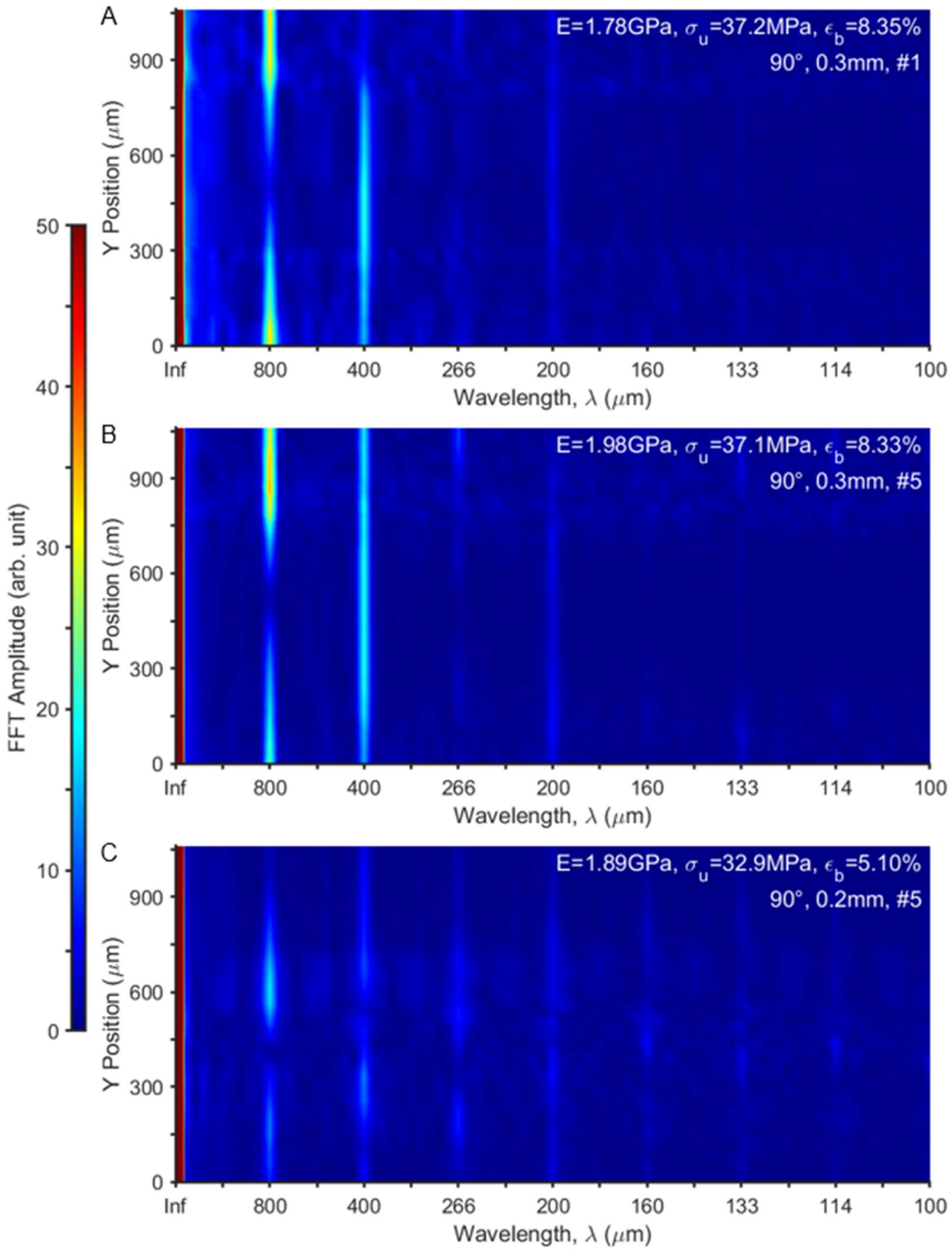

Figure 4.15: (A-C) Single-sided amplitude spectra of the highest elongation 90°specimens.

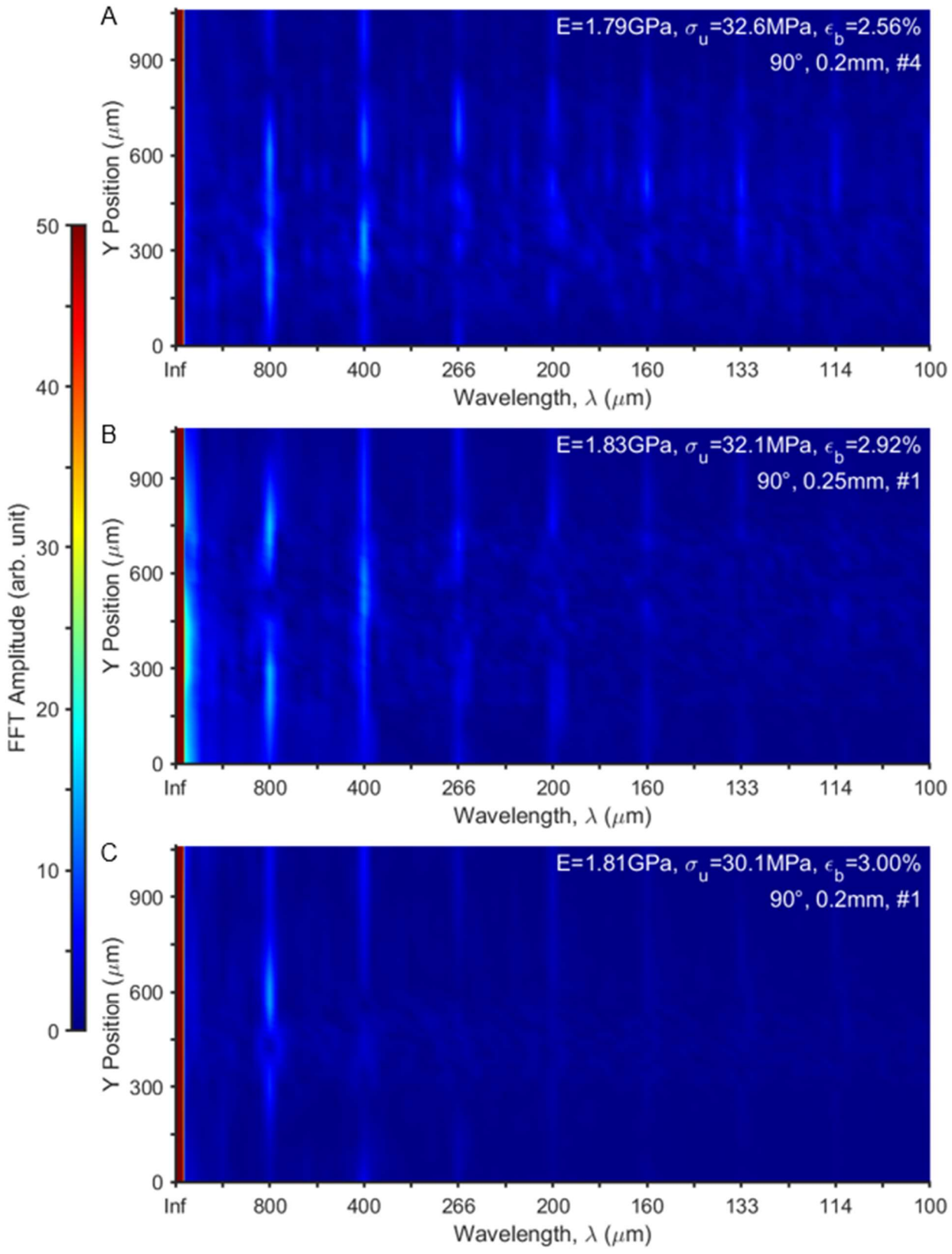

Figure 4.16: (A-C) Single-sided amplitude spectra of the lowest elongation 90° specimens.

4.4 Quantification and Correlation of Surface Parameters

Each of the five main qualities of the SASSs mentioned in the previous section were quantified using their respective parameters. The amplitudes of the two fundamental peaks, the ratio of the two fundamental peaks, the amount of background noise, the change of the fundamental amplitudes along the y-dimension, and the relative amplitude of the harmonics were defined by $A_{800+400}$, A_{800}/A_{400}, A_{Noise}, MAD_{λ} and THD_{λ}, respectively. The MAD and THD were applied to the λ = 800 μm and 400 μm separately, resulting in a total of seven parameters including $A_{800+400}$, A_{800}/A_{400}, A_{Noise}, MAD_{800}, MAD_{400}, THD_{800}, and THD_{400}.

Figure 4.17 correlates the first of these parameters, $A_{800+400}$, with each of the three measured mechanical properties, E, σ_u, and ε_b, using a linear trend. The average combined peak amplitude effectively sorted the specimens printed with each of the three layer heights into three clusters with some overlap between the 0.2 mm and 0.25 mm specimens. These clusters did not form a clear trend when plotted against the modulus or elongation data, resulting in low coefficient of determination (R^2) values of 0.091 and 0.396. However, plotting against the strength data resulted in a strong correlation with R^2 = 0.929. The positive slope of the trendline indicates that specimens with higher values of $A_{800+400}$ also tend to have a higher σ_u. This may help to address the unusual behavior of the tensile strength with respect to layer height where larger layer heights resulted in higher strengths. Larger layer heights result in less contact pressure being applied to the material as it is extruded, doing less to flatten the surface, instead forming larger height variations in the surface, increasing $A_{800+400}$, and by an unknown mechanism, σ_u. Related parameters like the average amplitude of the λ = 800 μm peak, A_{800}, and the average amplitude of the λ = 400 μm peak, A_{400} resulted in a very similar relationship with σ_u as identified for $A_{800+400}$, but with slightly lower R^2 values of 0.909 and 0.893.

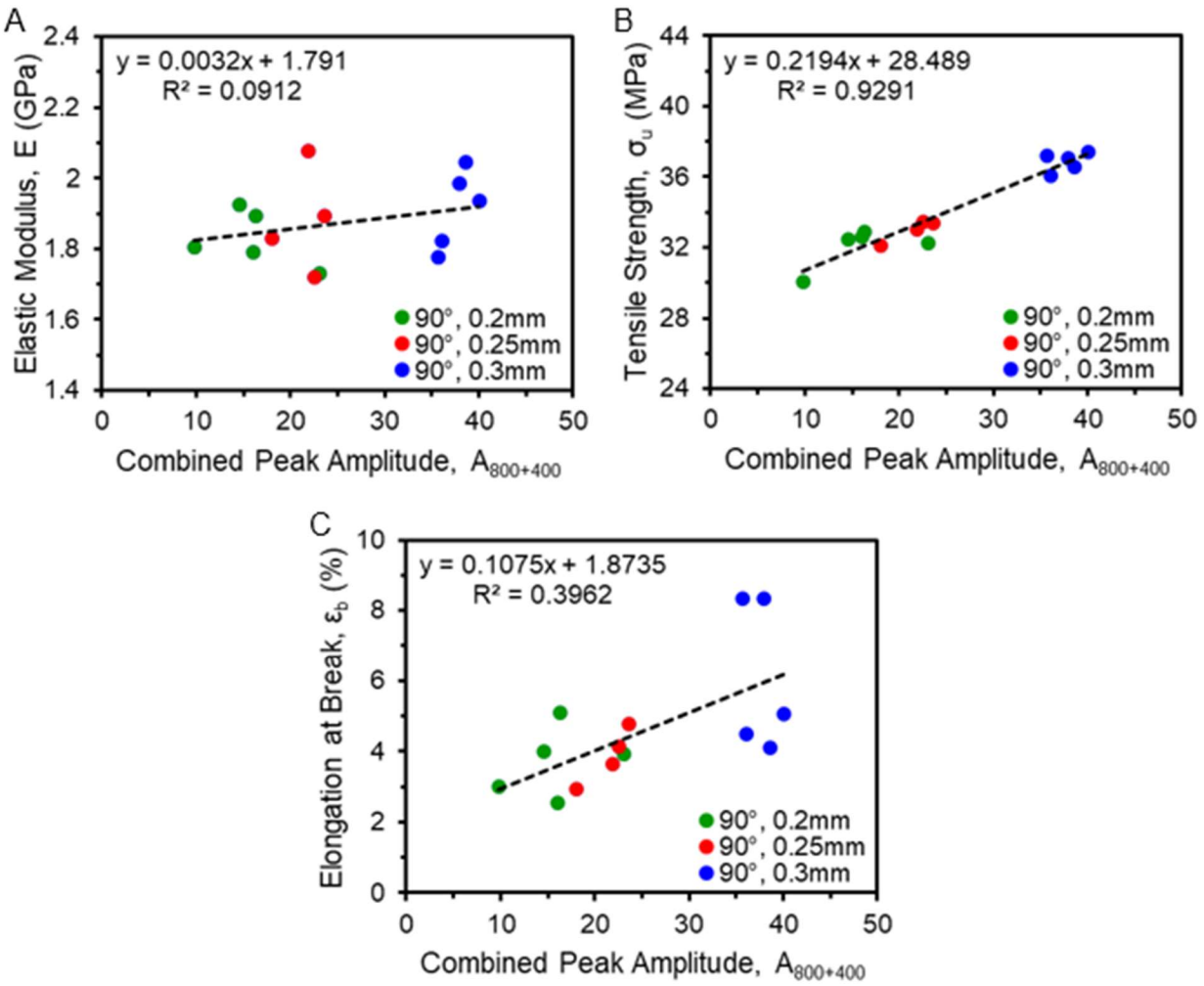

Figure 4.17: Correlations of the average combined peak amplitude, $A_{800+400}$, with the (A) elastic modulus; (B) ultimate tensile strength; (C) and elongation at break of all the tested 90° specimens.

The peak amplitude ratio, A_{800}/A_{400}, was selected to serve as a measure of the relative contributions to the surface morphology by the $\lambda = 400$ μm waves observed far from edges of the specimen like in the center of the grip sections and by the $\lambda = 800$ μm waves caused by the extrusion nozzle turning around at the edges of the specimen. Correlations of A_{800}/A_{400} with the measured mechanical properties results in no significant trends as shown in Figure 4.18. All three correlations have $R^2 < 0.05$.

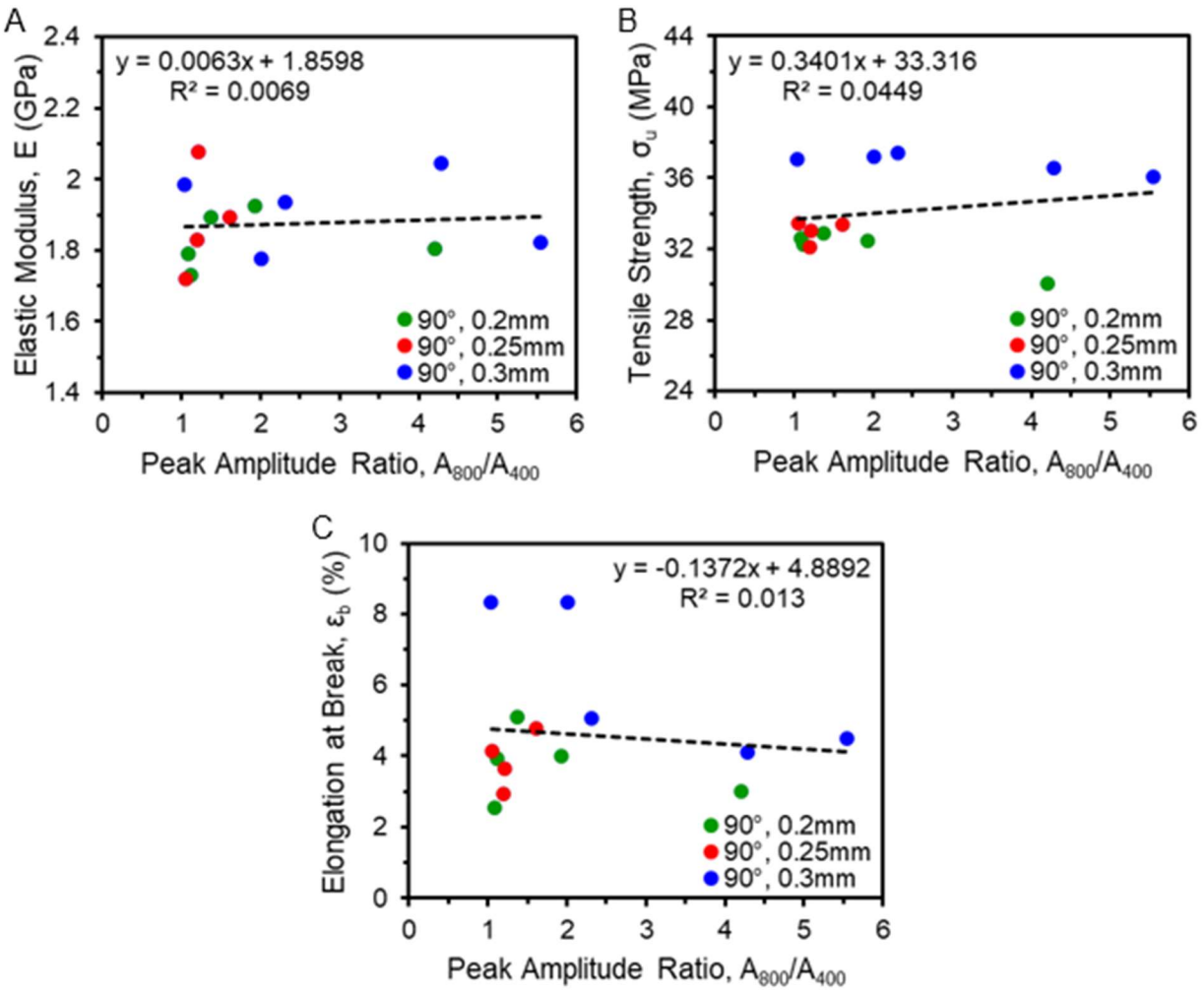

Figure 4.18: Correlations of the average peak amplitude ratio, A_{800}/A_{400}, with the (A) elastic modulus; (B) ultimate tensile strength; (C) and elongation at break of all the tested 90° specimens.

The background noise amplitude, A_{Noise}, was studied since surface defects including the stringing of material and holes in the top layer of the surface produced noise in the optical profilometry measurements which was carried through the FFTs into the SSASs. Despite this, Figure 4.19 shows that there are no significant linear trends present when the A_{Noise} is plotted against each of the measured mechanical properties.

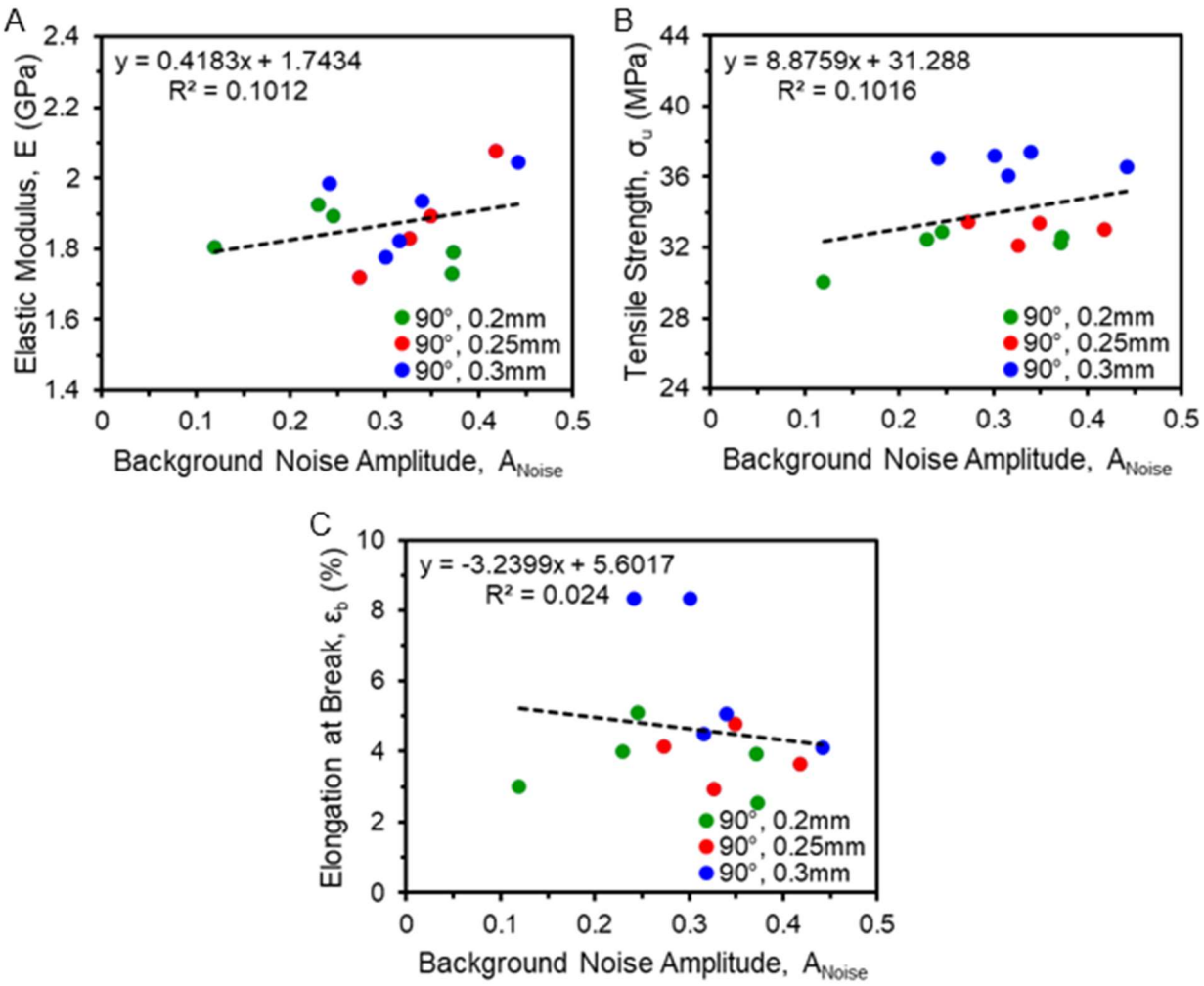

Figure 4.19: Correlations of the average background noise amplitude, A_{Noise}, with the (A) elastic modulus; (B) ultimate tensile strength; (C) and elongation at break of all the tested 90° specimens.

The MAD_{λ} is a measure of the variance of the amplitude of a given wavelength present in the specimen surface. High MAD_{λ} values indicate that the amplitude of the peak deviates significantly from the mean across the y-dimension of the surface, as would occur in a surface where the fundamental wave responsible for the surface morphology changes as occurs for 90°, 0.3mm, #4 in Figure 4.9. Figure 4.20 and Figure 4.21 plot MAD_{800} and MAD_{400} against each of the measured mechanical properties to identify correlations of either of these values with material performance. The plot of MAD_{800} and σ_u resulted in a good correlation with $R^2 = 0.785$

and a positive relationship between the MAD_{800} and σ_u. This suggests that the presence of the λ = 800 µm wave near the edges of the specimen is important to maintaining strength but that the amplitude of this wave should deviate (usually by decreasing) towards the middle of the surface for the best tensile strength. The same correlation with MAD_{400} was weaker with $R^2 = 0.327$. Plots of either value of MAD_λ against E or ε_b failed to produce any significant correlations.

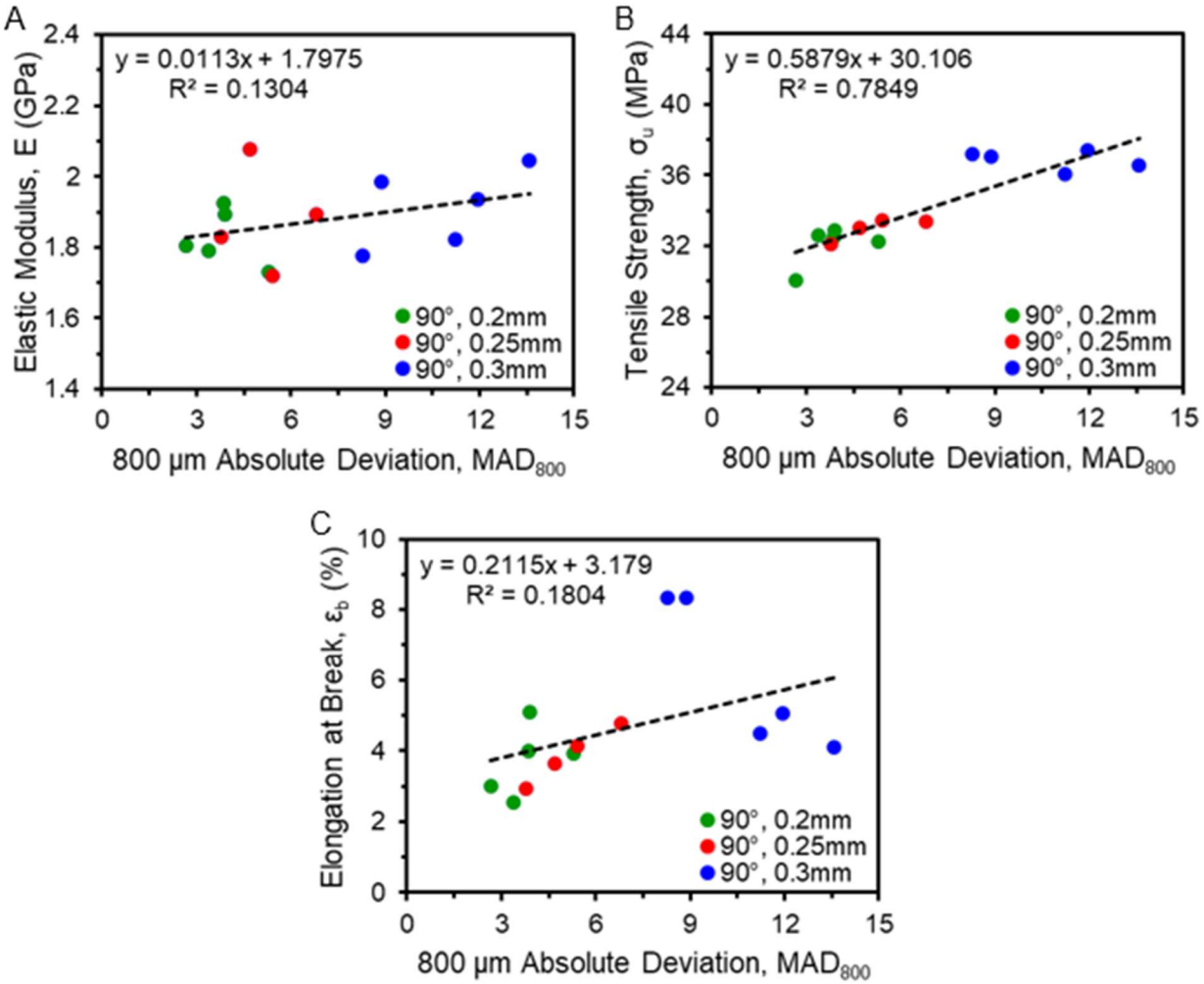

Figure 4.20: Correlations of the 800 µm mean absolute deviation, MAD_{800}, with the (A) elastic modulus; (B) ultimate tensile strength; (C) and elongation at break of all the tested 90° specimens.

The final pair of parameters, THD_{800} and THD_{400}, aim to measure how far the surface of each specimen is from a sinusoidal wave. This is done by finding the ratio of the combined

amplitudes of all the harmonics to the amplitude of the fundamental frequency. For THD_{800}, the amplitudes of the harmonics of an 800 µm wave (400, 266, 200, 160, 133, 114, 100 µm, etc.) were compared to the amplitude of the λ = 800 µm peak. Doing so and plotting against each of the studied mechanical properties as done in Figure 4.22 results in no significant correlations besides a weak correlation with σ_u and an $R^2 = 0.257$.

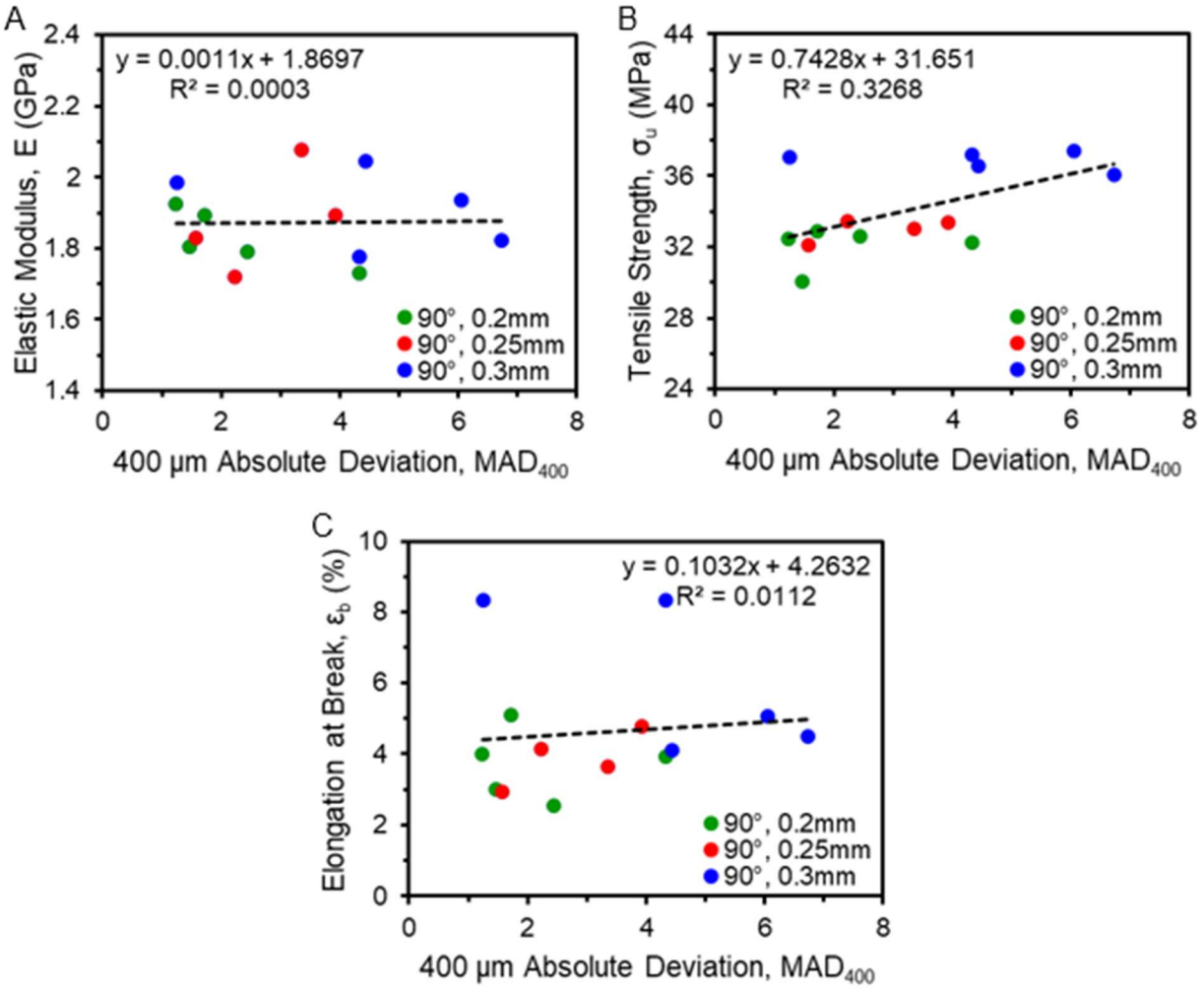

Figure 4.21: Correlations of the 400 µm mean absolute deviation, MAD_{400}, with the (A) elastic modulus; (B) ultimate tensile strength; (C) and elongation at break of all the tested 90° specimens.

Repeating the process for THD_{400}, instead using the harmonics of a 400 µm wave (200, 133, 100, 80, 66 µm, etc.), results in an improved correlation with σ_u as shown in Figure 4.23.

THD_{400} sorted the 0.3 mm layer height specimens into a cluster separated from the other two layer heights and correlated moderately well with σ_u with $R^2 = 0.604$. The shared harmonics of the two fundamental waves are thought to result in inaccurate THD values for some specimens, decreasing the significance of these correlations.

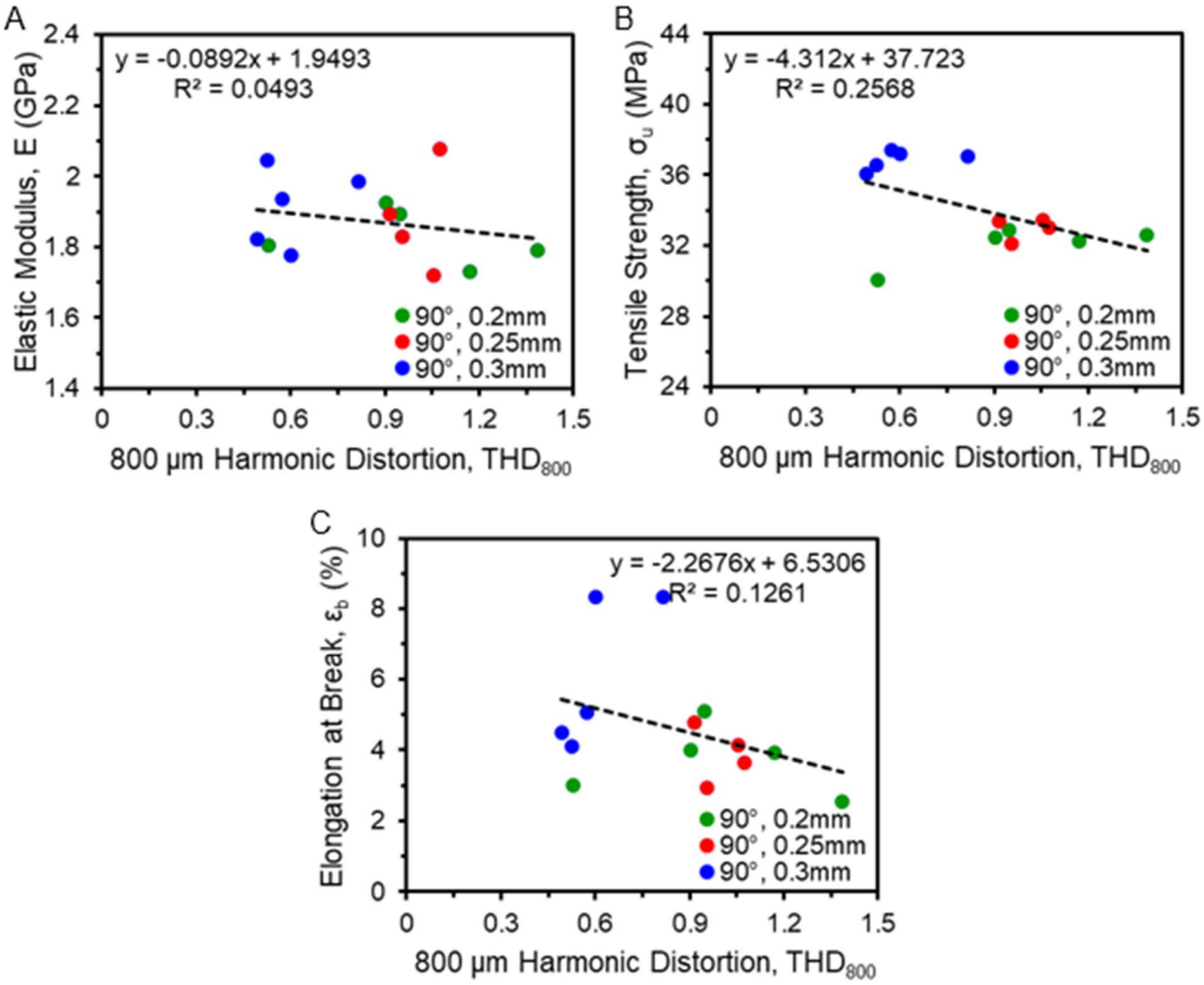

Figure 4.22: Correlations of the 800 µm total harmonic distortion, THD_{800}, with the (A) elastic modulus; (B) ultimate tensile strength; (C) and elongation at break of all the tested 90° specimens.

These same parameters were calculated for all the 0° specimens, but no strong correlations were identified due to the lack of observable periodicity along the x-dimension of

the specimen. The correlation plots for each of the seven parameters applied to the 0° specimens are provided in Figure A.3.

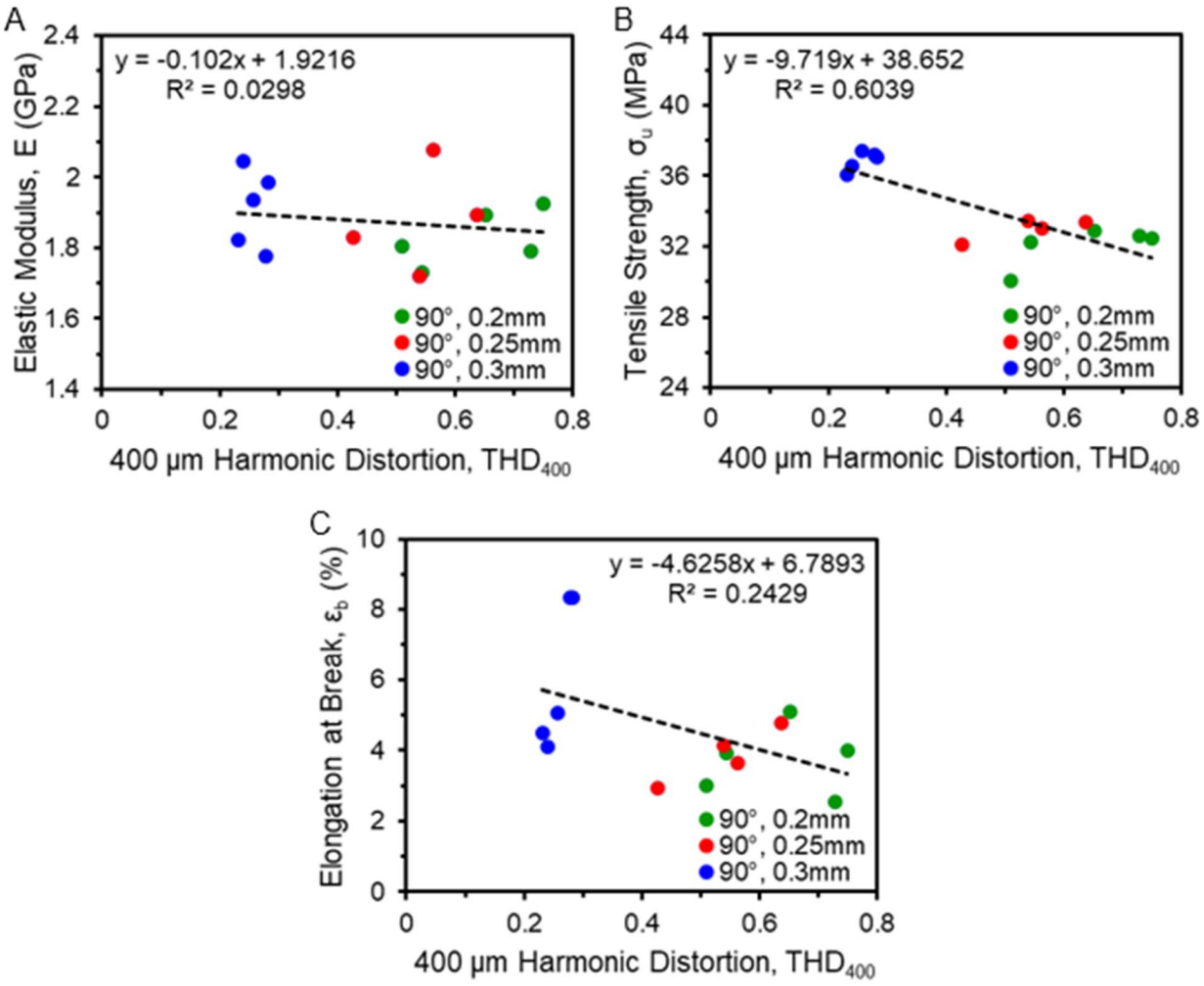

Figure 4.23: Correlations of the 400 µm total harmonic distortion, THD_{400}, with the (A) elastic modulus; (B) ultimate tensile strength; (C) and elongation at break of all the tested 90° specimens.

Chapter 5

Conclusions and Future Work

Acrylonitrile butadiene styrene Type V tensile specimens were additively manufactured by material extrusion with raster angles of 0° and 90° and layer heights of 0.2 mm, 0.25 mm, and 0.3 mm. A 3D surface morphology measurement of the narrow section of each specimen was obtained via focus variation microscopy. Significant differences in surface morphology were identified, even between specimens printed with identical process parameters at the same time. A series of fast Fourier transforms were applied to each surface to quantify these differences in surface morphology. These 1D Fourier transforms were aligned parallel to the tensile direction, outputting amplitude spectra of the waves that made up the surface. These spectra were analyzed to calculate parameters that characterized the height variation, noisiness, and how sinusoidal the surface morphology was, among other properties.

Uniaxial tensile testing did not provide statistically significant results on the effects of raster angle and layer height on the elastic modulus, ultimate tensile strength, and elongation at break. These properties were correlated with the parameters calculated from the amplitude spectra of each specimen's surface. No significant correlations were identified for the elastic modulus or elongation at break. The ultimate tensile strength of the 90° raster angle specimens was found to have a positive correlation with the combined amplitude of the 800 μm and 400 μm peaks ($R^2 = 0.929$), corresponding to the height variation of the surface. The tensile strength also had a positive correlation with the mean absolute deviation of the 800 μm peak across the width of the specimen ($R^2 = 0.785$) and a negative correlation with the total harmonic distortion of the surface ($R^2 = 0.604$), describing how sinusoidal the surface was. These correlations should

enable improved quality assurance of additively manufactured plastics without the need for destructive testing.

Future work is necessary to ensure the accuracy of the identified correlations and develop them into a predictive model of mechanical performance according to surface morphology measurements. Other process parameters in addition to raster angle and layer height will need to be considered to ensure robustness of the model. These parameters may include extrusion width, printing speed, and extrusion temperature.

Appendix

Supplementary Figures

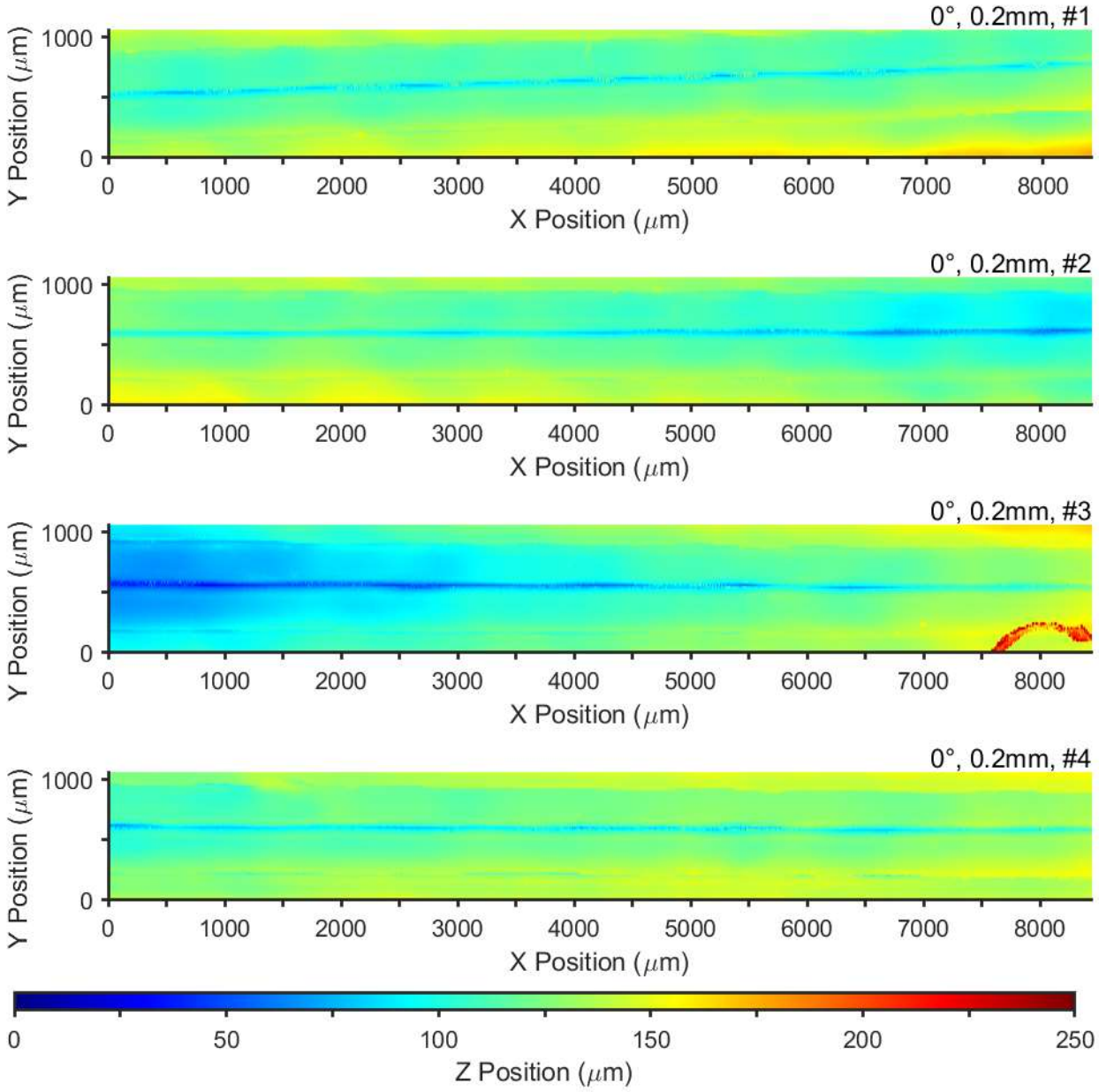

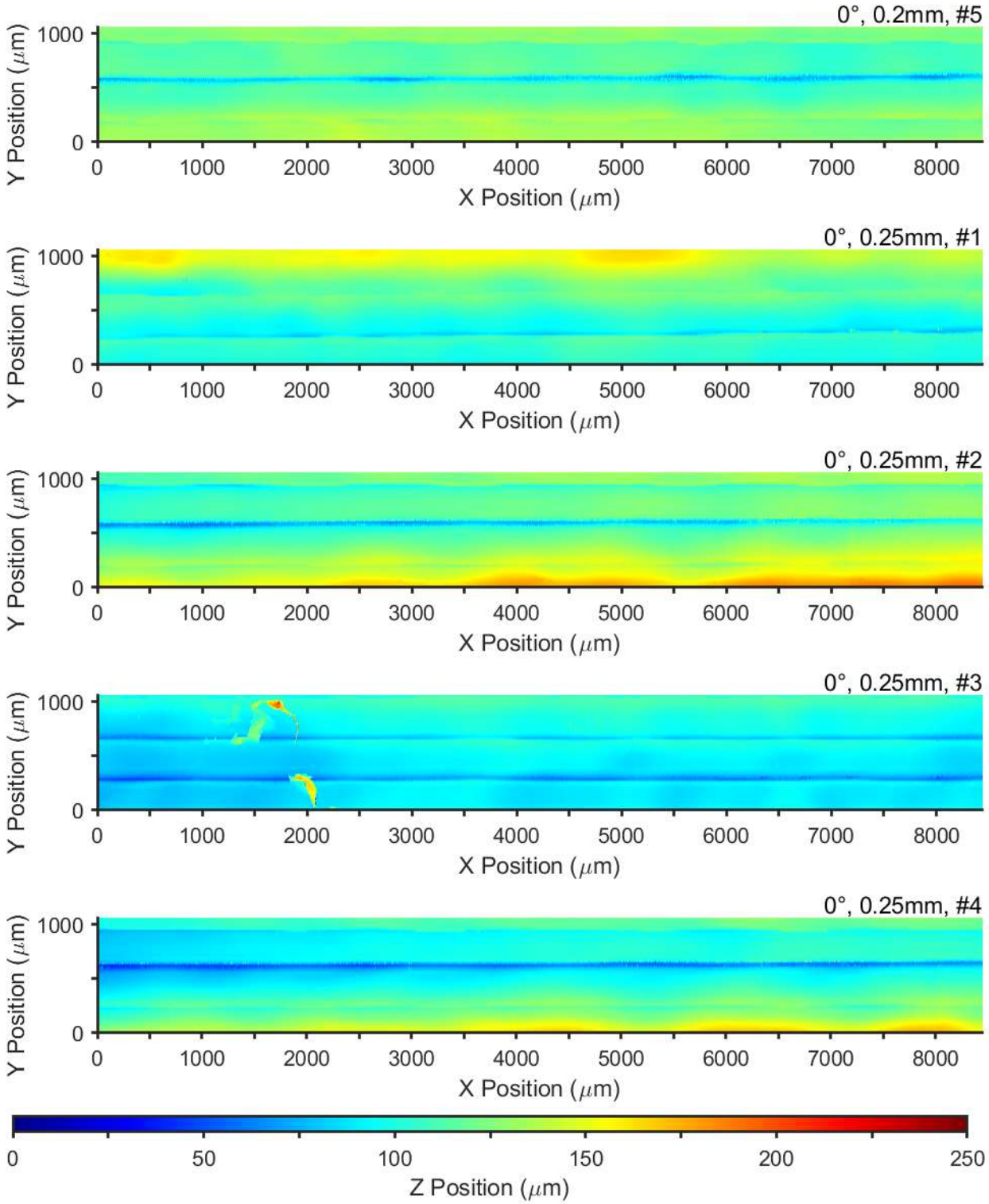
0°, 0.2mm, #5
0°, 0.25mm, #1
0°, 0.25mm, #2
0°, 0.25mm, #3
0°, 0.25mm, #4
Y Position (μm)
X Position (μm)
0
1000
2000
3000
4000
5000
6000
7000
8000
0
50
100
150
200
250
Z Position (μm)

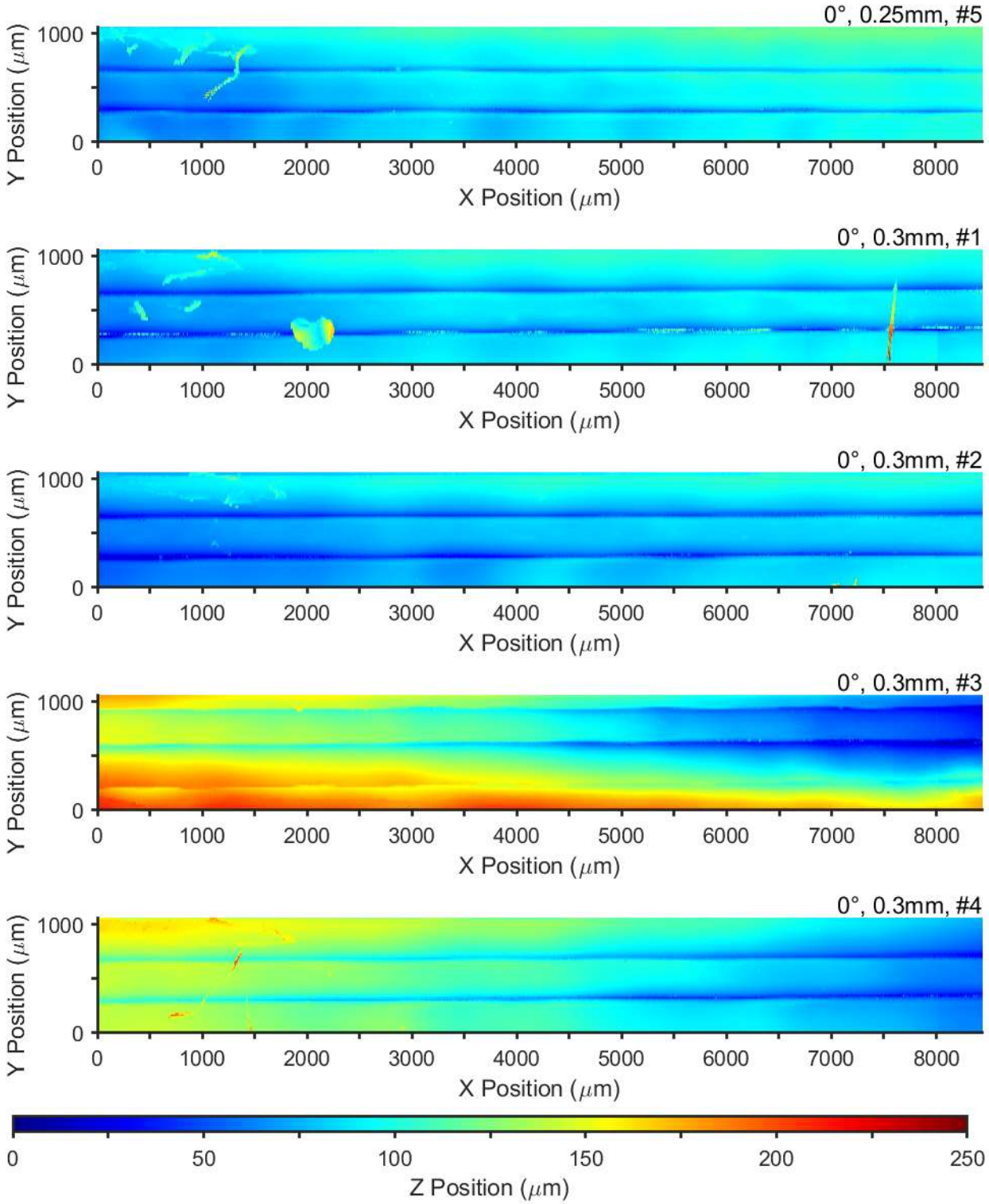
0°, 0.25mm, #5
0°, 0.3mm, #1
0°, 0.3mm, #2
0°, 0.3mm, #3
0°, 0.3mm, #4
Y Position (μm)
X Position (μm)
0
1000
2000
3000
4000
5000
6000
7000
8000
0
50
100
150
200
250
Z Position (μm)

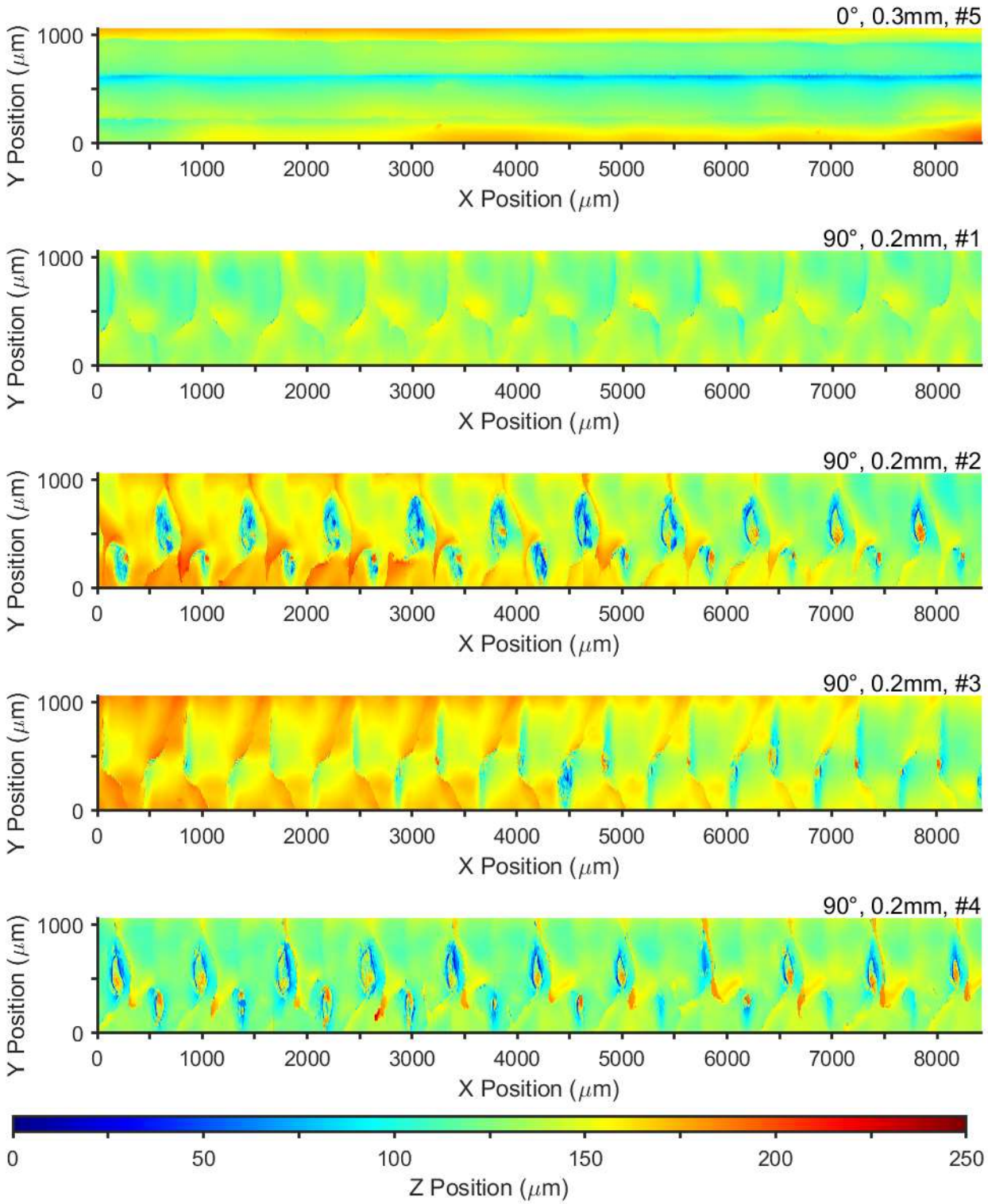
0°, 0.3mm, #5
90°, 0.2mm, #1
90°, 0.2mm, #2
90°, 0.2mm, #3
90°, 0.2mm, #4
Y Position (μm)
X Position (μm)
0
1000
2000
3000
4000
5000
6000
7000
8000
0
50
100
150
200
250
Z Position (μm)

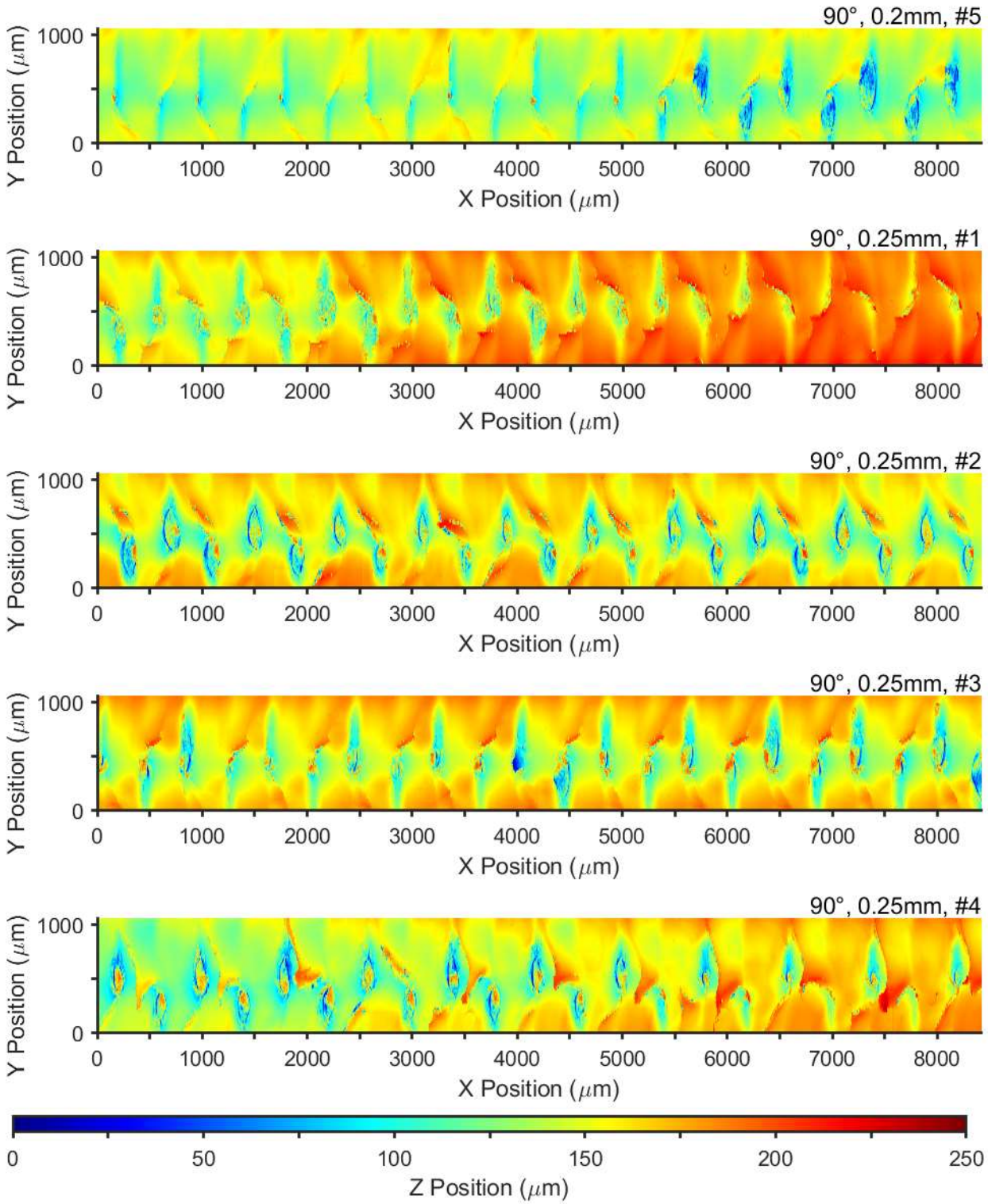
90°, 0.2mm, #5
90°, 0.25mm, #1
90°, 0.25mm, #2
90°, 0.25mm, #3
90°, 0.25mm, #4
Y Position (μm)
X Position (μm)
0
1000
2000
3000
4000
5000
6000
7000
8000
50
100
150
200
250
Z Position (μm)

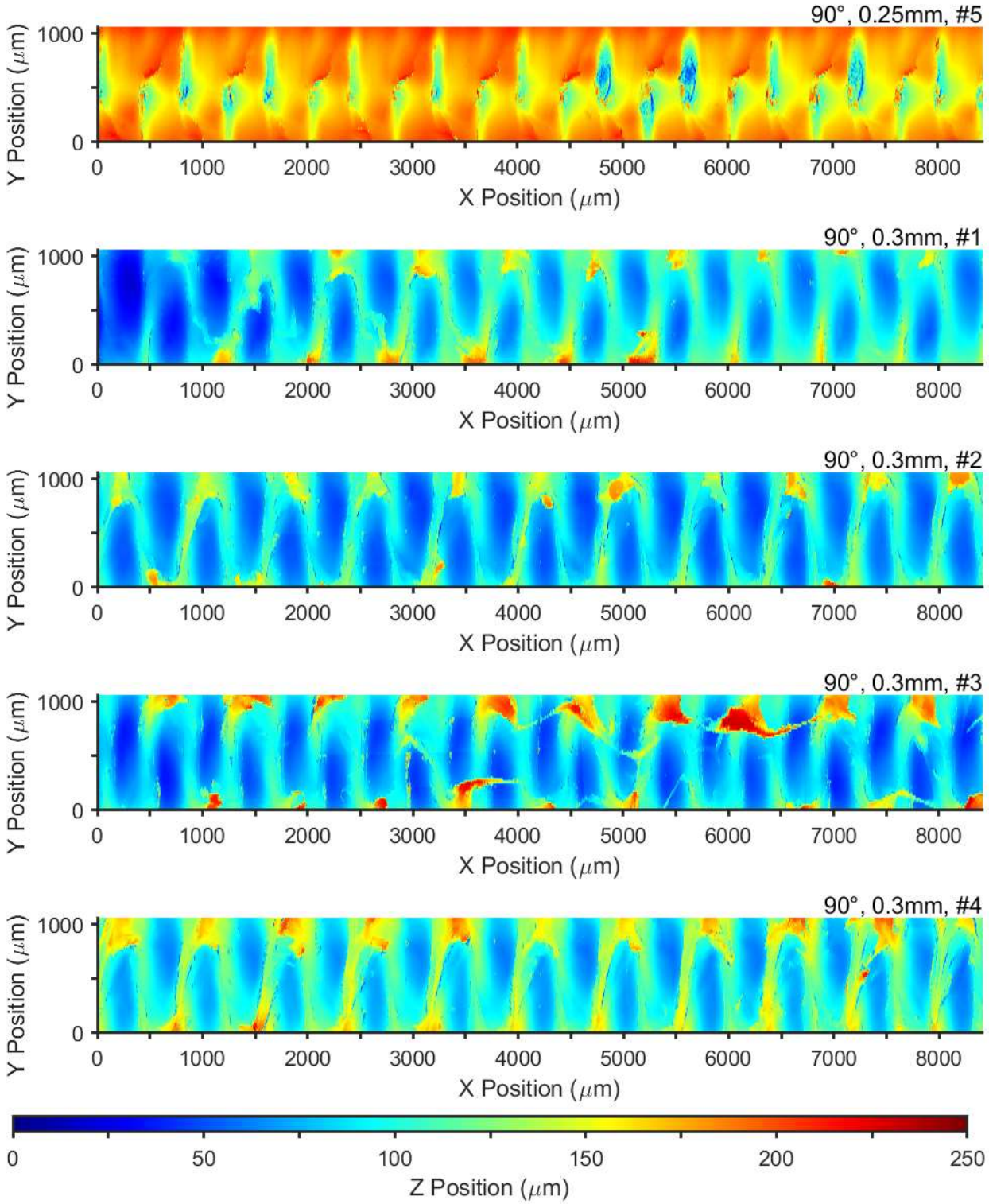
90°, 0.25mm, #5
90°, 0.3mm, #1
90°, 0.3mm, #2
90°, 0.3mm, #3
90°, 0.3mm, #4
Y Position (μm)
X Position (μm)
0
1000
2000
3000
4000
5000
6000
7000
8000
0
50
100
150
200
250
Z Position (μm)

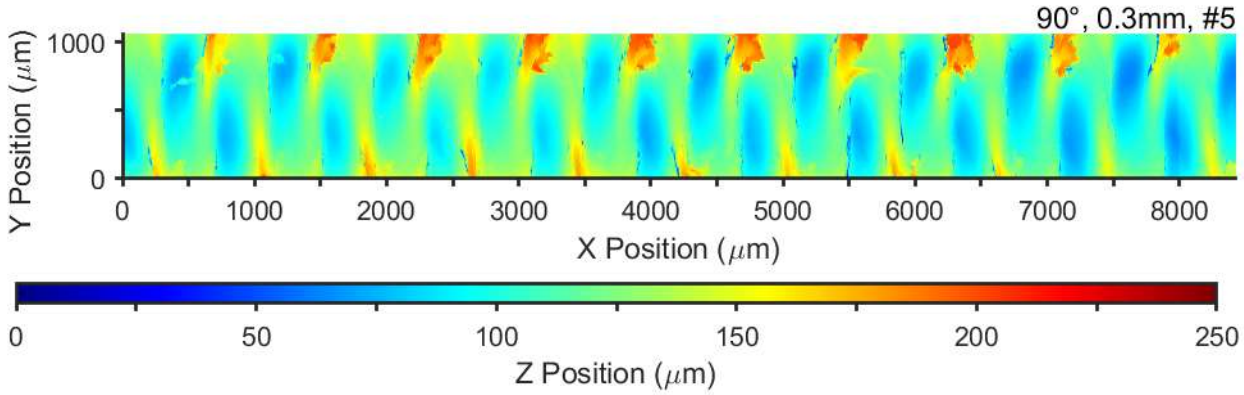

Figure A.1: 3D surface morphology measurements of the narrow sections of all thirty specimens with raster angles of 0° and 90° and layer heights of 0.2, 0.25, and 0.3 mm.

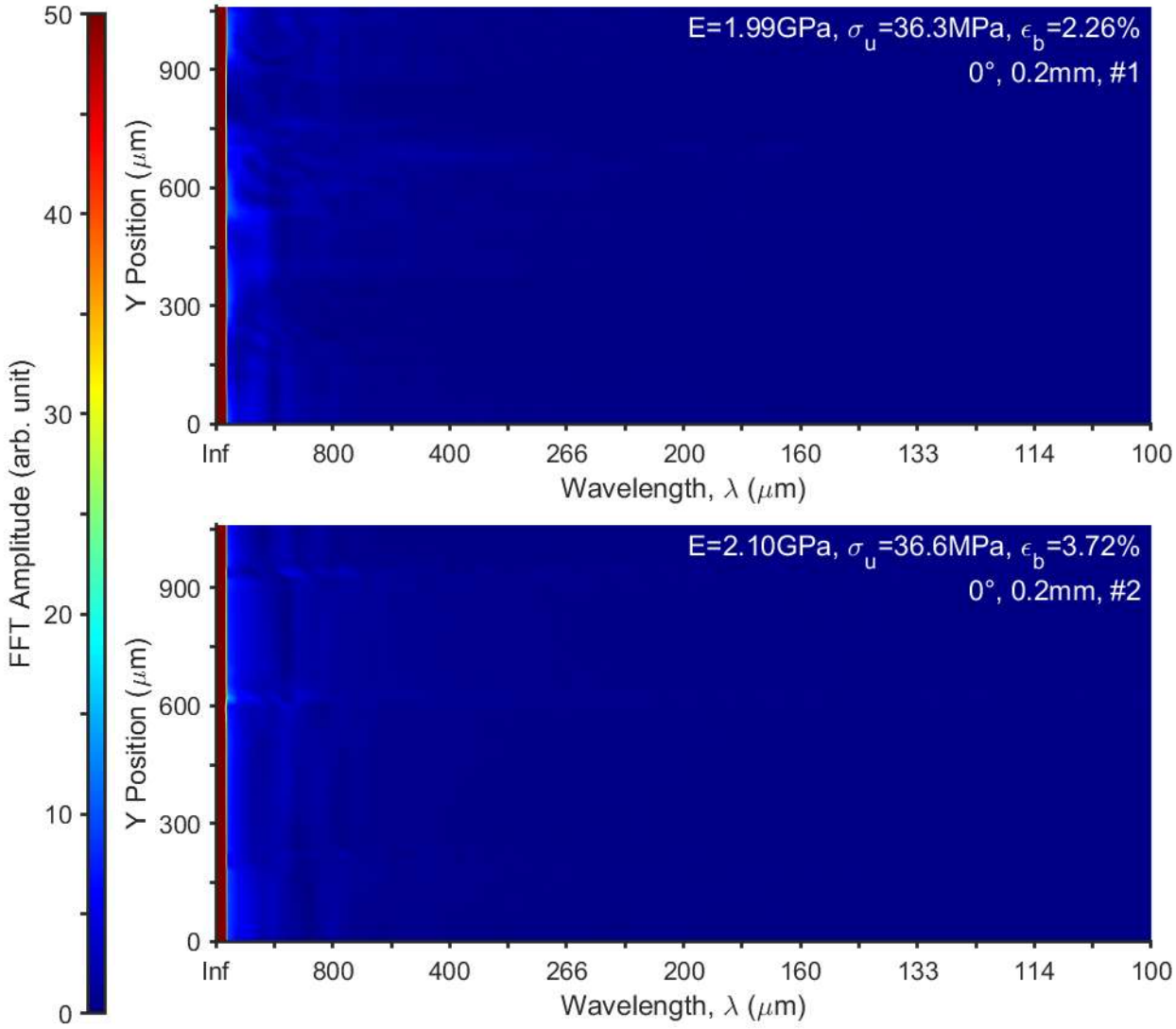

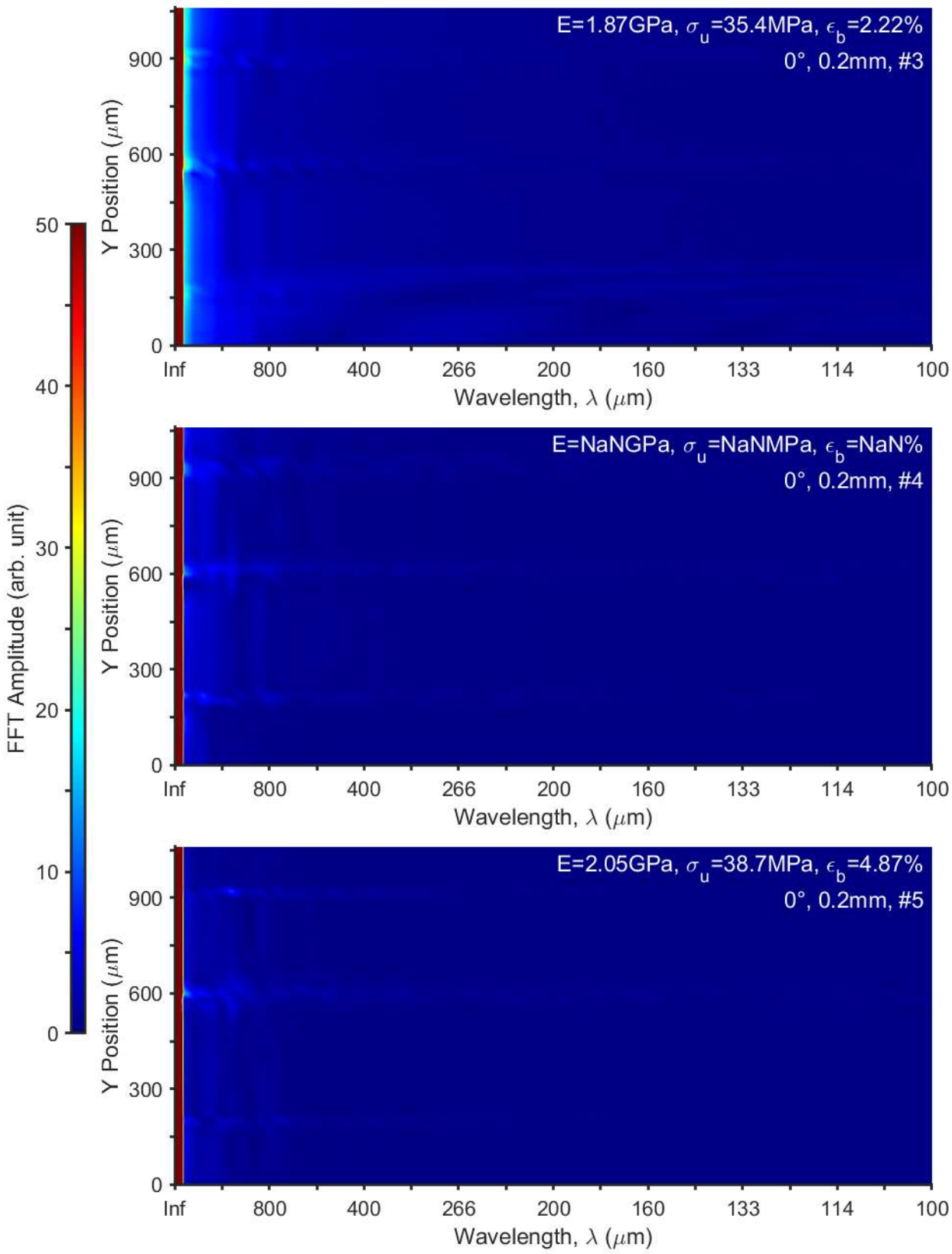
E=1.87GPa, σ_u=35.4MPa, ϵ_b=2.22%
0°, 0.2mm, #3
E=NaNGPa, σ_u=NaNMPa, ϵ_b=NaN%
0°, 0.2mm, #4
E=2.05GPa, σ_u=38.7MPa, ϵ_b=4.87%
0°, 0.2mm, #5
Y Position (μm)
0
300
600
900
Wavelength, λ (μm)
Inf
800
400
266
200
160
133
114
100
FFT Amplitude (arb. unit)
0
10
20
30
40
50

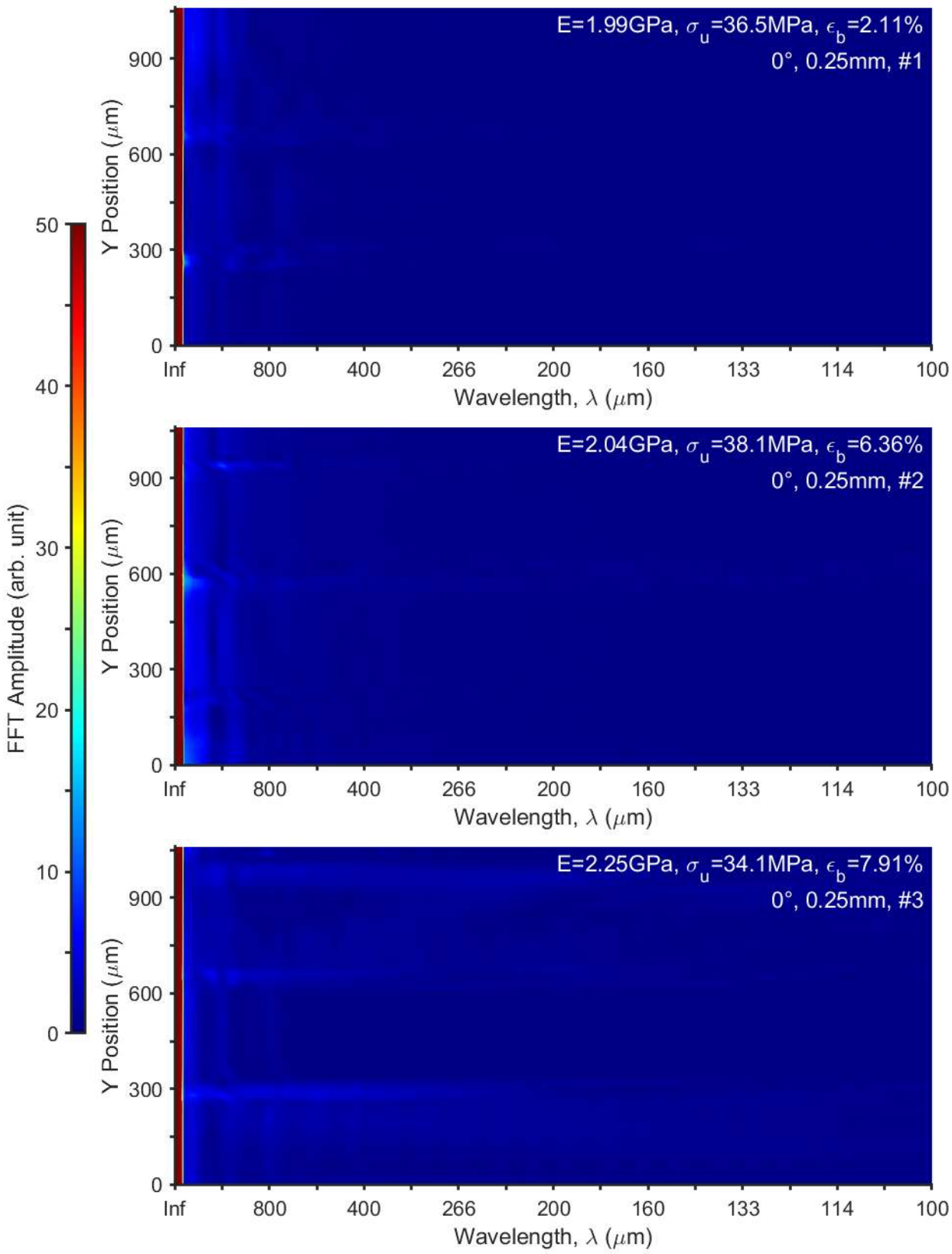
E=1.99GPa, σ_u=36.5MPa, ϵ_b=2.11%
0°, 0.25mm, #1
E=2.04GPa, σ_u=38.1MPa, ϵ_b=6.36%
0°, 0.25mm, #2
E=2.25GPa, σ_u=34.1MPa, ϵ_b=7.91%
0°, 0.25mm, #3
Y Position (μm)
0
300
600
900
Wavelength, λ (μm)
Inf
800
400
266
200
160
133
114
100
FFT Amplitude (arb. unit)
0
10
20
30
40
50

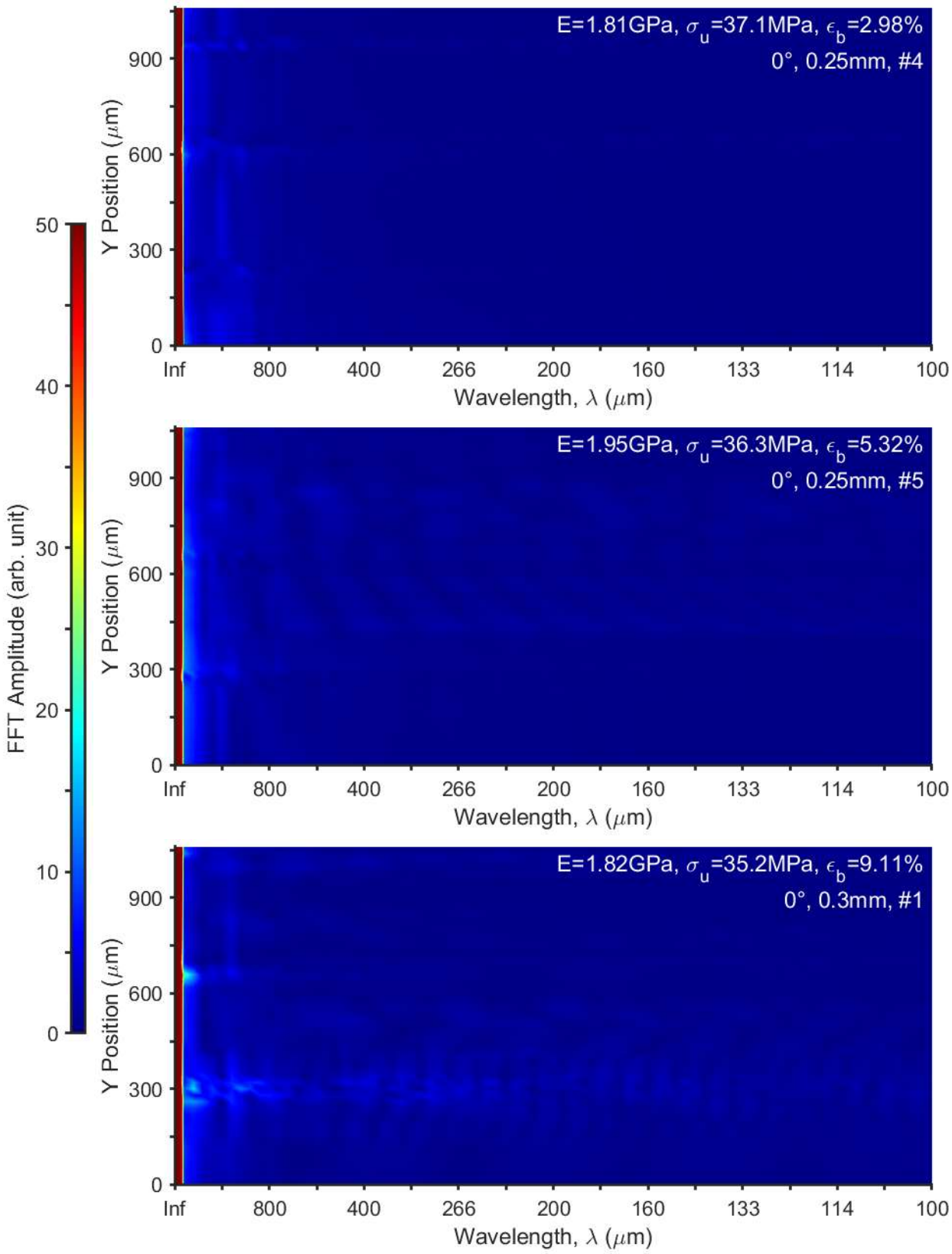
E=1.81GPa, σ_u=37.1MPa, ϵ_b=2.98%
0°, 0.25mm, #4
E=1.95GPa, σ_u=36.3MPa, ϵ_b=5.32%
0°, 0.25mm, #5
E=1.82GPa, σ_u=35.2MPa, ϵ_b=9.11%
0°, 0.3mm, #1
Y Position (μm)
0
300
600
900
Wavelength, λ (μm)
Inf
800
400
266
200
160
133
114
100
FFT Amplitude (arb. unit)
0
10
20
30
40
50

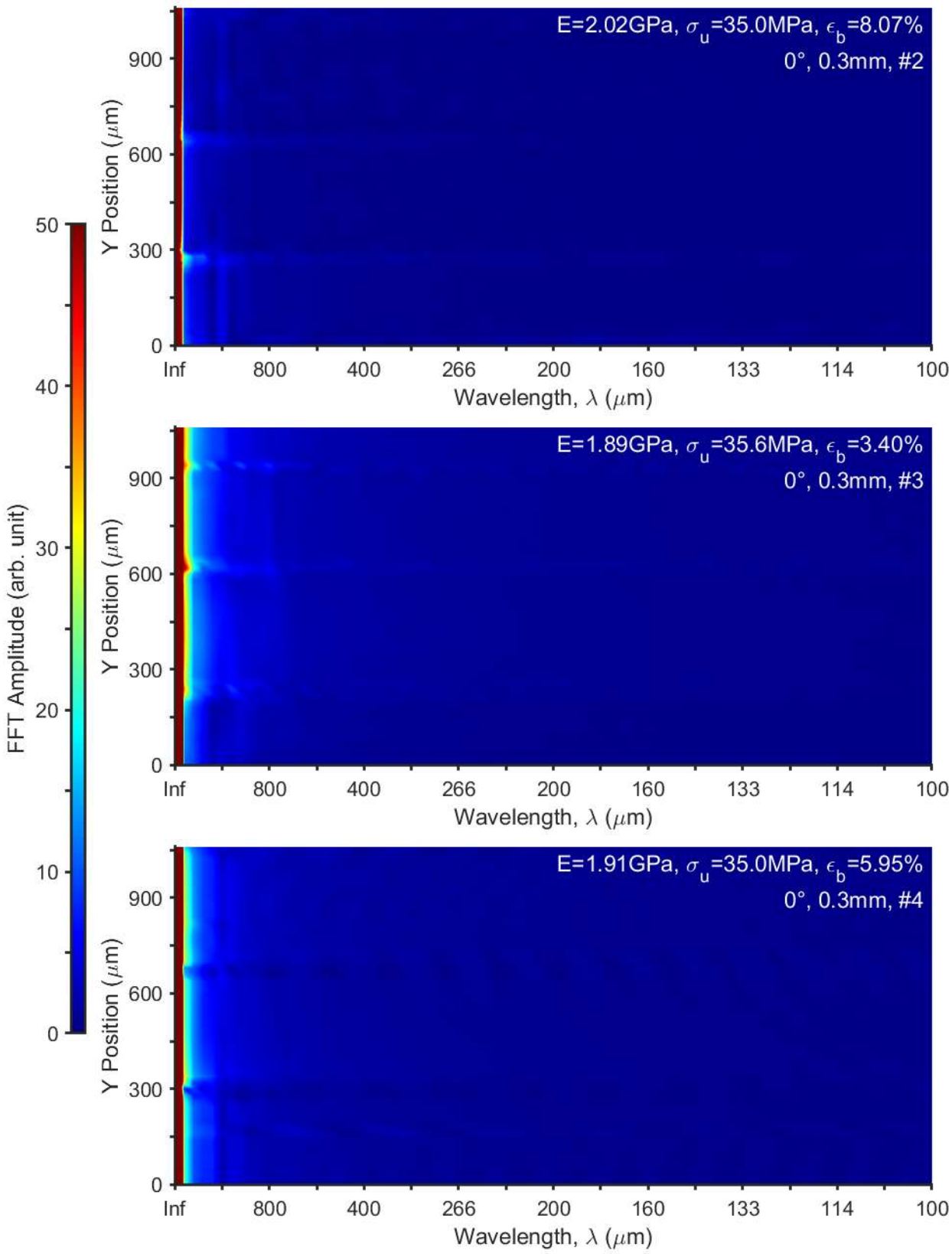
E=2.02GPa, σ_u=35.0MPa, ϵ_b=8.07%
0°, 0.3mm, #2
E=1.89GPa, σ_u=35.6MPa, ϵ_b=3.40%
0°, 0.3mm, #3
E=1.91GPa, σ_u=35.0MPa, ϵ_b=5.95%
0°, 0.3mm, #4
Y Position (μm)
0
300
600
900
Wavelength, λ (μm)
Inf
800
400
266
200
160
133
114
100
FFT Amplitude (arb. unit)
0
10
20
30
40
50

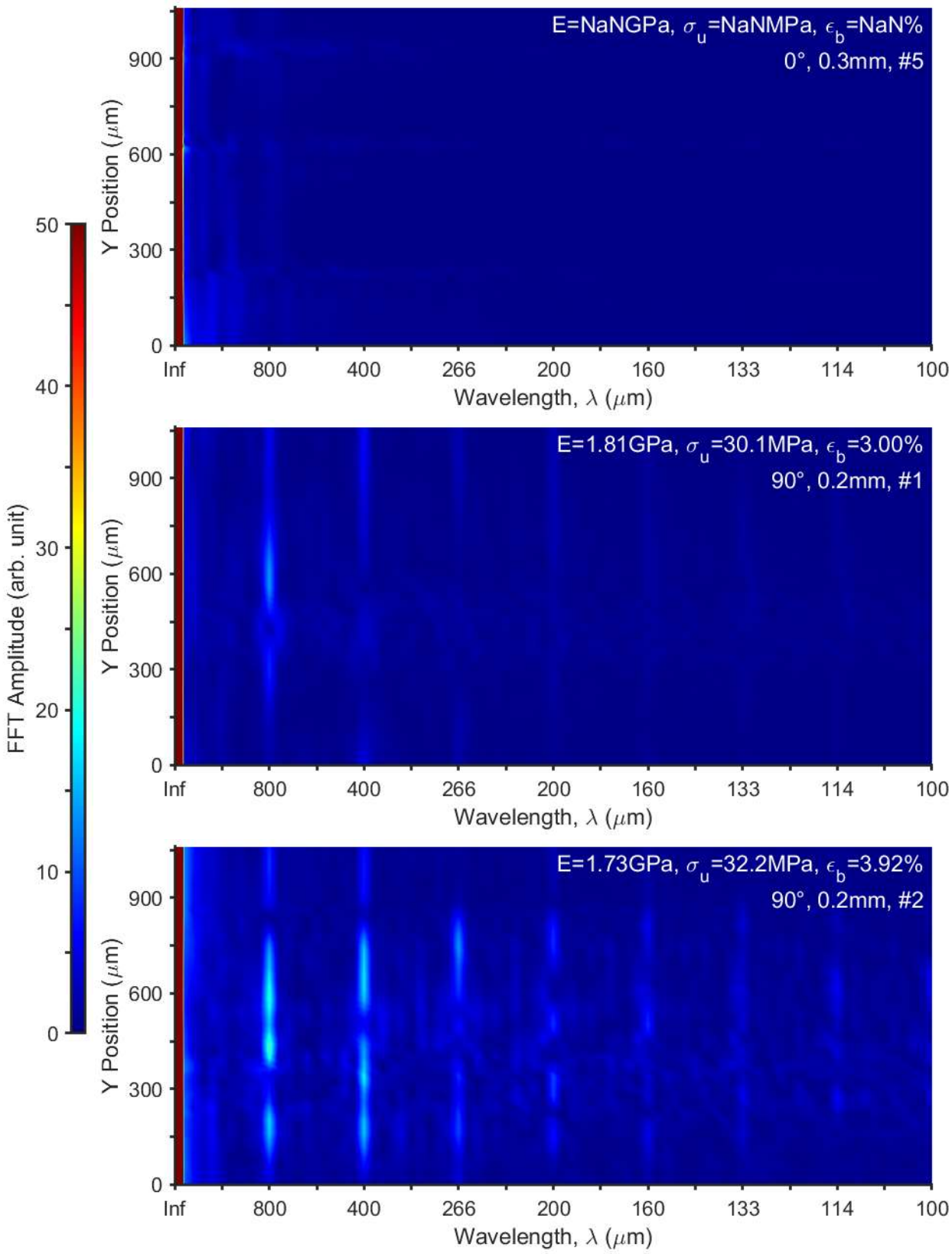
E=NaNGPa, σ_u=NaNMPa, ϵ_b=NaN%
0°, 0.3mm, #5
E=1.81GPa, σ_u=30.1MPa, ϵ_b=3.00%
90°, 0.2mm, #1
E=1.73GPa, σ_u=32.2MPa, ϵ_b=3.92%
90°, 0.2mm, #2
Y Position (μm)
0
300
600
900
Wavelength, λ (μm)
Inf
800
400
266
200
160
133
114
100
FFT Amplitude (arb. unit)
0
10
20
30
40
50

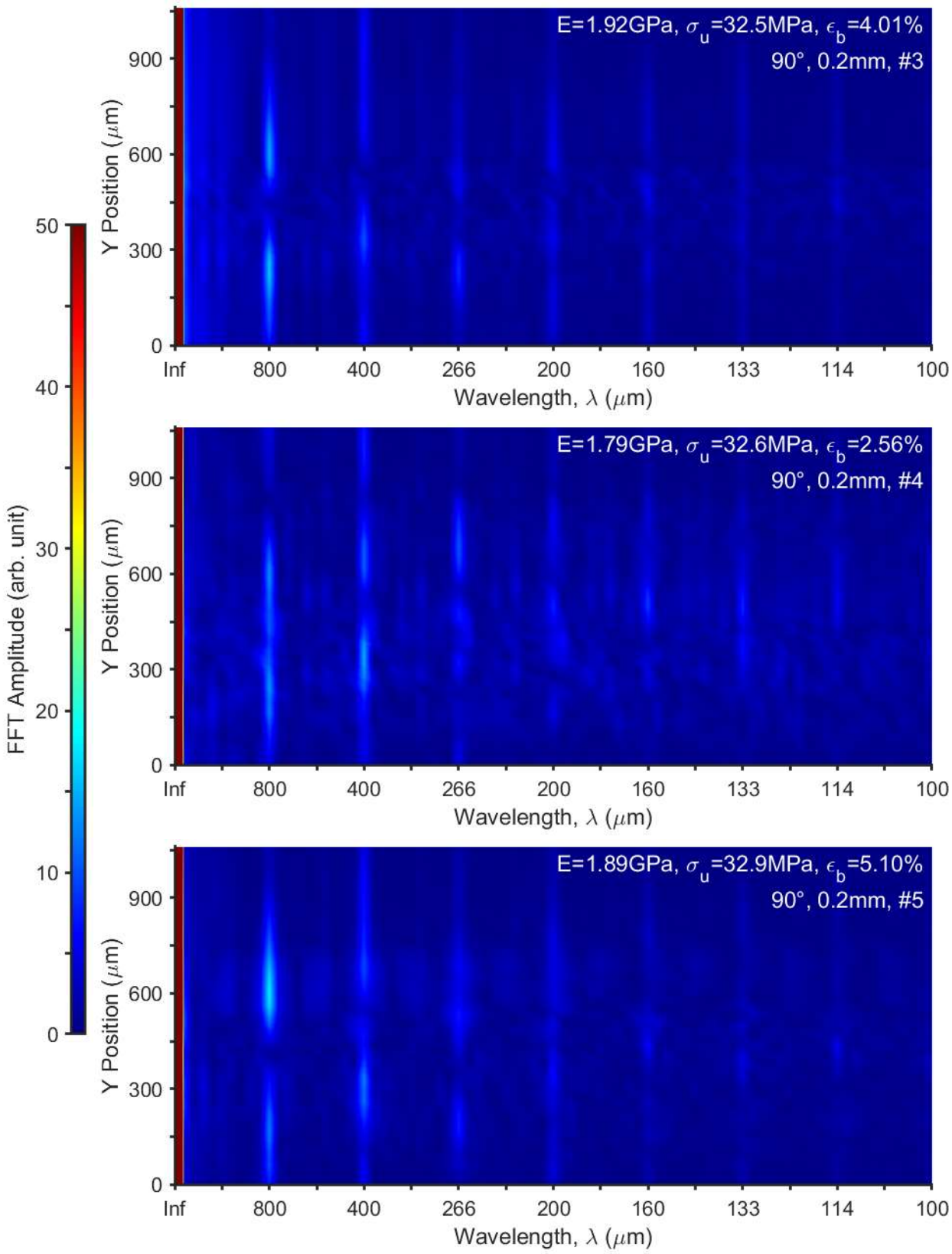
E=1.92GPa, σ_u=32.5MPa, ϵ_b=4.01%
90°, 0.2mm, #3
E=1.79GPa, σ_u=32.6MPa, ϵ_b=2.56%
90°, 0.2mm, #4
E=1.89GPa, σ_u=32.9MPa, ϵ_b=5.10%
90°, 0.2mm, #5
Y Position (μm)
0
300
600
900
Wavelength, λ (μm)
Inf
800
400
266
200
160
133
114
100
FFT Amplitude (arb. unit)
0
10
20
30
40
50

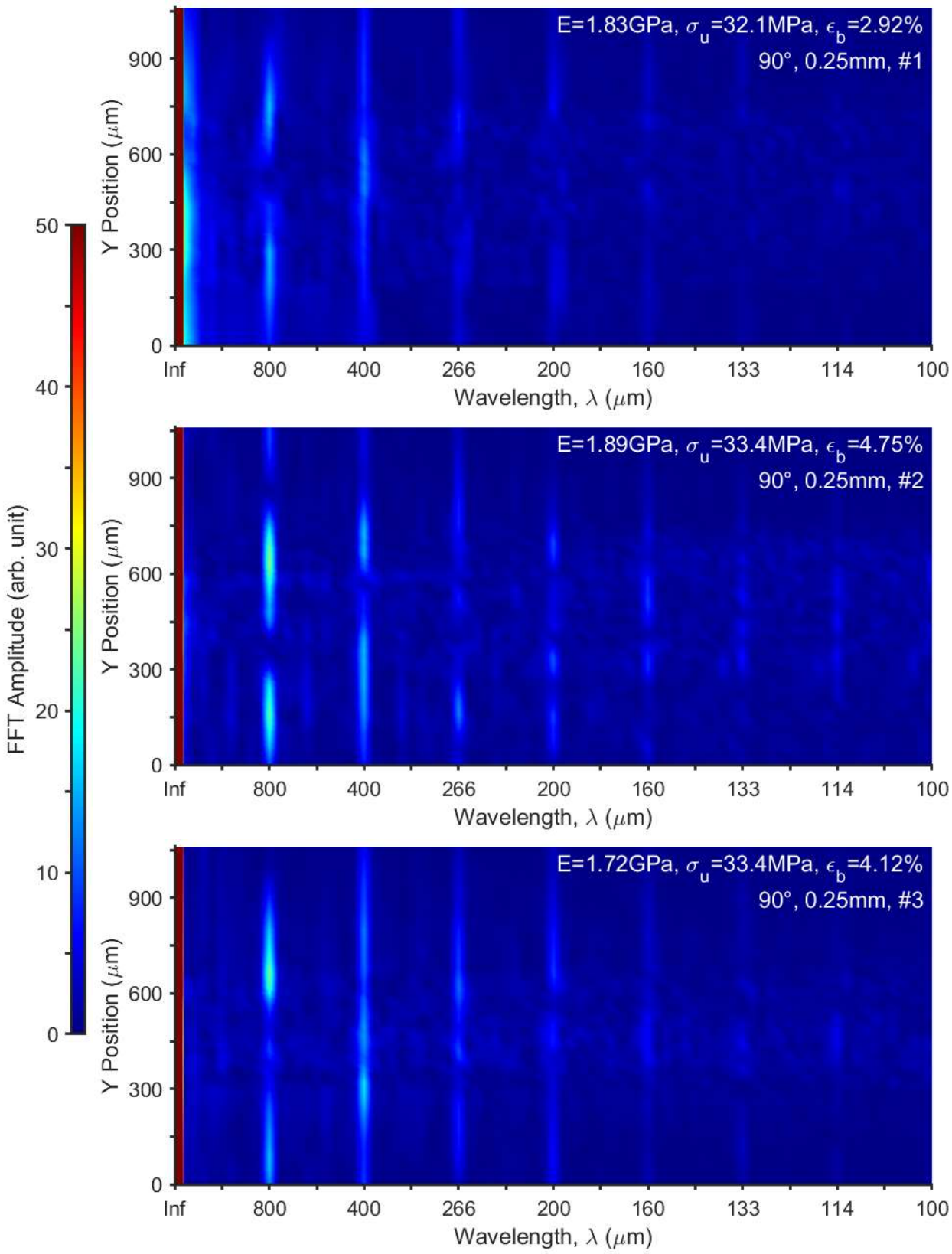
E=1.83GPa, σ_u=32.1MPa, ϵ_b=2.92%
90°, 0.25mm, #1
E=1.89GPa, σ_u=33.4MPa, ϵ_b=4.75%
90°, 0.25mm, #2
E=1.72GPa, σ_u=33.4MPa, ϵ_b=4.12%
90°, 0.25mm, #3
Y Position (μm)
0
300
600
900
Wavelength, λ (μm)
Inf
800
400
266
200
160
133
114
100
FFT Amplitude (arb. unit)
0
10
20
30
40
50

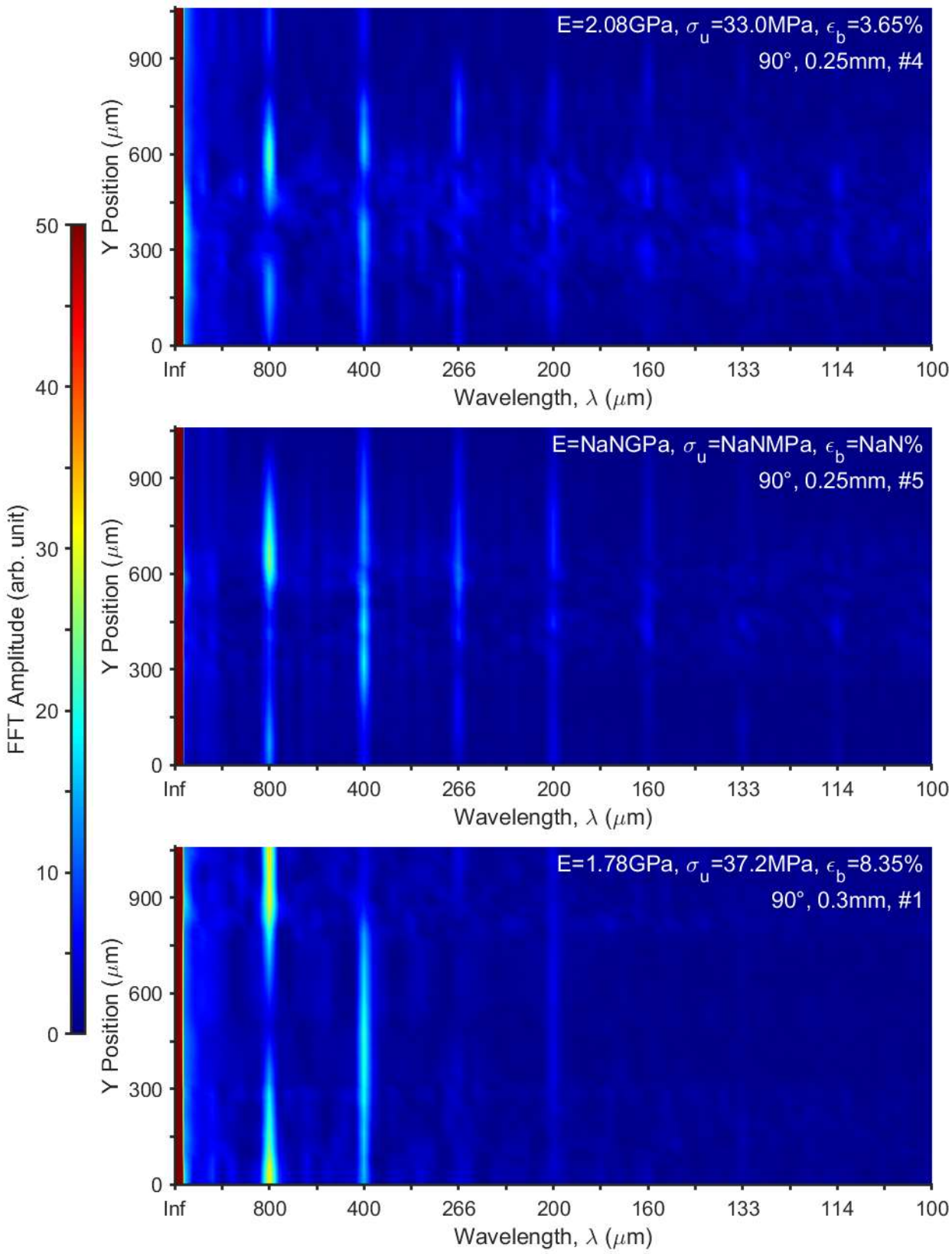
E=2.08GPa, σ_u=33.0MPa, ϵ_b=3.65%
90°, 0.25mm, #4
E=NaNGPa, σ_u=NaNMPa, ϵ_b=NaN%
90°, 0.25mm, #5
E=1.78GPa, σ_u=37.2MPa, ϵ_b=8.35%
90°, 0.3mm, #1
Y Position (μm)
0
300
600
900
Wavelength, λ (μm)
Inf
800
400
266
200
160
133
114
100
FFT Amplitude (arb. unit)
0
10
20
30
40
50

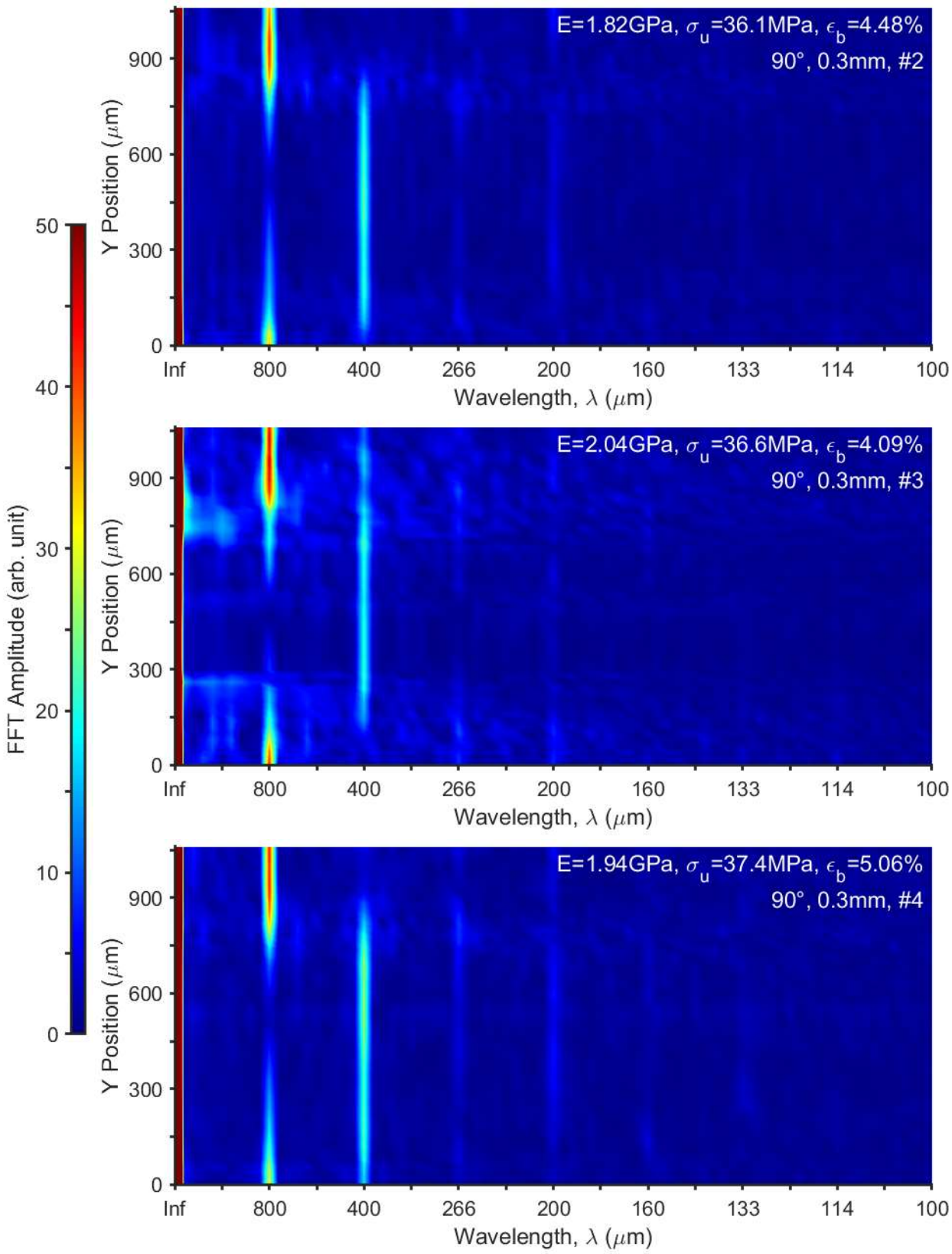
E=1.82GPa, σ_u=36.1MPa, ϵ_b=4.48%
90°, 0.3mm, #2
E=2.04GPa, σ_u=36.6MPa, ϵ_b=4.09%
90°, 0.3mm, #3
E=1.94GPa, σ_u=37.4MPa, ϵ_b=5.06%
90°, 0.3mm, #4
Y Position (μm)
0
300
600
900
Wavelength, λ (μm)
Inf
800
400
266
200
160
133
114
100
FFT Amplitude (arb. unit)
0
10
20
30
40
50

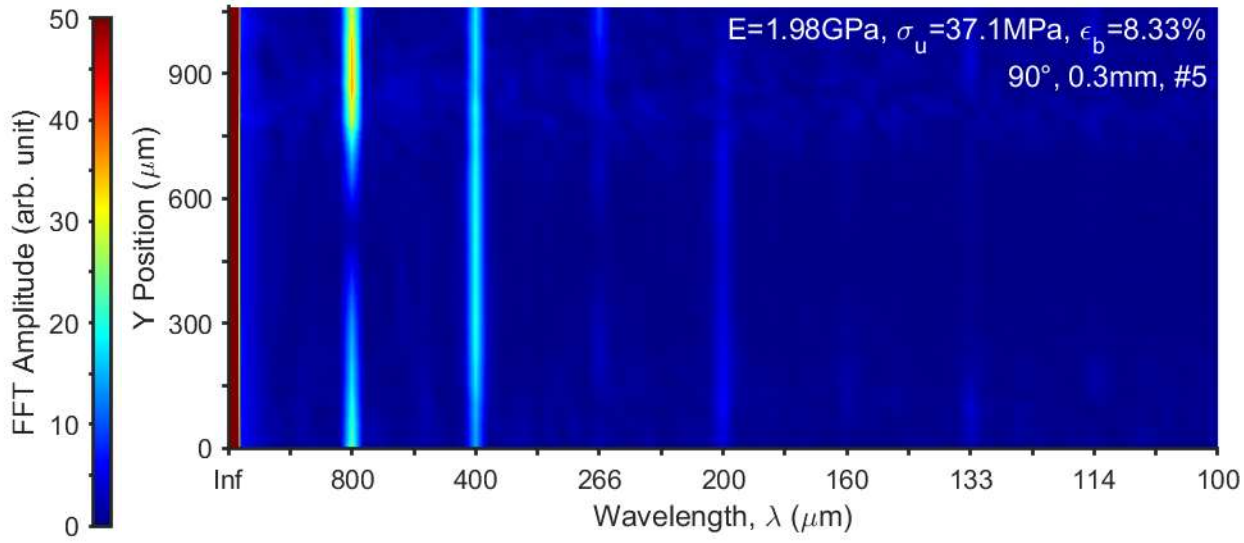

Figure A.2: Single-sided amplitude spectra of the narrow sections of all thirty specimens with raster angles of 0° and 90° and layer heights of 0.2, 0.25, and 0.3 mm.

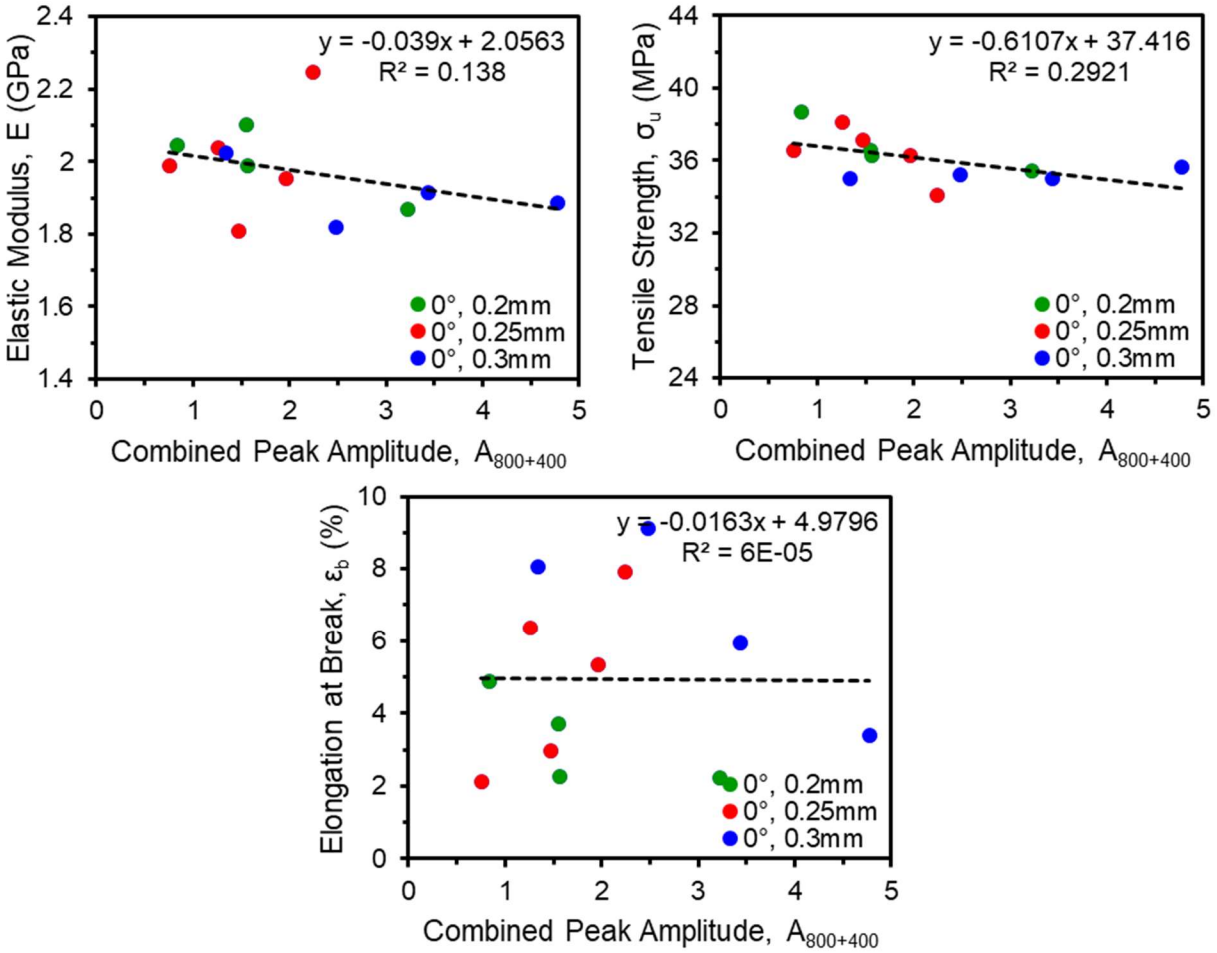

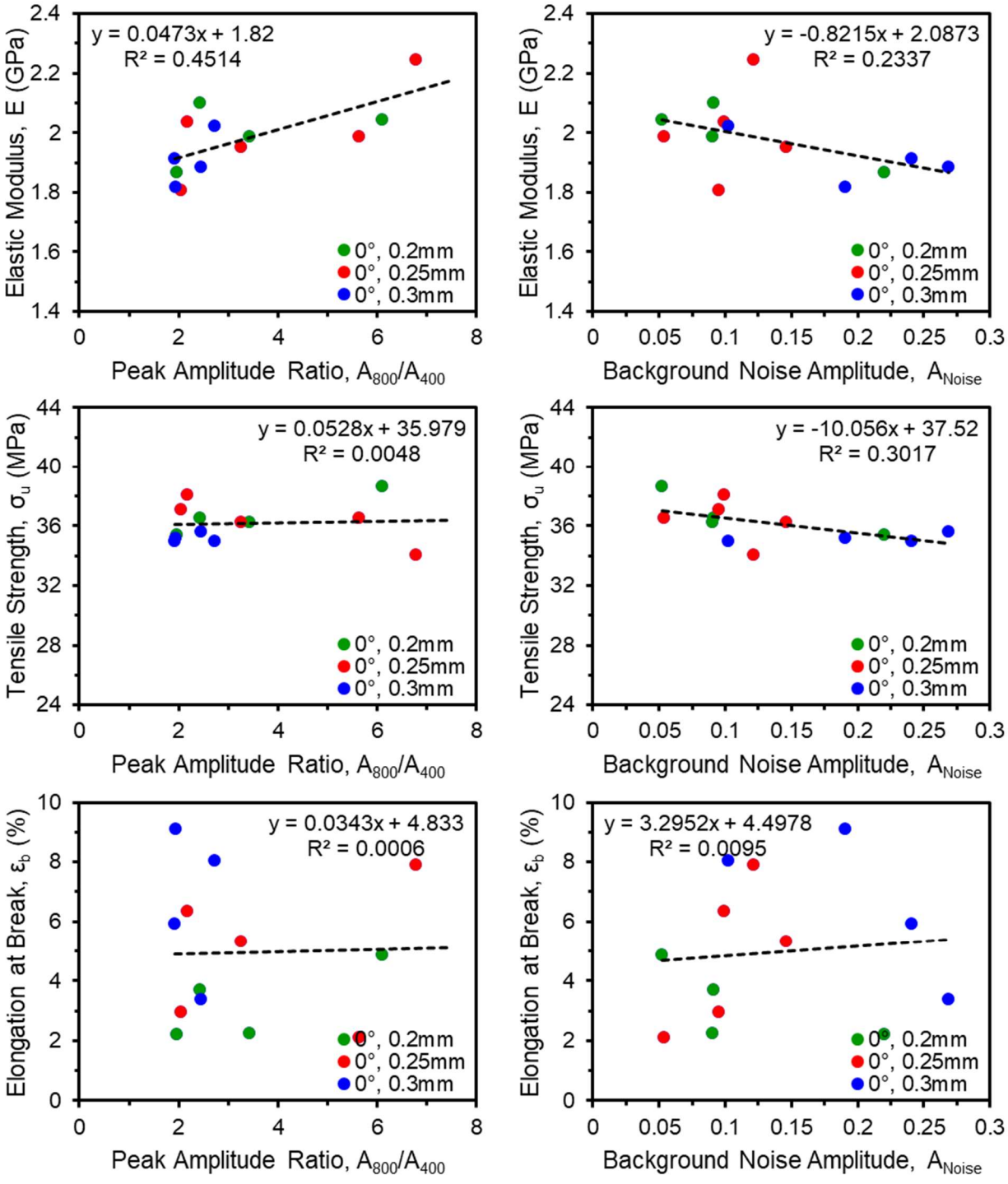
y = 0.0473x + 1.82
R² = 0.4514
Elastic Modulus, E (GPa)
Peak Amplitude Ratio, A800/A400
y = -0.8215x + 2.0873
R² = 0.2337
Background Noise Amplitude, ANoise
y = 0.0528x + 35.979
R² = 0.0048
Tensile Strength, σu (MPa)
y = -10.056x + 37.52
R² = 0.3017
y = 0.0343x + 4.833
R² = 0.0006
Elongation at Break, εb (%)
y = 3.2952x + 4.4978
R² = 0.0095
0°, 0.2mm
0°, 0.25mm
0°, 0.3mm

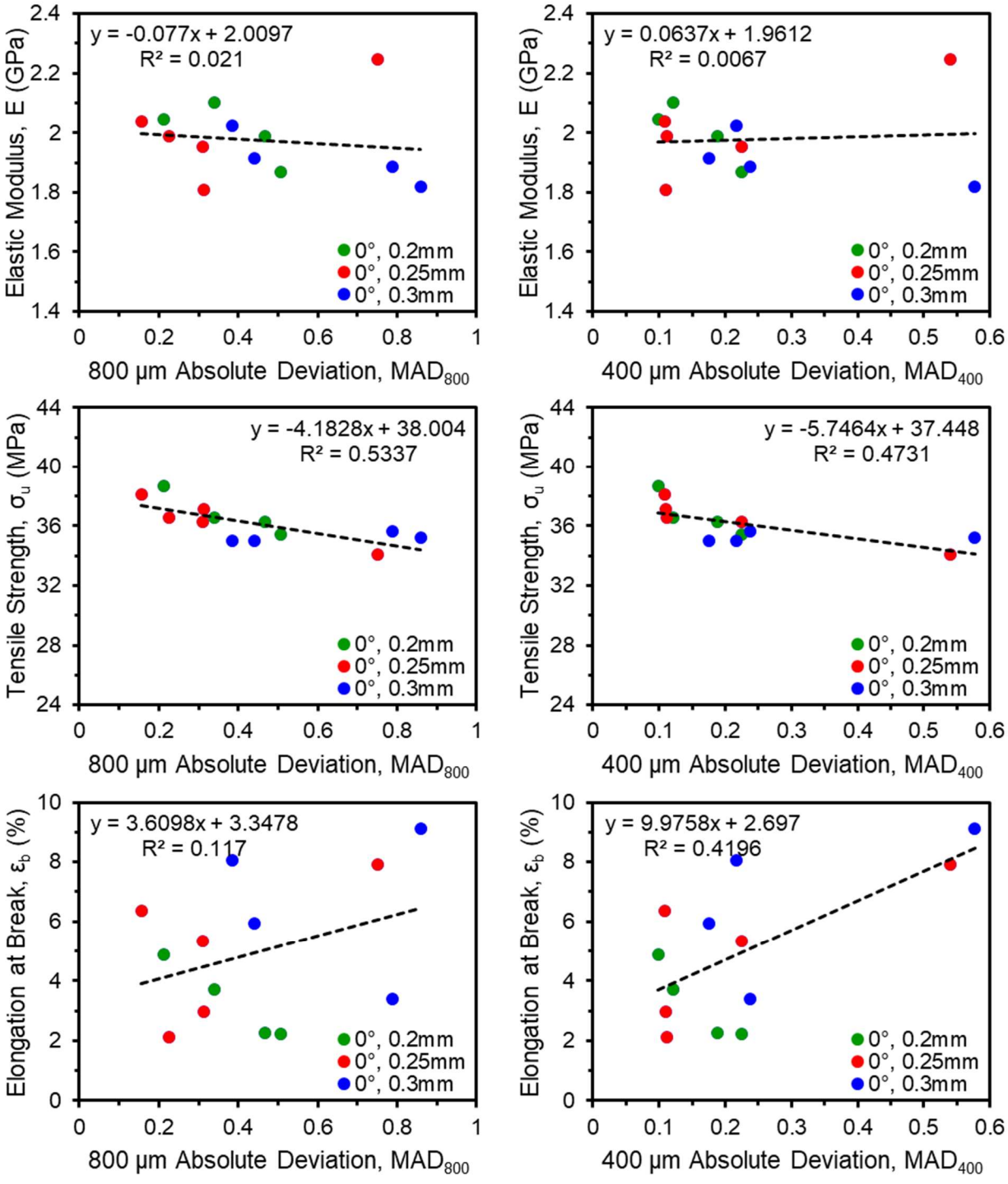
y = -0.077x + 2.0097
R² = 0.021
Elastic Modulus, E (GPa)
800 µm Absolute Deviation, MAD800
0°, 0.2mm
0°, 0.25mm
0°, 0.3mm
y = 0.0637x + 1.9612
R² = 0.0067
Elastic Modulus, E (GPa)
400 µm Absolute Deviation, MAD400
y = -4.1828x + 38.004
R² = 0.5337
Tensile Strength, σu (MPa)
800 µm Absolute Deviation, MAD800
y = -5.7464x + 37.448
R² = 0.4731
Tensile Strength, σu (MPa)
400 µm Absolute Deviation, MAD400
y = 3.6098x + 3.3478
R² = 0.117
Elongation at Break, εb (%)
800 µm Absolute Deviation, MAD800
y = 9.9758x + 2.697
R² = 0.4196
Elongation at Break, εb (%)
400 µm Absolute Deviation, MAD400

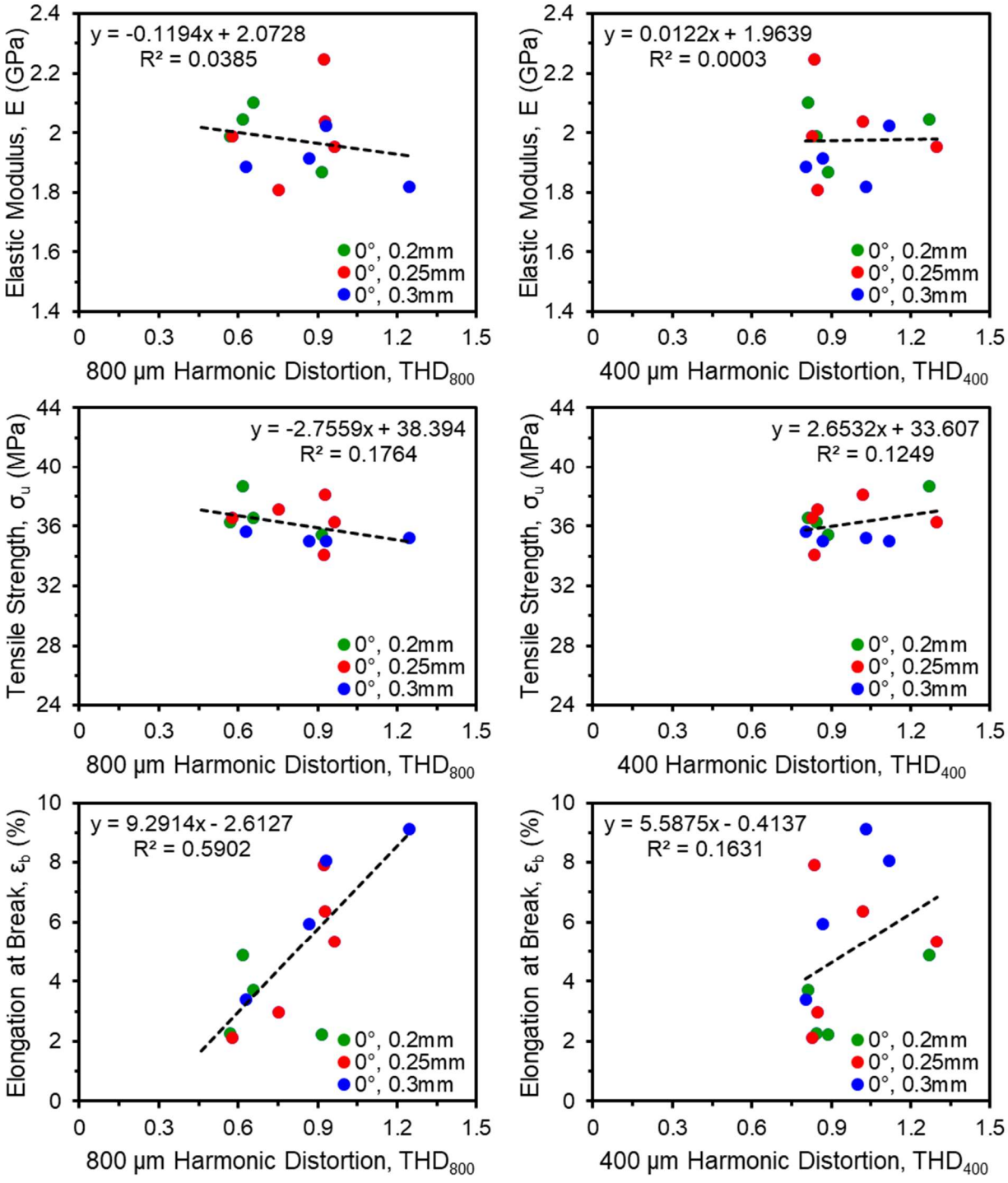

Figure A.3: Correlations of $A_{800+400}$, A_{800}/A_{400}, A_{Noise}, MAD_{800}, MAD_{400}, THD_{800}, and THD_{400}, with the elastic modulus, ultimate tensile strength, and elongation at break of all the tested 0° specimens.

BIBLIOGRAPHY

[1] T. Pereira et al., “A comparison of traditional manufacturing vs additive manufacturing, the best method for the job,” *Procedia Manuf.*, **30** 11-18 (2019). <https://doi.org/10.1016/j.promfg.2019.02.003>.

[2] S. A.M. Tofail et al., “Additive manufacturing: scientific and technological challenges, market uptake and opportunities,” *Mater. Today*, **21** [1] 22-37 (2018). <https://doi.org/10.1016/j.mattod.2017.07.001>.

[3] T. D. Ngo et al., “Additive manufacturing (3D printing): A review of materials, methods, applications and challenges,” *Compos. B. Eng.*, **143** 172-196 (2018). <https://doi.org/10.1016/j.compositesb.2018.02.012>.

[4] Z. Quan et al., “Additive manufacturing of multi-directional preforms for composites: opportunities and challenges,” *Mater. Today*, **18** [9] 503-512 (2015). <https://doi.org/10.1016/j.mattod.2015.05.001>.

[5] Y. Jiang et al., “Similarity quantification of 3D surface topography measurements,” *Measurement*, **186** 110207 (2021). < https://doi.org/10.1016/j.measurement.2021.110207>.

[6] T. J. Coogan and D. O. Kazmer, “Modeling of interlayer contact and contact pressure during fused filament fabrication,” *J. Rheol.*, **63** 655 (2019). <https://doi.org/10.1122/1.5093033>.

[7] F. Majid et al., “Mechanical behavior and crack propagation of ABS 3D printed specimens,” *Procedia Struct. Integr.*, **28** 1719-1726 (2020). <https://doi.org/10.1016/j.prostr.2020.10.147>.

[8] S. H. Ahn et al., “Anisotropic material properties of fused deposition modeling ABS,” *Rapid Prototyp. J.*, **8** [4] 248-257 (2002). <https://doi.org/10.1108/13552540210441166>.

[9] P. Shubham et al., “The Influence of Layer Thickness on Mechanical Properties of the 3D Printed ABS Polymer by Fused Deposition Modeling,” *Key Eng. Mater.*, **706** 63-67 (2016). <https://doi.org/10.4028/www.scientific.net/KEM.706.63>.

[10] N. D. Dolinski et al., “Solution Mask Liquid Lithography (SMaLL) for One-Step, Multimaterial 3D Printing,” *Adv. Mater.*, **30** [31] 1800364 (2018). <https://doi.org/10.1002/adma.201800364>.

[11] W. Gao et al., “The status, challenges, and future of additive manufacturing in engineering,” *Comput. Aided Des.*, **69** 65-89 (2015). <https://doi.org/10.1016/j.cad.2015.04.001>.

[12] ASTM Standard 52900, 2021, " Additive manufacturing — General principles — Fundamentals and vocabulary," ASTM International, West Conshohocken, PA, 2003. <https://www.astm.org/f3177-21.html>.

[13] C. Druga et al., “Analysis of the Influence of the Layer Height on the Strength of 3D Printed Structures,” *11th International Conference on Information Science and Information Literacy*, Brasov, Romania (2021). <https://doi.org/10.2478/9788395815065-019>.

[14] C. McIlroy and P. D. Oldmsted, “Disentanglement effects on welding behaviour of polymer melts during the fused-filament-fabrication method for additive manufacturing,” *Polymer*, **123** 376-391 (2017). <https://doi.org/10.1016/j.polymer.2017.06.051>.

[15] N. P. Levenhagen and M. D. Dadmun, “Reactive Processing in Extrusion-Based 3D Printing to Improve Isotropy and Mechanical Properties,” *Macromolecules*, **52** [17] 6495-6501 (2019). <https://doi.org/10.1021/acs.macromol.9b01178>.

[16] D. P. Street et al., “Self-Complementary Multiple Hydrogen-Bonding Additives Enhance Thermomechanical Properties of 3D-Printed PMMA Structures,” *Macromolecules*, **52** [15] 5574-5582 (2019). <https://doi.org/10.1021/acs.macromol.9b00546>.

[17] T. D’Amico and A. M. Peterson, “Bead parameterization of desktop and room-scale material extrusion additive manufacturing: How print speed and thermal properties affect heat transfer,” *Addit. Manuf.*, **34** 101239 (2020). <https://doi.org/10.1016/j.addma.2020.101239>.

[18] M. Faes et al., “Influence of Inter-layer Cooling time on the Quasi-static Properties of ABS Components Produced via Fused Deposition Modelling,” *Procedia CIRP*, **42** 748-753 (2016). <https://doi.org/10.1016/j.procir.2016.02.313>.

[19] J. R. Ai and B. D. Vogt, “Size and print path effects on mechanical properties of material extrusion 3D printed plastics,” *Prog. Addit. Manuf.*, **7** 1009-1021 (2022). <https://doi.org/10.1007/s40964-022-00275-w>.

[20] F. Peng et al., “Enhanced Impact Resistance of Three-Dimensional-Printed Parts with Structured Filaments,” *ACS Appl. Mater. Interfaces*, **10** [18] 16087-16094 (2018). <https://doi.org/10.1021/acsami.8b00866>.

[21] A. Das et al., “Importance of Polymer Rheology on Material Extrusion Additive Manufacturing: Correlating Process Physics to Print Properties,” *ACS Appl. Polym. Mater.*, **3** [3] 1218-1249 (2021). <https://doi.org/10.1021/acsapm.0c01228>.

[22] C. Y. Poon and B. Bhushan, “Comparison of surface roughness measurements by stylus profiler, AFM and non-contact optical profiler,” *Wear*, **190** [1] 76-88 (1995). <https://doi.org/10.1016/0043-1648(95)06697-7>.

[23] C. J. Tay et al., “In situ surface roughness measurement using a laser scattering method,” *Opt. Commun.*, **218** [1-3] 1-10 (2003). <https://doi.org/10.1016/S0030-4018(03)01102-7>.

[24] Y. Zheng et al., “Similarity evaluation of topography measurement results by different optical metrology technologies for additive manufactured parts,” *Opt. Lasers Eng.*, **126** 105920 (2020). <https://doi.org/10.1016/j.optlaseng.2019.105920>.

[25] Y. Zhou et al., “Application of the random ball test for calibrating slope-dependent errors in profilometry measurements,” *Appl. Opt.*, **52** [24] 5925-5931 (2013). <https://doi.org/10.1364/AO.52.005925>.

[26] J. Straub, “Initial Work on the Characterization of Additive Manufacturing (3D Printing) Using Software Image Analysis,” *Machines*, **3** [2] 55-71 (2015). <https://doi.org/10.3390/machines3020055>.

[27] M. Launhardt et al., “Detecting surface roughness on SLS parts with various measuring techniques,” *Polym. Test.*, **53** 217-226 (2016). <https://doi.org/10.1016/j.polymertesting.2016.05.022>.

[28] M. A. de Pastre et al., “Polymer powder bed fusion surface texture measurement,” *Meas. Sci. Technol.*, **31** 055002 (2020). <https://doi.org/10.1088/1361-6501/ab63b1>.

[29] S. Wang et al., “Similarity evaluation of 3D surface topography measurements,” *Meas. Sci. Technol.*, **32** 125003 (2021). <https://doi.org/10.1088/1361-6501/ac1b41>.

[30] E. G. Thwaite and M. J. Puttock, “Power Spectra of Rough Surfaces Obtained by Optical Fourier Transformation,” *CIRP Ann.*, **29** [1] 419-422 (1980). <https://doi.org/10.1016/S0007-8506(07)61363-8>.

[31] “Blue ABS Filament - 1.75mm, 1kg Spool,” *Hatchbox*, Web. <https://www.hatchbox3d.com/products/3d-abs-1kg1-75-blu>.

[32] ASTM Standard D638, 2022, "Standard Test Method for Tensile Properties of Plastics," ASTM International, West Conshohocken, PA, 2003. <https://www.astm.org/d0638-22.html>.

[33] “FFT (Fast Fourier Transform) Waveform Analysis,” *Dataq Instruments*, Web. <https://www.dataq.com/data-acquisition/general-education-tutorials/fft-fast-fourier-transform-waveform-analysis.html>.

[34] M. Gasior and J. L. Gonzalez, “Improving FFT Frequency Measurement Resolution by Parabolic and Gaussian Spectrum Interpolation,” *AIP Conf. Proc.*, **732** [1] 276 (2004). <https://doi.org/10.1063/1.1831158>.

[35] D. Williams, “Understanding, Calculating, and Measuring Total Harmonic Distortion (THD),” *All About Circuits*, Web. 20 Feb. 2017. <https://www.allaboutcircuits.com/technical-articles/the-importance-of-total-harmonic-distortion>.

[36] M. Faes et al., “Variability In Mechanical Properties Of ABS Parts Produced By Fused Deposition Modelling,” *2015 NAFEMS World Congress*, San Diego, CA (2015). <https://www.nafems.org/publications/resource_center/nwc15_428/>.

[37] A. Sola et al., “Open challenges in tensile testing of additively manufactured polymers: A literature survey and a case study in fused filament fabrication,” *Polym. Test.*, **117** 107859 (2023). <https://doi.org/10.1016/j.polymertesting.2022.107859>.

ACADEMIC VITA

Bevan Harbinson

EDUCATION

Bachelor of Science in Materials Science & Engineering — University Park, PA
Specialization in Polymer Science — Class of 2023
The Pennsylvania State University
Schreyer Honors College

INTERNSHIP EXPERIENCE

Testing, Analytics & Physics North America Intern — Pittsburgh, PA
Covestro LLC — May 2022 – August 2022

- Assessed systematic error produced during accelerated weathering experiments.
- Measured degree of material weathering according to CIELAB color difference, specular gloss retention, and Fourier-transform infrared spectroscopy (FTIR).
- Identified service life prediction models to improve knowledge of degradation mechanisms.
- Performed monthly lab safety inspections with Materials Testing staff.

Materials Characterization Lab Research Assistant — University Park, PA
The Pennsylvania State University — May 2021 – May 2022

- Independently operated scanning (SEM) and transmission (TEM) electron microscopes.
- Developed macros for the algorithmic analysis of SEM images with ImageJ.
- Collected TEM images and energy-dispersive X-ray spectroscopy (EDS) maps.
- Analyzed ceramic and polymeric materials using powder X-ray diffraction (XRD).

Design & Drafting Work-Based Learning Intern — Richland, WA
Energy Northwest — August 2018 – August 2019

- Revised structural, mechanical, and electrical drawings using AutoCAD.
- Organized and analyzed large data sets related to plant systems and design.
- Collaborated with nuclear, civil, mechanical, electrical, and design engineers.

TECHNICAL SKILLS

- Trained in material characterization methods including SEM, TEM, EDS, XRD, and FTIR.
- Experienced in design using AutoCAD, SolidWorks, and Adobe Suite.
- Certified in Microsoft Word, PowerPoint, and Excel.
- Proficient in MATLAB, HTML, and JavaScript.

LEADERSHIP & INVOLVEMENT

Senior Class Representative, Material Advantage — September 2019 – Present
Member, 3D Printing Club — September 2019 – Present

ACHIEVEMENTS & AWARDS

- 1st Place MATSE 492W Sustainability Team Project 2022
- The Evan Pugh Scholar Award 2022
- The President Sparks Award 2021
- The President's Freshman Award 2020
- Delta High School Valedictorian 2019